NATIONAL AND KAPODISTRIAN UNIVERSITY OF ATHENS

SCHOOL OF SCIENCES
DEPARTMENT OF INFORMATICS AND TELECOMMUNICATIONS

PROGRAM OF POSTGRADUATE STUDIES

PhD THESIS

Image Analysis and Processing

With Applications in Proteomics and Medicine

Eleftheria A. Mylona

ATHENS

JANUARY 2014

ΕΘΝΙΚΟ ΚΑΙ ΚΑΠΟΔΙΣΤΡΙΑΚΟ ΠΑΝΕΠΙΣΤΗΜΙΟ ΑΘΗΝΩΝ

ΣΧΟΛΗ ΘΕΤΙΚΩΝ ΕΠΙΣΤΗΜΩΝ
ΤΜΗΜΑ ΠΛΗΡΟΦΟΡΙΚΗΣ ΚΑΙ ΤΗΛΕΠΙΚΟΙΝΩΝΙΩΝ

ΠΡΟΓΡΑΜΜΑ ΜΕΤΑΠΤΥΧΙΑΚΩΝ ΣΠΟΥΔΩΝ

ΔΙΔΑΚΤΟΡΙΚΗ ΔΙΑΤΡΙΒΗ

Ανάλυση και Επεξεργασία Εικόνας

Με Εφαρμογές στην Πρωτεομική και Ιατρική

Ελευθερία Α. Μυλωνά

Ευρωπαϊκή Ένωση
Ευρωπαϊκό Κοινωνικό Ταμείο

ΕΠΙΧΕΙΡΗΣΙΑΚΟ ΠΡΟΓΡΑΜΜΑ
ΕΚΠΑΙΔΕΥΣΗ ΚΑΙ ΔΙΑ ΒΙΟΥ ΜΑΘΗΣΗ
επένδυση στην κοινωνία της γνώσης
ΥΠΟΥΡΓΕΙΟ ΠΑΙΔΕΙΑΣ & ΘΡΗΣΚΕΥΜΑΤΩΝ, ΠΟΛΙΤΙΣΜΟΥ & ΑΘΛΗΤΙΣΜΟΥ
ΕΙΔΙΚΗ ΥΠΗΡΕΣΙΑ ΔΙΑΧΕΙΡΙΣΗΣ

ΕΣΠΑ 2007-2013
πρόγραμμα για την ανάπτυξη
ΕΥΡΩΠΑΪΚΟ ΚΟΙΝΩΝΙΚΟ ΤΑΜΕΙΟ

Με τη συγχρηματοδότηση της Ελλάδας και της Ευρωπαϊκής Ένωσης

ΑΘΗΝΑ

ΙΑΝΟΥΑΡΙΟΣ 2014

PhD THESIS

Image Analysis and Processing with Applications in Proteomics and Medicine

Eleftheria A. Mylona

SUPERVISOR: Dimitris Maroulis, Professor UoA

THREE-MEMBER ADVISORY COMMITTEE:
Dimitris Maroulis, Professor UoA
Athanassios Skodras, Professor UPATRAS
Ioannis Ellinas, Professor TEI PIRAEUS

SEVEN-MEMBER EXAMINATION COMMITTEE

Dimitris Maroulis,
Professor UoA

Athanassios Skodras,
Professor UPATRAS

Ioannis Ellinas,
Professor TEI
PIRAEUS

Sergios Theodoridis,
Professor UoA

Theoharis Theoharis,
Professor UoA

Emmanouil Sagriotis,
Assistant Professor UoA

Sophia Kossida,
Investigator C' BRFAA

Examination Date 9/1/2014

ΔΙΔΑΚΤΟΡΙΚΗ ΔΙΑΤΡΙΒΗ

Ανάλυση και Επεξεργασία Εικόνας με Εφαρμογές στην Πρωτεομική και Ιατρική

Ελευθερία Α. Μυλωνά

ΕΠΙΒΛΕΠΩΝ ΚΑΘΗΓΗΤΗΣ: Δημήτρης Μαρούλης, Καθηγητής ΕΚΠΑ

ΤΡΙΜΕΛΗΣ ΕΠΙΤΡΟΠΗ ΠΑΡΑΚΟΛΟΥΘΗΣΗΣ:
Δημήτρης Μαρούλης, Καθηγητής ΕΚΠΑ
Αθανάσιος Σκόδρας, Καθηγητής Πανεπιστημίου Πατρών
Ιωάννης Έλληνας, Καθηγητής ΤΕΙ Πειραιά

ΕΠΤΑΜΕΛΗΣ ΕΞΕΤΑΣΤΙΚΗ ΕΠΙΤΡΟΠΗ

Δημήτρης Μαρούλης,
Καθηγητής ΕΚΠΑ

Αθανάσιος Σκόδρας,
Καθηγητής Πανεπιστημίου Πατρών

Ιωάννης Έλληνας,
Καθηγητής ΤΕΙ Πειραιά

Σέργιος Θεοδωρίδης,
Καθηγητής ΕΚΠΑ

Θεοχάρης Θεοχάρης,
Καθηγητής ΕΚΠΑ

Εμμανουήλ Σαγκριώτης,
Αναπληρωτής Καθηγητής ΕΚΠΑ

Σοφία Κοσσίδα,
Ερευνήτρια Γ' ΙΙΒΕΑΑ

Ημερομηνία εξέτασης 9/1/2014

ABSTRACT

This thesis introduces unsupervised image analysis algorithms for the segmentation of several types of images, with an emphasis on proteomics and medical images. The presented algorithms are tailored upon the principles of deformable models and more specific region-based active contours. Two different objectives are pursued. The first is the core issue of unsupervised parameterization in image segmentation, whereas the second is the formulation of a complete model for the segmentation of proteomics images, which is the first to exploit the appealing attributes of active contours.

The first major contribution of this thesis is a novel framework for the automated parameterization of region-based active contours. The presented framework aims to endow segmentation results with objectivity and robustness as well as to set domain users free from the cumbersome and time-consuming process of empirical adjustment. It is applicable on various medical imaging modalities and remains insensitive on alterations in the settings of the acquisition devices. The experimental results demonstrate that the presented framework maintains a segmentation quality which is comparable to the one obtained with empirical parameterization.

The second major contribution of this thesis is an unsupervised active contour-based model for the segmentation of proteomics images. The presented model copes with crucial issues in *2D-GE* image analysis including streaks, artifacts, faint and overlapping spots. In addition, it provides an alternate to the laborious, error-prone process of manual editing, which is required in state-of-the-art *2D-GE* image analysis software packages. The experimental results demonstrate that the presented model outperforms *2D-GE* image analysis software packages in terms of detection and segmentation quantity metrics.

SUBJECT AREA: Image Analysis

KEYWORDS: Segmentation, Active Contours, Proteomics Images, Medical Images

ΠΕΡΙΛΗΨΗ

Στην παρούσα διατριβή παρουσιάζονται αυτόματοι αλγόριθμοι ανάλυσης εικόνας για την κατάτμηση διαφόρων τύπων εικόνων, με έμφαση στις εικόνες πρωτεομικής και στις ιατρικές εικόνες. Οι προτεινόμενοι αλγόριθμοι βασίζονται στις αρχές των παραμορφώσιμων μοντέλων και ειδικότερα των ενεργών περιγραμμάτων περιοχής. Η διατριβή εστιάζει σε δύο κυρίως στόχους: ο πρώτος είναι η επίλυση του σημαντικού προβλήματος της αυτόματης παραμετροποίησης στην κατάτμηση εικόνας, ενώ ο δεύτερος είναι η διατύπωση ενός ολοκληρωμένου μοντέλου κατάτμησης εικόνων πρωτεομικής που αξιοποιεί το ανάπτυγμα των ενεργών περιγραμμάτων.

Η πρώτη κύρια συνεισφορά της παρούσας διατριβής είναι ένα πρωτότυπο πλαίσιο για την αυτόματη παραμετροποίηση των ενεργών περιγραμμάτων περιοχής. Το πλαίσιο που παρουσιάζεται έχει σκοπό να εμπλουτίσει τα αποτελέσματα με αντικειμενικότητα και αρτιότητα καθώς και να απελευθερώσει τους τελικούς χρήστες από την επίπονη και χρονοβόρα διαδικασία της εμπειρικής ρύθμισης. Μπορεί να εφαρμοσθεί σε διάφορους τύπους ιατρικών εικόνων και παραμένει ανεπηρέαστο στις τροποποιήσεις των ρυθμίσεων των συσκευών λήψης των εικόνων αυτών. Τα πειραματικά αποτελέσματα καταδεικνύουν ότι το προτεινόμενο πλαίσιο διατηρεί υψηλή την ποιότητα κατάτμησης, συγκρίσιμη με εκείνη που επιτυγχάνεται με εμπειρική παραμετροποίηση.

Η δεύτερη κύρια συνεισφορά της διατριβής είναι ένα αυτόματο μοντέλο βασιζόμενο στα ενεργά περιγράμματα για την κατάτμηση εικόνων πρωτεομικής. Το μοντέλο αυτό αντιμετωπίζει σημαντικά προβλήματα στην ανάλυση δι-διάστατων εικόνων ηλεκτροφόρησης συμπεριλαμβανομένων των γραμμών, τεχνουργημάτων, αχνών και επικαλυπτομένων κηλίδων. Ακόμη, παρέχει εναλλακτική λύση στην επίπονη, επιρρεπή σε σφάλματα διαδικασία της χειρωνακτικής επεξεργασίας, η οποία απαιτείται στα υπάρχοντα πακέτα λογισμικού ανάλυσης δι-διάστατων εικόνων ηλεκτροφόρησης. Τα πειραματικά αποτελέσματα καταδεικνύουν ότι το προτεινόμενο μοντέλο υπερτερεί των υπαρχόντων πακέτων λογισμικού δι-διάστατης ανάλυσης σε ποσοτικές μετρικές εντοπισμού και κατάτμησης.

ΘΕΜΑΤΙΚΗ ΠΕΡΙΟΧΗ: Ανάλυση Εικόνας

ΛΕΞΕΙΣ ΚΛΕΙΔΙΑ: Κατάτμηση, Ενεργά Περιγράμματα, Εικόνες Πρωτεομικής, Ιατρικές Εικόνες

“The task is…not so much to see what no one has yet seen; but to think what nobody has yet thought, about that which everybody sees.”

Erwin Schrödinger (8/1887-1/1961)

To my parents, Mary and Antonis...

ACKNOWLEDGEMENTS

I would like to express my sincere gratitude to my supervisor Professor Dimitris Maroulis for accepting me as a member of his group and giving me the opportunity to work in an inspiring and challenging field of research. Prof. Maroulis, thank you for your continuous supervision, support, guidance and encouragement. You were always eager to share your knowledge by teaching me how to deal with scientific problems from the beginning till the very end of this thesis.

I am most grateful to Dr. Michalis Savelonas for the untiring and relentless proofreading of all manuscripts and for the constructive criticism. Michali, thank you for always being available to answer questions and give valuable advice regardless of your busy schedule. I enjoyed all our stimulating conversations and felt confident to tackle scientific problems. I have been very fortunate to have you.

I would also like to thank the members of my PhD Advisory and Examination Committee for reviewing this thesis and providing insightful comments on improving the manuscript.

I would like to thank the people of the Biomedical Research Foundation of the Academy of Athens, Dr. Sophia Kossida, Dr. Antonia Vlahou and Dr. Manousos Makridakis for the provision of proteomics images and their ground truth as well as their valuable help and expertise in the field of proteomics.

I would also like to thank Dr. Michalis Aivaliotis from the Foundation of Research and Technology, Institute of Molecular Biology and Biotechnology, for the provision of segmentation results obtained by Delta2D image analysis software package as well as for his availability to answer all kinds of questions concerning this software.

Many thanks go to my colleagues at The Real-Time Systems & Image Analysis Lab for their friendship, collaboration, valuable advice, constructive discussions and the pleasant working environment they created during all these years. Dimitri, Strato, Dionysi, Eleni, Eirini, Stamo, you were great colleagues. I really enjoyed sharing the office space with you. Eirini, Stamo, good luck with the rest of your Ph.D.

I would like to thank my Master's supervisor Professor Murray Campbell in the School of Physics and Astronomy, University of Edinburgh for encouraging me with the continuation of my research studies. Prof. Murray, thank you for always treating me as a colleague and inspiring me through your passion for research.

I would also like to thank my Bachelor's supervisor Professor Dimitris Tsoukalas in the School of Applied Mathematics and Physical Sciences, National Technical University of Athens and co-supervisor Lecturer Panagiotis Photopoulos in the Technological Educational Institute of Athens for contributing to my earlier education, introducing me to the joys of research and inspiring me through our fruitful conversations. Pano, thank you for always mentoring me to become not only an independent researcher yet an independent, critical mind.

I wish to thank my parents for their unconditional and endless love and support during these years and at any stage of my life. Mum, Dad, thank you for your constant optimism and kindness. All of this would not have been possible if it weren't for you. You are my rocks.

I wish to thank my sister Dr. Athina Mylona and my brother in-law Senior Lecturer Kristofer Leslie for their scientific advice, support and love. Athina, Kris, thank you for always being there when I needed you.

I would like to thank my aunts Kiki and Efi for their love and support at any stage of my life.

I would also like to thank my second family Professor Ioannis Chandrinos, Mrs. Elpida Chandrinou, Dr. Chryssa Chandrinou and Lecturer Emmanouil Topoglidis for their support and their valuable advice during the years of my thesis.

Many thanks go to my friends Kleopatra, Marcia, Olga, Stefano, Rhea, John, George, Dimitra, Elias, Sophia, Zinwna, Vassiliki, Paul, Rebecca for their encouragement, understanding and patience during all these years.

Finally, I would like to thank Demosthenes Chandrinos for his emotional support, love, endless patience, understanding and encouragement during all these years. Demo, what can I say, thank you for everything…

LIST OF PUBLICATIONS (17)

International Journals

1. E.A. Mylona, M.A. Savelonas, D. Maroulis, “Automated Adjustment of Region-Based Active Contour Parameters Using Local Image Geometry,” accepted with revisions to ***IEEE Transactions on Cybernetics*** (26/11/2013).
2. E.A. Mylona, M.A. Savelonas, D. Maroulis, “Self-Parameterized Active Contours Based on Regional Edge Structure for Medical Image Segmentation,” submitted to ***Medical & Biological Engineering & Computing*** (26/8/2013).
3. M.A. Savelonas, E.A. Mylona, D. Maroulis, "Unsupervised 2D Gel Electrophoresis Image Segmentation based on Active Contours," ***Pattern Recognition***, vol. 45, pp. 720-731, 2012.
4. E.A. Mylona, M.A. Savelonas, D. Maroulis, S. Kossida, "A Computer-Based Technique for Automated Spot Detection in Proteomics Images," ***IEEE Transactions on Information Technology in Biomedicine***, vol. 15, no. 4, pp. 661-667, 2011.

Book Chapters

1. E.A. Mylona, M.A. Savelonas, D. Maroulis, "Towards Self-Parameterized Active Contours for Medical Image Segmentation with Emphasis on Abdomen," A.S. El-Baz et al. (eds.), Abdomen and Thoracic Imaging: An Engineering & Clinical Perspective, ***Springer Science + Business Media,*** New York, 2014.

International Conferences

1. E.A. Mylona, M.A. Savelonas, D. Maroulis, “Automated Parameterization of Active Contours: A Brief Survey,” in Proc. *IEEE International Symposium on Signal Processing and Information Technology (**ISSPIT**)*, Athens, Greece, 2013.
2. E.A. Mylona, M.A. Savelonas, D. Maroulis, “Self-Adjusted Active Contours Using Multi-Directional Texture Cues,” in Proc. *IEEE International Conference on Image Processing* (***ICIP***), Melbourne, Australia, 2013.
3. E.A. Mylona, M.A. Savelonas, E. Zacharia, D. Maroulis, C. Pattichis, “Unsupervised Level Set Parameterization Using Multi-Scale Filtering,” in Proc. *IEEE International Conference on Digital Signal Processing* (***DSP***), Santorini, Greece, 2013.

4. E.A. Mylona, M.A. Savelonas, D. Maroulis, A.N. Skodras, “Autopilot Spatially-Adaptive Active Contour Parameterization for Medical Image Segmentation,” in Proc. *IEEE International Symposium on Computer-Based Medical Systems* (***CBMS***), Porto, Portugal, 2013.
5. E.A. Mylona, M.A. Savelonas, D. Maroulis, "Entropy-Based Spatially-Varying Adjustment of Active Contour Parameters," in Proc. *IEEE International Conference on Image Processing* (***ICIP***), Orlando, FL, USA, 2012.
6. M. Savelonas, E. Mylona, D. Maroulis, "An Automatically Initialized Level-Set Approach for the Segmentation of Proteomics Images," in Proc. *IEEE International Workshop on Biomedical Engineering*, Kos, Greece, 2011.
7. E.A. Mylona, M.A. Savelonas, D. Maroulis, M. Aivaliotis, "2D-GE Image Segmentation based on Level-Sets," in Proc. *IEEE International Conference on Image Processing (**ICIP**)*, Brussels, Belgium, 2011.
8. E. Mylona, M. Savelonas, D. Maroulis, "A Two-Stage Active Contour-based Scheme for Spot Detection in Proteomics Images," in Proc. *IEEE International Conference on Information Technology Applications in Biomedicine (**ITAB**)*, Corfu, Greece, 2010.
9. E. Mylona, M. Savelonas, D. Maroulis, "Protein Spot Detection in 2D-GE Images using Morphological Operators," in Proc. *IEEE International Symposium on Computer-Based Medical Systems (**CBMS**)*, Perth, Australia, 2010.
10. M. Savelonas, E. Mylona, D. Maroulis, "A Level Set Approach for Proteomics Image Analysis," in Proc. *European Signal Processing Conference (**EUSIPCO**)*, Aalborg, Denmark, 2010.
11. M.A. Savelonas, D. Maroulis, E. Mylona, "Segmentation of Two-Dimensional Gel Electrophoresis Images containing Overlapping Spots,” in Proc. *IEEE International Conference on Information Technology Applications in Biomedicine (**ITAB**)*, Larnaca, Cyprus, 2009.

Hellenic Conferences

1. E. Mylona, M. Savelonas, D. Maroulis, "Computer-based Methodology for Protein Spot Detection and its Contribution to Health Services", *14th Panhellenic Conference of the Greek Physicists Union*, Kamena Vourla, Greece, 2012.

CONTENTS

LIST OF TABLES

LIST OF FIGURES

PREFACE

In this thesis, unsupervised image analysis algorithms are developed for image segmentation, especially implemented on proteomics and medical images. A novel framework for automated region-based active contour parameterization is developed, aiming to endow segmentation results with objectivity and robustness as well as to set domain users free from the cumbersome and time-consuming process of empirical parameter adjustment. In addition, an unsupervised active contour-based model for the segmentation of proteomics images is developed to provide an alternate to the laborious, error-prone process of manual editing by gel analysts.

This thesis is entitled: “Image Analysis and Processing with Applications in Proteomics and Medicine” (code: 70/3/11039), supervised by Professor UoA Dimitris Maroulis. This research has been co-financed by the European Union (European Social Fund-ESF) and Greek national funds through the Operational Program “Education and Lifelong Learning” of the National Strategic Reference Framework (NSFR)-Research Funding Program: Heracleitus II. Investing in knowledge society through the European Social Fund.

Eleftheria A. Mylona

Athens, January 2014.

CHAPTER 1

1. INTRODUCTION

1.1 The Segmentation Task

Segmentation is the process of partitioning an image into semantically disjoint regions (segments) so that each region exhibits homogeneous properties. The primary objective is to mine information on target regions associated with their shape, size and location on the image.

Definition: Let F be the set of all regions of an image and $P()$ be a uniformity (homogeneity) predicate defined on groups of connected pixels, then segmentation is a partitioning of the set F into a set of connected subsets or regions $(S_1,S_2,..,S_n)$ such that $\bigcup_{i=1}^{n} S_i = F$ with $S_i \cap S_j = \varnothing$ when $i \neq j$. The uniformity predicate $P(S_i)$ is true for all regions S_i and $P(S_i \bigcup S_j)$ is false when S_i is adjacent to S_j.

Segmentation is a challenging task in computer vision with essential applications in biomedical engineering, remote sensing, robotics and automation. Typically, the target region is separated from the rest of image regions utilizing defining features including intensity, texture, color or motion cues. In this light, multiple segments are generated and the selection of the most significant segments becomes a controversial decision as it highly hinges on heuristic considerations. Figure 1.1 depicts: (a) a sample image obtained by the Berkeley segmentation dataset [1] as well as (b)-(d) different versions of ground truth images. A significant task in order to develop image segmentation algorithms is the provision of objective, informative and usable ground truth images. This task becomes even more difficult in cases that experts disagree with one another and the validity of the ground truth is disputed.

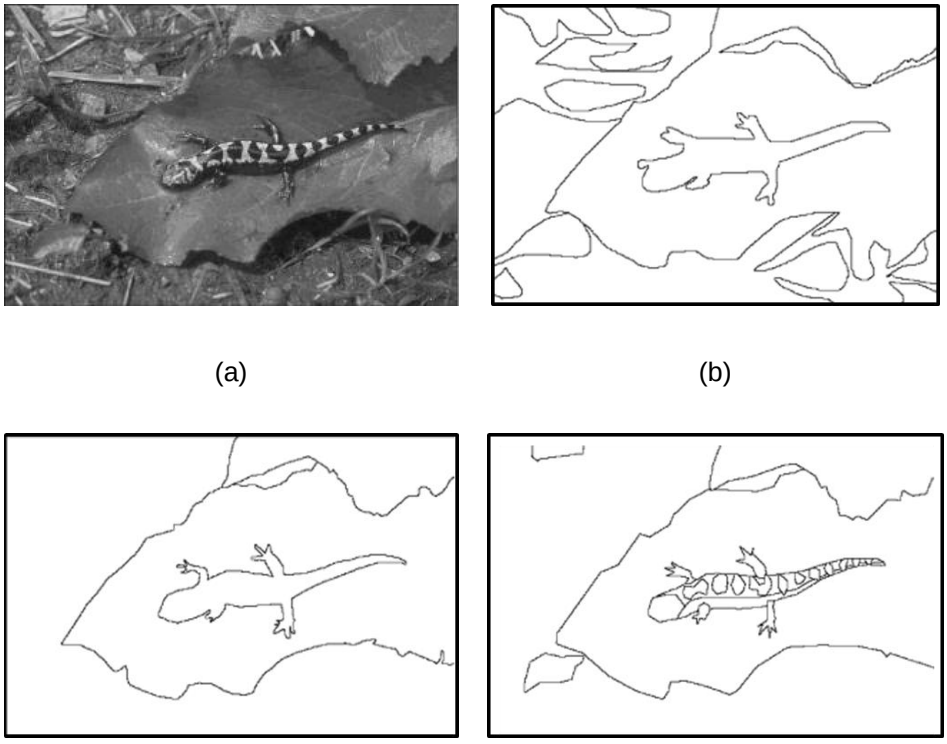

(a) (b)

(c) (d)

Figure 1.1: (a) Sample image obtained by the Berkeley segmentation dataset [1], (b)-(d) different versions of ground truth images.

Moreover, the separation of the target regions is impeded by several daunting factors such as: background clutter, the presence of noise and artifacts as well as occlusions on multiple target regions. This thesis focuses on image segmentation using deformable models and specifically region-based Active Contours (*ACs*) [2] because of their strong mathematical foundation and their appealing properties (*see Chapter 2, § 2.5.4*). Figure 1.2 depicts an example of the style of image segmentation adopted in this thesis, utilizing texture information. The segmentation task is performed by delineating the boundaries of target regions via contour tracking.

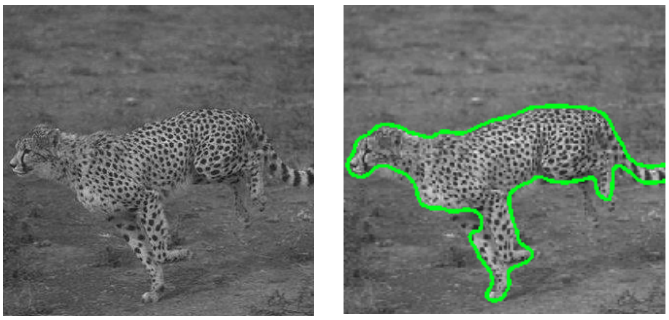

Figure 1.2: Example of the style of image segmentation adopted in this thesis.

1.2 Objectives of the Thesis

This thesis aims to present unsupervised image analysis algorithms for the segmentation of various types of images, with a focus on proteomics and medical images.

- The first major objective of this thesis is to develop a novel framework which immunizes deformable models against empirical parameterization. The novel framework focuses on region-based *ACs* due to their appealing merits on biomedical image segmentation (*see Chapter 3)*. It is applied on various medical imaging modalities in order to set Medical Doctors (*MDs*) free from the tedious and time-consuming process of parameter tuning, as well as to bolster the objectivity and reliability of the segmentation results (*see Chapter 5*).
- The second major objective of this thesis is to develop unsupervised algorithms for spot detection and segmentation on proteomics images since state-of-the-art software packages and techniques generate results which require manual editing and corrections by gel expert analysts (*see Chapter 6*).

1.3 Contributions of the Thesis

The contributions of this thesis to the state-of-the-art are categorized into theoretical and applied and are addressed below:

Theoretical

- *A Novel Framework for Automated Parameterization of Region-Based ACs.*

  The presented framework aims to enrich segmentation results with objectivity and robustness as well as to set domain users free from the cumbersome and time-consuming process of empirical adjustment. Additionally, technical skills and *a priori* knowledge or learning considering the shape/size of the target region, are no longer a prerequisite for the end-user. The presented framework is inspired by an observed isomorphism between the eigenvalues of structure tensors and *AC* parameters. Both may act as descriptors of the orientation coherence in regions containing edges. The experimental results demonstrate that the presented framework maintains a high segmentation quality without the need of trial-and-error parameter adjustment. Moreover, due to its simplicity and flexibility, it can be embedded in various region-based *AC* variations. Refer to Chapter 3 for details of the novel framework.

Applied

- *Medical Image Segmentation Utilizing the Automatic Framework*.

  The presented framework is applicable to various medical imaging modalities regardless of the shape/size and the non-rigid boundaries of the internal anatomical structures as well as the degree of corruption due to the presence of noise. Furthermore, it is not sensitive on alterations in the settings of the acquisition devices and it relieves *MDs* from the laborious task or parameter tuning. Refer to Chapter 5 for details of medical image segmentation provided by the automatic framework.

- *Unsupervised AC-Based Model for the Detection and Segmentation of Proteomics Images*.

  The presented model is the first to exploit the attractive properties of the *AC* formulation, in order to confront acute issues in *2D-GE* image analysis, such as the presence of noise, streaks, multiplets and faint spots. Moreover, it relieves gel expert analysts from the tedious, error-prone process of manually correcting segmentation results obtained by state-of-the-art *2D-GE* image

analysis software packages. It is based on the formation of a spot-targeted level-set surface, as well as of morphologically-derived *AC* energy terms, used to guide *AC* initialization and evolution, respectively. The experimental results demonstrate that the presented model generates more plausible spot boundaries and outperforms *2D-GE* image analysis software packages in terms of detection and segmentation quantity measures. Refer to Chapter 6 for details of the unsupervised *2D-GE* image detection and segmentation based on *ACs*.

All ideas presented in this thesis have been published or are submitted in four (4) international peer-reviewed journals, eleven (11) international peer-reviewed conferences, one (1) book chapter and one (1) Hellenic conference. Among them, one work has been published in Pattern Recognition, Elsevier while another one has been published in IEEE Transactions on Information Technology in Biomedicine (*TITB*). One more has been accepted with revisions in IEEE Transactions on Cybernetics and another one has been submitted in Medical & Biological Engineering & Computing, Springer. Moreover, three papers have been published in the Proceedings of IEEE International Conference on Image Processing (*ICIP*), two in the Proceedings of IEEE Computer-Based Medical Systems (*CBMS*), two in the Proceedings of IEEE Information Technology and Applications in Biomedicine (*ITAB*), one in the Proceedings of IEEE Digital Signal Processing (*DSP*), one in the Proceedings of European Signal Processing Conference (*EUSIPCO*) and one in Proceedings of the IEEE International Workshop on Biomedical Engineering. Furthermore, one paper has been published in the Proceedings of IEEE International Symposium on Signal Processing and Information Technology (*ISSPIT*).

1.4 Organization of the Thesis

The remainder of this thesis is organized as follows:

Chapter 2 provides a literature review on the most representative segmentation methods. These include: a) thresholding, b) edge-based, c) region-based methods and d) deformable models. Particular emphasis is provided on the latter,

since most of the ideas presented in this thesis are based on deformable models and more specific region–based *ACs*.

Chapter 3 presents a novel framework for automated parameterization of region-based *ACs*. This chapter provides information on related work as well as the motivation that inspired the design of the framework. Furthermore, a detailed description of the methodology reveals the framework's inner mechanisms. The framework is incorporated into two region-based and one hybrid *AC* variation so as to demonstrate its versatility with respect to different region-based *AC* variations.

Chapter 4 provides an introduction on proteomics and medical images, on which all algorithms developed in this thesis, are applied. A brief biological and medical background is provided on either case along with the challenges of these images, which impede the segmentation task.

Chapter 5 presents medical image segmentation results on six medical image databases using the automatic framework. The utilized databases include: a) mammograms containing abnormalities, b) ultrasounds of thyroid nodules, c) endoscopy images containing polyps, d) dermoscopy images containing skin lesions, e) axial and coronal *CT* scans of lung parenchyma and f) labial teeth and gingiva photographic images.

Chapter 6 introduces an unsupervised *AC*-based model for the detection and segmentation of proteomics images. As a first step, protein detection is performed utilizing operators based on mathematical morphology. The presented detection technique is evaluated on real *2D-GE* images by comparing it with a popular software package. As a second step, protein spot segmentation is achieved by an *AC*-based scheme which is automatically initialized and is capable of separating overlapping spots as well as identifying faint spots. The presented segmentation scheme is experimentally evaluated on real and synthetic *2D-GE* images by comparing it with three state-of-the-art software packages.

Chapter 7 summarizes the major achievements of this thesis and provides ideas regarding possible future directions of this work.

CHAPTER 2

2. LITERATURE REVIEW ON SEGMENTATION METHODS

2.1 Introduction

This chapter provides a concise review of the most established segmentation methods published in literature so far as well as extensive references for further reading. The segmentation methods can be classified into four main categories: a) thresholding methods, b) edge-based methods, c) region-based methods and d) deformable models. Most of the ideas presented in this thesis are tailored upon the principles of deformable models.

2.2 Thresholding Methods

Thresholding is a simple yet effective method of image segmentation. It is implemented based on the intuitive idea of differentiating Pixels Of Interest (*POIs*) from the rest. Regions Of Interest (*ROIs*) are separated according to each specific application by comparing pixel intensity values with respect to a threshold value. The output is a binary image consisting of two states namely, foreground and background, each one assigned specific intensity values that fulfill the needs of implementation. *ROIs* are usually portrayed in the foreground.

Several thresholding applications focus on document image analysis with the aim to extract characters, logos, graphical content, lines or legends [4], scene processing [5], quality inspection of materials [6], cell image analysis [7] and segmentation of various imaging modalities [8]-[11]. Thresholding methods can be categorized into six types depending on the exploitation of: a) histogram shape-based, b) clustering-based, c) entropy-based, d) spatial-based and e) local statistics-based information [12].

2.2.1 Histogram Shape-Based

This category achieves thresholding based on the exploitation of the shape properties of the image histogram. Rosenfeld's method [13] analyzes the

concavities of the histogram $h(g)$ contrary to its convex hull $Hull(g)$, i.e. the set theoretic difference $|Hull(g) - h(g)|$. Intensity values associated with the deepest concavity points become threshold candidates. In the case that there are multiple competing concavities, various target attributes other than intensity may as well be exploited. Variations on this thresholding algorithm were proposed by [14]-[17]. Sezan's method [18] analyzes the peaks of the histogram by convolving the histogram function with a smoothing kernel. The aperture of the kernel is adjusted and the peaks of the histogram are merged. As a result, the histogram is reduced to a two-lobe function where each lobe consists of incipient e_i, maximum m_i and terminating s_i zero-crossings. The optimal threshold is located between the first terminating and second initiating zero-crossing and is calculated by the following formula:

$$T_{opt} = \gamma \cdot e_1 + (1-\gamma) \cdot s_2, \quad 0 \le \gamma \le 1 \tag{2.2.1}$$

2.2.2 Clustering-Based

In this category, the grey level data are divided into two clusters. Riddler et al. [19] proposed one of the first iterative approaches according to two-class Gaussian mixture models. At the n^{th} iteration, a new threshold value is established based on the average of the foreground and background class means. The iterations terminate when $|T_n - T_{n+1}|$ becomes sufficiently small. Leung and Fam [20] as well as Trussel [21] proposed thresholding approaches in a similar fashion. Yanni and Horne [22] initialized the mean value g_{mid} between two peaks of the histogram as $g_{mid} = (g_{\max} + g_{\min})/2$, where $g_{\max}$ is the highest non-zero grey level and $g_{\min}$ is the lowest so that $(g_{\max} - g_{\min})$ becomes the span of non-zero grey values in the histogram. The mean value is updated using the mean of the two peaks on the right and left as $g^*_{mid} = (g_{peak1} + g_{peak2})/2$.

Otsu [23] addressed the minimization of the weighted sum of within-class variances of the foreground and background pixels to establish an optimal

threshold. The results are satisfactory when the numbers of pixels in each class are close to each other.

2.2.3 Entropy-Based

The algorithms of this class exploit the entropy measure of the intensity distribution. Kapur et al. [24] considered the image foreground and background as two different signal sources and the obtained threshold value was the intensity value that maximizes the sum of the two class entropies. Moreover, Yen et al. [25] obtained the threshold that maximizes the entropy correlation. Sahoo et al. [26] incorporated the Renyi entropies H_f and H_b of the foreground and background, respectively defined as follows:

$$H_f = \frac{1}{1-\rho}\cdot\ln\left\{\sum_{g=0}^{T}\left[\frac{p(g)}{p(T)}\right]^{\rho}\right\},\quad H_b = \frac{1}{1-\rho}\cdot\ln\left\{\sum_{g=T+1}^{G}\left[\frac{p(g)}{1-p(T)}\right]^{\rho}\right\} \tag{2.2.2}$$

where $\rho \neq 1$ is a positive real parameter, T the threshold value and g the intensity values. By maximizing the sum of the foreground and the background Renyi entropies for the three ranges $0<\rho<1$, $\rho>1$ and $\rho \to 1$ in the limiting case, they obtain three different threshold values T_1, T_2 and T_3, respectively. The optimal threshold value is a weighted combination of these three threshold values.

2.2.4 Spatial-Based

Algorithms of this category utilize both intensity distribution and dependency of pixels on a neighborhood in the form of context probabilities, correlation functions, co-occurrence probabilities and local linear dependence models of pixels. Pal et al. [27] introduced an approach based on the observation that two images with identical histograms can have different entropies due to their spatial structure. Thus, they utilized the co-occurrence probability of intensities of each pixel over its horizontal and vertical neighbors. Chang et al. [28] proposed an approach

based on the minimization of the divergence between the co-occurrence probabilities of the original and binary image. The utilized measure of divergence was the Kullback-Leibler distance.

2.2.5 Local Statistics-Based

In this category, a threshold is calculated at each pixel based on local statistics such as intensity range or variance of the pixel neighborhood. According to Niblack [29] as well as Trier and Jain [30], a threshold is calculated by using local variance while the local contrast is exploited by White and Rohrer [31]. The latter compared the intensity value of a pixel with the average of the intensity values in a neighborhood chosen to be of character size. Provided that the pixel is significantly darker than the average it is denoted as character, otherwise it is classified as background.

2.3 Edge-Based Methods

In edge-based segmentation the main idea is to detect edges by designing a kernel matrix which resembles the edge structure. The image is convolved with the kernel and the pixels with a neighborhood similar to the kernel will give a strong output. Let $I(m,n)$ be the two-dimensional input image and $k(i,j)$ the kernel with which the image is convolved. The convolution of I with k is defined as follows:

$$I * k = \sum_{i=-I}^{I} \sum_{j=-J}^{J} k(i,j) \cdot I(m-i, n-j) \tag{2.3.1}$$

Figure 2.1 depicts the process of convolution of I with k. The center element of k is placed over the source pixel of I. On the output image, the source pixel is replaced by a weighted sum of itself and nearby pixels.

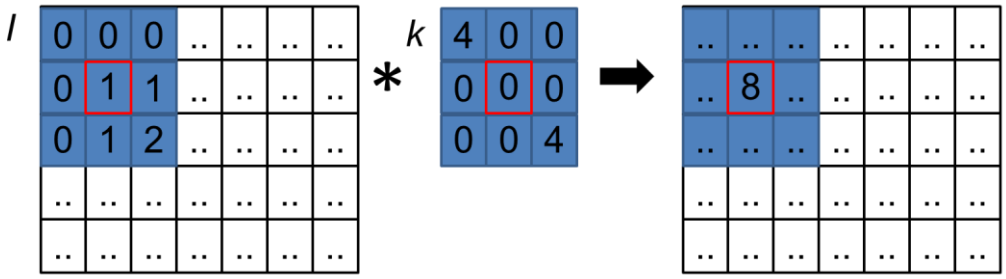

Figure 2.1: Convolution of image I with kernel matrix k.

The most typical elements for edge detection are the first and second derivatives. The first derivative is the natural candidate for edge detection since it provides a non-zero output across the entire edge transition. It is represented by the gradient operator G defined as:

$$G = \nabla I = (G_x, G_y) = \left(\frac{\partial I}{\partial x}, \frac{\partial I}{\partial y} \right) \tag{2.3.2}$$

Three discrete formulations widely utilized for edge detection are the Prewitt [32], Sobel [33] and Roberts [34] filter masks illustrated in Figure 2.2.

$$G_x = \begin{bmatrix} -1 & 0 & +1 \\ -1 & 0 & +1 \\ -1 & 0 & +1 \end{bmatrix}, \quad G_y = \begin{bmatrix} -1 & -1 & -1 \\ 0 & 0 & 0 \\ +1 & +1 & +1 \end{bmatrix}$$

(a)

$$G_x = \begin{bmatrix} +1 & 0 & -1 \\ +2 & 0 & -2 \\ +1 & 0 & -1 \end{bmatrix}, \quad G_y = \begin{bmatrix} +1 & +2 & +1 \\ 0 & 0 & 0 \\ -1 & -1 & -1 \end{bmatrix}$$

(b)

$$G_x = \begin{bmatrix} +1 & 0 \\ 0 & -1 \end{bmatrix}, \quad G_y = \begin{bmatrix} 0 & +1 \\ -1 & 0 \end{bmatrix}$$

(c)

Figure 2.2: (a) Prewitt, (b) Sobel and (c) Roberts filter masks.

The second derivative is utilized to determine the transition from low to high intensity or vice versa. It may also be used to verify the center of an edge by the zero-crossing of the two peaks. It is represented by the Laplacian operator defined as:

$$G^2 = \nabla^2 I = G_x^2 + G_y^2 = \frac{\partial^2 I}{\partial x^2} + \frac{\partial^2 I}{\partial y^2} \tag{2.3.3}$$

Due to the double differentiation, it is very susceptible to noise. In order to overcome this, the image is smoothed using a Gaussian filter defined as:

$$G_\sigma = -e^{-(x^2+y^2)/2\sigma^2} \tag{2.3.4}$$

The Laplacian and Gaussian operators are combined so as to form the Laplacian of a Gaussian (LoG_σ) operator defined as:

$$LoG_\sigma = -\left(\frac{x^2 + y^2 - \sigma^2}{\sigma^4}\right) \cdot e^{-(x^2+y^2)/2\sigma^2} \tag{2.3.5}$$

According to [35], Canny is 10.17%, 11.29% and 70.12% better than LoG, Sobel and Prewitt operator, respectively in terms of localization and signal response.

2.4 Region-Based Methods

The key idea is to start from a given seed point that represents a target pixel. The neighborhood of the pixel is classified as background or target region depending on a threshold value. The target region is segmented by a recursive search through the pixels which are classified as target. The most common region-based approach is the Watersheds Transform (*WST*) [36]. According to the latter, the image is visualized as a landscape where local minima are identified as seed points. Provided that rain falls over the landscape, the water will be collected from

a specific area surrounding each local minimum called catchment basin. Each catchment basin is considered to represent a target region. The boundaries generated between catchment basins are called watersheds.

A typical drawback of this approach is over-segmentation since all pixels of the image are assigned to catchment basins, i.e. no pixels are initially excluded from the procedure. Aiming at confronting over-segmentation, researchers have developed inner marker *WST* [37] as well as region merging methods [38]. The former incorporates markers in order to identify appropriate local minima, whereas the latter removes false watersheds generated after the segmentation process. Figure 2.3 depicts: (a) forested watersheds, (b) *WST* formulation in image segmentation.

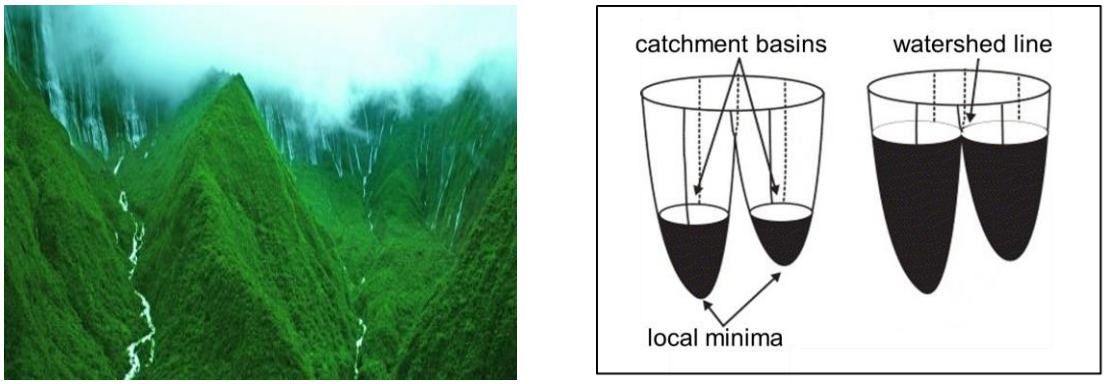

(a) (b)

Figure 2.3: (a) Forested watersheds, (b) *WST* formulation in image segmentation.

2.5 Deformable Models

Deformable models are related to the theory developed in Fluid Dynamics during the 80's. They are formulated according to an energy functional defined so as to be minimized when approximating target boundaries. The argument of the energy functional is typically a curve or surface, which evolves and defines the partitioning of the image based on external forces that hinge on image features such as intensity and/or texture. Additionally, internal constraints generate tension and stiffness, which preserve the smoothness and continuity of the model by

preventing the formation of sharp corners. The corresponding Euler-Lagrange equation constitutes a Partial Differential Equation (*PDE*), i.e. an iterative gradient descent algorithm, which guides the evolution towards the minimum (*see Appendix I*). The numerical implementation of the evolution is performed by the level set method, which endows the model with topological adaptability, i.e. splitting or merging, appearing or disappearing during the surface evolution.

2.5.1 Snakes

The original snake model was introduced by Kass, Witkin and Terzopoulos in 1988 [39]. A snake is a deformable curve defined in $\Re^2$ described as $s:[0,1]\to\Re^2$. The energy functional was suggested to contain two terms: the internal and external energy. The internal energy E_{int} is associated with smoothness and continuity and is defined as:

$$E_{\text{int}}(s)=\int_0^1 (a\cdot \| s_p \|^2+\beta\cdot \| s_{pp} \|^2)dp \tag{2.5.1}$$

where s_p and s_{pp} are the first and second derivative of s, respectively and a,β are the corresponding weighting parameters defining the elastic properties. The external energy E_{ext} is associated with image features and is defined as:

$$E_{ext}(s\,|\,I)=\int_0^1 P(s(p)\,|\,I)dp \tag{2.5.2}$$

where $P:\Re^2\to\Re$ is a function, called potential function, which hinges on image features. The total energy functional E_{total} being minimized is defined as follows:

$$E_{total}(s) = w_{\text{int}} \cdot E_{\text{int}}(s) + w_{ext} \cdot E_{ext}(s \mid I) \tag{2.5.3}$$

where w_{int}, w_{ext} are corresponding weighting parameters which control the fine balance between the two energy terms. The snake is initialized close to the target region and evolves until convergence towards a local minimum of E_{total} defined as (*see Appendix I*):

$$s_{\min} = \arg\min_{s}\{ E_{\text{int}}(s) + E_{ext}(s \mid I)\} \tag{2.5.4}$$

The numeric implementation of this minimization problem is obtained by sampling the continuous curve s at finite number of points $s_i = s(p_i) \in \Re^2$, $p_i = i \cdot \Delta p$, $i = 1,2,\ldots,N$. The discrete energy functional is obtained by replacing the integral with a sum and the derivatives with first and second order differences as follows:

$$E_{total}(s) = w_{\text{int}} \cdot \sum_{i=1}^{N} E_{\text{int}}(s_i) + w_{ext} \cdot \sum_{i=1}^{N} P(s_i) \tag{2.5.5}$$

where $E_{\text{int}}(s_i) = a \cdot \| s_{i+1} - s_{i-1} \|^2 + \beta \cdot \| s_{i+1} - 2s_i + s_{i-1} \|^2$. The total discrete energy functional is minimized by the gradient descent algorithm which yields to the following recursive equation:

$$s_i^{t+1} = s_i^t + w_{\text{int}} \cdot F_{\text{int}}(s_i) + w_{ext} \cdot F_{ext}(s_i) \tag{2.5.6}$$

where $F_{\text{int}}(s_i)$ and $F_{ext}(s_i)$ are the internal and external forces defined as:

$$F_{\text{int}}(s_i) = \frac{dE_{\text{int}}(s_i)}{ds_i}, \quad F_{ext}(s_i) = \frac{dE_{ext}(s_i)}{ds_i} \tag{2.5.7}$$

The model converges when an equilibrium between $F_{\text{int}}(s_i)$ and $F_{ext}(s_i)$ is reached. Figure 2.4 depicts the evolution of the snake model.

Although simple and efficient, snakes are not topologically adaptable, i.e. they are not capable of extracting multiple targets. This drawback triggered researchers to develop *AC* models represented by the level set method.

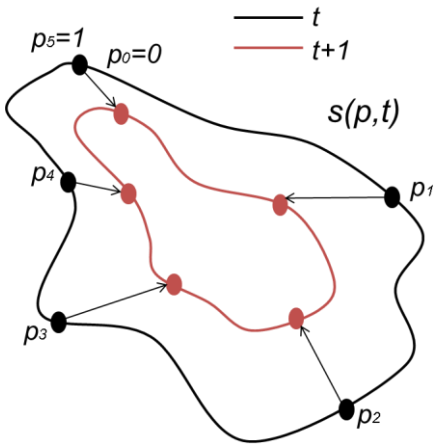

Figure 2.4: Evolution of the snake model.

2.5.2 The Level Set Method

The level set method uses an intrinsic representation of curve and surface evolution. This method was introduced in Fluid Dynamics at the end of the 70's. Osher and Sethian [40] provided a solid mathematical foundation with applications to gas dynamics and flame propagation that was introduced for image segmentation. This framework is highly appropriate for curve and surface evolution. Hence, it has become the standard way of representing interfaces evolution in Fluid Dynamics and Computer Vision, among other disciplines.

The curve C is represented implicitly via a Lipschitz function φ such that $C = \{(x,y) \in \Omega \subset \Re^2 \mid \varphi(x,y) = 0\}$. Curve evolution is given by the zero-level set function $\varphi(x,y,t)$. The motion of the curve is given by solving the following *PDE*:

$$\frac{\partial \varphi}{\partial t} = K \cdot |\nabla \varphi|, \quad \varphi(x,y,0) = \varphi_0(x,y) \tag{2.5.8}$$

where the set $\{(x,y) \,|\, \varphi_0(x,y) = 0\}$ defines the initial contour and $K = div\left(\frac{\nabla \varphi(x,y)}{|\nabla \varphi(x,y)|}\right)$ is the curvature of the level set. Figure 2.5 depicts a 3D representation of the level set.

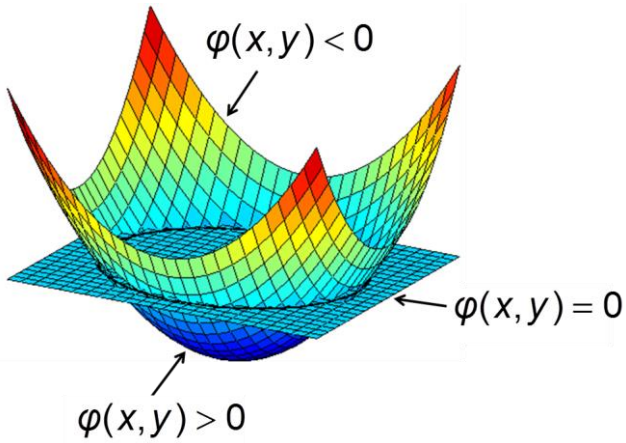

Figure 2.5: 3D representation of the level set.

2.5.3 Level Set Edge-Based *ACs*

The first level set edge-based *AC* model, called Geometric *AC* (*GAC*), was introduced by Caselles et al. [41]. The main idea was to utilize an edge detector function which depends on image gradient as follows:

$$g(|\nabla I|) = \frac{1}{1 + |\nabla G_\sigma * I|^2} \tag{2.5.9}$$

where $G_\sigma * I$ is the convolution of image I with the Gaussian G_σ. The evolution equation is represented by the level set method as follows:

$$\frac{\partial \varphi}{\partial t} = g(|\nabla I|) \cdot |\nabla \varphi| \cdot \left(div\left(\frac{\nabla \varphi}{|\nabla \varphi|}\right) + v \right) \tag{2.5.10}$$

where v is a balloon force. Even though *GAC* is topologically adaptable, it fails to converge to the target boundary because g is practically never zero on edges. In order to overcome this drawback, Caselles et al. [42] introduced an extended version of the *GAC* model, called geodesic *AC* model. Instead of utilizing the edge detector function described in Eq. (2.5.9), they proposed the more generic edge detector function $g(|\nabla I|)^2$. The evolution equation of the geodesic level set function is defined as follows:

$$\frac{\partial \varphi}{\partial t} = g(|\nabla I|)\cdot|\nabla\varphi|\cdot div\left(\frac{\nabla\varphi}{|\nabla\varphi|}\right) - \nabla g(|\nabla I|)\cdot\nabla\varphi \tag{2.5.11}$$

Equation (2.5.11) extends (2.5.10) in the sense that it includes a new term which increases the attraction of the contour towards the target boundary. It should be noted that, the balloon force can be incorporated so as to increase the convergence speed.

2.5.3.1 The Model of Li et al.

Li et al. [43] proposed to minimize an energy functional inspired by *GAC*, which is defined as:

$$\begin{aligned} E(\varphi) &= w_{reg}\cdot\int_{\Omega} p(|\nabla\varphi)dx \\ &+ a\cdot\int_{\Omega} g\cdot\delta_{\varepsilon}(\varphi)\cdot|\nabla\varphi|dx + w_{df}\cdot\int_{\Omega} g\cdot H_{\varepsilon}(-\varphi)dx \end{aligned} \tag{2.5.12}$$

where p a potential function $p:[0,\infty)\to\Re$, δ the Dirac function, H the Heaviside function, w_{reg} the regularization parameter, a a parameter that weights the second energy term which can be expressed as a line integral of the *GAC* model and w_{df} the data fidelity parameter. The level set evolution is determined as follows:

$$\frac{\partial \varphi}{\partial t} = w_{reg} \cdot div\left(d_p \cdot \frac{\nabla \varphi}{|\nabla \varphi|} \right) + a \cdot \delta_\varepsilon(\varphi) \cdot div\left(g \cdot \frac{\nabla \varphi}{|\nabla \varphi|} \right) + w_{df} \cdot g \cdot \delta_\varepsilon(\varphi) \tag{2.5.13}$$

Level set edge-based *ACs* have been widely utilized for boundary extraction [44]-[51]. However, they only incorporate localized information derived from the target region boundary, ignoring information related to the regions inside and outside of the target boundary. Hence, the contour might be delayed on edges associated with noise or artifacts. Aiming at encompassing more global information, region-based *ACs* were introduced.

2.5.4 Region-Based *ACs*

The first region-based *AC* model was proposed by Mumford and Shah in 1989 [52]. The key idea was to compute the optimal approximation of an image as a combination of regions of piecewise smooth intensities. The authors suggested the following energy functional:

$$E(u,C) = w_{reg} \cdot L(C) + w_{df} \cdot \int_\Omega |I(x,y) - u(x,y)|^2 dxdy + \int_{\Omega \setminus C} |\nabla u(x,y)|^2 dxdy \tag{2.5.14}$$

where u is a piecewise smooth approximation of I, $C \subset \Omega$ a 1D subset of edges and $L(C)$ the boundary length. The first term of Eq. (2.5.14) forces C to have minimal length, whereas the second term evokes u to approximate image I. The third term makes it more homogeneous.

2.5.4.1 The Chan-Vese Model

Chan and Vese [2] introduced a level set region-based *AC* model which was a particular case of the Mumford-Shah functional. According to this model, u is a

binary function which obtains two values: a) the average of I inside the segmented region and b) the average of I outside the segmented region. The energy functional that was suggested is defined as follows:

$$\begin{aligned} E(c_{in},c_{out},\varphi) = w_{reg}\cdot\int_{\Omega}|\nabla H(\ \varphi(x,y))|\,dxdy \\ -w_{df}\cdot\int_{\Omega}|\,I(x,y)-c_{in}(\ \varphi(x,y))\,|^2\cdot H(\ \varphi(x,y))dxdy \\ +w_{df}\cdot\int_{\Omega}|\,I(x,y)-c_{out}(\ \varphi(x,y))\,|^2\cdot(\,1-H(\ \varphi(x,y)))dxdy \end{aligned} \tag{2.5.15}$$

where c_{in}, c_{out} are the average values of I inside and outside of the contour, respectively defined as:

$$\begin{aligned} c_{in}(\ \varphi(x,y)) &= \frac{\int_{\Omega} I(x,y)\cdot H(\ \varphi(x,y))dxdy}{\int_{\Omega} H(\ \varphi(x,y))dxdy} \\ c_{out}(\ \varphi(x,y)) &= \frac{\int_{\Omega} I(x,y)\cdot(\,1-H(\ \varphi(x,y))dxdy}{\int_{\Omega}(\,1-H(\ \varphi(x,y)))dxdy} \end{aligned} \tag{2.5.16}$$

The evolution equation of the Chan-Vese model is defined as follows:

$$\begin{aligned} \frac{\partial\varphi}{\partial t} = w_{reg}\cdot\delta(\ \varphi(x,y))\cdot div\left(\frac{\nabla\varphi}{|\nabla\varphi|}\right) \\ -w_{df}\cdot(\ I(x,y)-c_{in}(\ \varphi(x,y)))^2 \\ +w_{df}\cdot(\ I(x,y)-c_{out}(\ \varphi(x,y)))^2 \end{aligned} \tag{2.5.17}$$

The advantages of this model is that the initial contour can be placed anywhere on the image and it can extract target regions with weak boundaries.

2.5.4.2 The Model of Bresson et al.

Bresson et al. [53] proposed to minimize the following energy functional based on the Chan-Vese model, in order to carry out the global minimization of segmentation:

$$E(u,c_{in},c_{out},w_{df}) = TV_g(u) + w_{df}\cdot\int_{\Omega}(c_{in}-I(x))^2-(c_{out}-I(x))^2dx \quad (2.5.18)$$

where $TV_g(u)$ is the weighted total variation energy of the function u with the weight function g, i.e. $TV_g(u)=\int g(x)\cdot|\nabla u|dx$. Region-based *ACs* have been extensively utilized in image segmentation [54]-[57].

2.6 Summary

In this chapter, the most representative image segmentation methods proposed in literature are introduced. The emphasis is put on deformable models since this thesis focuses on region-based *ACs.* Table 2.1 provides a comparison between the aforementioned segmentation methods pertinent to their benefits as well as their limitations.

Table 2.1: Comparison of segmentation methods

Segmentation Method	Benefits	Limitations
Thresholding	Simple implementation	Histograms with no sharp or well-defined peaks
Edge-Based	a) Algorithms are typically less complex	a) Fail in the presence of noise
	b) Successful on images of high contrast between target and background	b) Ineffective at curves and corners where gray level intensity values vary
Region-Based	a) Wider range of image features such as texture	a) Susceptible to the selection of seed points
	b) Insensitive to the presence of noise	b) Requirements for stopping criteria
	c) Use of spatial information	c) Over-segmentation
Deformable Models	a) Topologically adaptable	a) Sensitive to local minima
	b) Incorporation of smoothness constraints which provide robustness to noise	b) Sensitive to parameter settings

Aiming to overcome the last limitation of deformable models, one major goal of this thesis is to develop a novel framework which immunizes deformable models against empirical parameterization. Since it is unrealistic to automatically adjust all parameters of different deformable models, the novel framework focuses on region-based *ACs* due to their attractive merits on biomedical image segmentation.

CHAPTER 3

3. A NOVEL FRAMEWORK FOR AUTOMATED PARAMETERIZATION OF REGION-BASED *ACs*

3.1 Introduction

ACs are a rather mature image segmentation paradigm, with several variations proposed in literature (*see Chapter 2, § 2.5*). However, their parameterization remains a challenging, open issue, with strong implications on the quality, objectivity and robustness of the segmentation results. Very often, parameters are empirically adjusted on a trial and error basis, a process which is laborious and time-consuming, based on subjective as well as heuristic considerations. On one hand, non-expert users such as *MDs* and biologists require technical support since they are not familiar with the algorithmic inner mechanisms. On the other hand, parameter configurations empirically determined by image analysis experts are usually suboptimal and applicable to specific datasets [58].

This chapter introduces a novel framework for automated adjustment of region-based *AC* regularization and data fidelity parameters based on local image geometry information. Starting from the observation that these parameters and the eigenvalues of structure tensors are associated with the same orthogonal directions, local image geometry is encoded by the orientation coherence in edge regions. The latter can be mined by means of Orientation Entropy (*OE*), a measure which is an increasing function of the variability in edge orientation, obtaining low values in structured regions containing edges of similar orientations and high values in unstructured regions containing edges of multiple orientations. As a result, those forces that guide contour away from randomly oriented, high-entropy edge regions are amplified and iterations dedicated to misleading local minima are avoided, speeding up contour convergence. On the other hand, forces imposed within the proximity of structured edges, naturally related to target edge regions, are reduced, enhancing segmentation accuracy. It should be highlighted that, the convergence acceleration is a byproduct of the presented

framework, rather than its main motivation, which is the capability of *AC* self-parameterization.

3.1.1 Contribution

The contribution of the presented framework has several aspects:

1) It is unsupervised and may be treated as a 'black box': the regularization and data fidelity parameters are automatically adjusted. Hence, technical skills are not a prerequisite for the domain user, whereas the subjectivity of the results is reduced.

2) It is applicable to several types of images: it can be applied to natural, textured and biomedical images as well as to real-world photographs.

3) It does not require any *a priori* knowledge or learning considering the shape/size of the target region.

4) It guides contour away from high-entropy edge regions in order to avoid iterations dedicated to misleading local minima, by selectively amplifying data fidelity forces.

3.1.2 Related Work

Numerous approaches have been proposed in order to cope with the issue of empirical parameterization. Pluempitiwiriyawej et al. [59] and Tsai et al. [60], dynamically update *AC* parameters as contour evolves. This temporal dependency may lead to the propagation of early errors in the later contour evolution stages. In addition, in these approaches parameters are not spatially-varying, failing to capture local image features. Kokkinos et al. [61] proposed a statistical approach employing the *a posteriori* probabilities of texture, edge and intensity cues as contour weights in a locally adaptive manner. Nevertheless, their approach still requires technical skills by the domain user. Keuper et al. [62] and Liu et al. [63] presented a method for dynamic adjustment of *AC* parameters, applicable on the detection of cell nuclei and lip boundaries, respectively. Both methods require *a priori* knowledge considering the shape of the target region. Iakovidis et al. [64] and Hsu et al. [65] introduced a framework for optimization of

AC parameters based on genetic algorithms. However, these heuristic approaches converge slowly in locally optimal solutions. Allili et al. [66] proposed an approach for estimating hyper-parameters capable of balancing the contribution of boundary and region-based terms. In their approach, empirical parameter tuning is still involved. Yushkevich et al. [67] developed an application for level set segmentation of images of anatomical structures. Although their Graphical User Interface (*GUI)* is friendly to non-expert users, parameter settings are still empirically fixed.

3.2 Motivation

3.2.1 Structure Tensor Eigenvalues

The presented parameterization framework is motivated by the appealing properties of structure tensor eigenvalues [68]. The latter are capable of describing the orientation coherence in edge regions.

In what follows, an edge region containing edges of similar orientations is characterized as a *structured edge region*, whereas an edge region containing multiple orientations is characterized as an *unstructured* one. Structured edge regions usually surround actual region boundaries, whereas unstructured edge regions are associated with noise or artifacts. In this light, structure tensors are capable of providing maps of actual region boundaries and regions which correspond to noise or artifacts. This is depicted in Figure 3.1, which illustrates: (a) the structure tensor field of a test image, (b) a zoomed region which corresponds to an actual region boundary and (c) a zoomed region which corresponds to noise and artifacts. In the case of Figure 3.1(b), the edge region is characterized by edges of similar orientations, whereas in the case of Figure 3.1(c), the edge region is associated with multiple orientations. Based on the above remark, structure tensor eigenvalues are capable of identifying whether an edge region is associated with actual region boundaries, depending on the variability of the orientations of its edges.

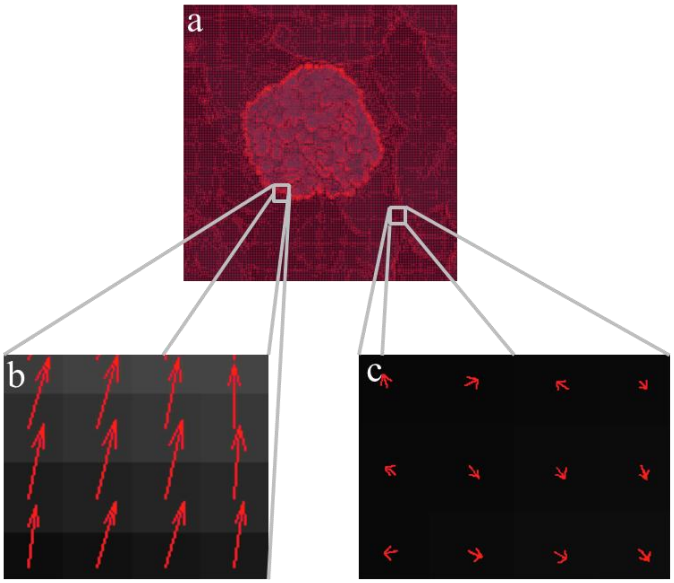

Figure 3.1: (a) Structure tensor field of a test image, (b) zoomed region which corresponds to an actual region boundary, (c) zoomed region which corresponds to noise and artifacts.

The Weickert's diffusion model [69] defines a structure tensor D as a symmetric, semi-positive 2×2 matrix (also called "second-moment matrix"), capable of describing the orientation coherence of an edge region as follows:

$$D = \nabla I \otimes \nabla I = \nabla I \cdot \nabla I^T \tag{3.2.1}$$

where D has an orthonomal basis of eigenvectors v_1, v_2 with $v_1 \| \nabla I$, $v_2 \perp \nabla I$ and λ_1, λ_2 are the corresponding eigenvalues given by:

$$\lambda_{1,2} = \frac{1}{2}(I_{xx} + I_{yy} \pm \sqrt{(I_{xx} - I_{yy})^2 + 4I_{xy}^2}) \tag{3.2.2}$$

where the $+$ sign belongs to λ_1. The eigenvectors form the orthogonal basis so that the variance of the projection on one of the tensor's axes is maximal and the projection on one of the remaining axes is minimal. The eigenvalues describe the orientation coherence of edge regions along the corresponding eigenvectors. It is

worth to be noted that, λ_1 is the principal eigenvalue and is longitudinal with respect to the principal axis of the elliptical tensor, whereas λ_2 is the minor eigenvalue and is vertical with respect to the same principal axis. Figure 3.2 depicts an elliptical representation of a 2D structure tensor.

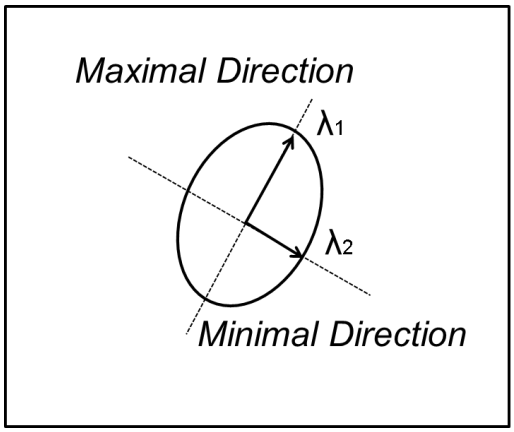

Figure 3.2: Elliptical representation of a 2D structure tensor.

3.2.2 Regularization and Data Fidelity Forces

The general form of the region-based *AC* energy functional can be written as follows (*see Chapter 2, § 2.5.4*):

$$E_{total} = w_{reg} \cdot E_{reg} + w_{df} \cdot E_{df} \tag{3.2.3}$$

where E_{reg} and E_{df} are the regularization and data fidelity energy terms, respectively, whereas w_{reg} and w_{df} are the corresponding weighting parameters. Energy terms are scalar functions, which most often discard any information associated with the orientation coherence of edge regions. However, forces guiding contour evolution are vectors, which are affected by the orientation coherence of edges.

Regularization forces imposed on a point of the contour are tangent, whereas data fidelity forces are vertical, attracting the contour towards target edges.

Providing that the contour is initialized as a circle, the regularization weight w_{reg} is longitudinal on a point of the contour, whereas the data fidelity weight w_{df} is vertical with respect to the same point. Figure 3.3 depicts a circular representation of an *AC* (red line).

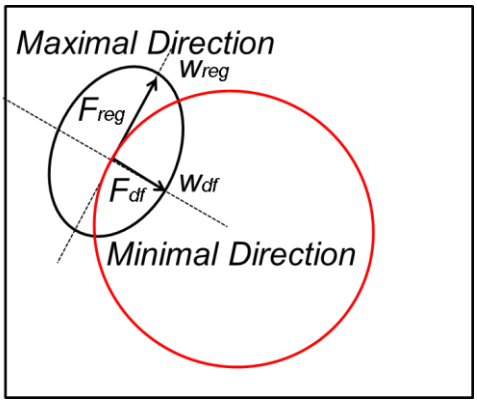

Figure 3.3: Circular representation of an *AC* (red line).

It is tempting to notice that, if we associate the eigenvectors of the elliptical tensor with the forces imposed on a point of the contour, the regularization weight w_{reg} corresponds to the same direction as the principal eigenvalue λ_1, whereas the data fidelity weight w_{df} corresponds to the same direction as the minor eigenvalue λ_2. This isomorphism indicates a link between the regularization and data fidelity parameters and the eigenvalues of the structure tensor.

3.3 Methodology

3.3.1 Orientation Coherence Estimation Using Multi-Directional Analysis

Inspired by the aforementioned observation, regularization and data fidelity parameters of region-based *ACs* are automatically adjusted in order to reflect the orientation coherence of edge regions, in a similar fashion to Weickert's diffusion model [69]. The orientation coherence is estimated by means of the orientation entropy (*OE)*. The latter is calculated on directional subbands in each scale of the Contourlet Transform (*CTr*) [70], which apart from intensity also represents textural information. *CTr* provides an inherent multi-directional filtering

mechanism, capable of filtering out randomly oriented edges associated with noise, artifacts and/or background clutter. Moreover, *CTr* is directly implemented in the discrete domain, as opposed to similar transforms, such as curvelets [71].

The Contourlet Transform (*CTr*)

Aiming at a sparse image representation, *CTr* employs a double iterated filter-bank, which captures point discontinuities by means of the Laplacian Pyramid (*LP*) and obtains linear structures by linking these discontinuities with a Directional Filter-Bank (*DFB*). The final result is an image expansion that uses basic contour segments. Figure 3.4 illustrates a *CTr* iterated filter-bank.

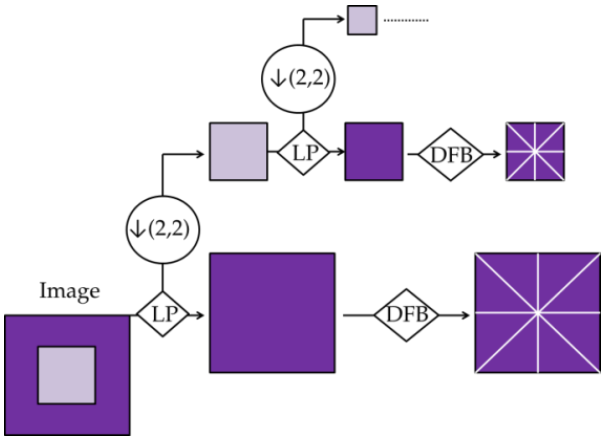

Figure 3.4: The *CTr* filter-bank. *LP* provides a downsampled low-pass and a band-pass version of the image. Consequently, a *DFB* is applied to each band-pass image.

The downsampled low-pass and band-pass versions of the image contain lower and higher frequencies, respectively. It is evident that, the band-pass image contains detailed information of point discontinuities which are associated with target edge regions. Furthermore, *DFB* is implemented by an *l*-level binary tree which leads to 2^l subbands. In the first stage, a two-channel quincunx filterbank [72] with fan filters divides the 2D spectrum into vertical and horizontal directions. In the second stage, a shearing operator reorders the samples. As a result, different directional frequencies are captured at each decomposition level. The number of iterations depends mainly on the size of the input image. The total number of directional subbands K_{total} is calculated as:

$$K_{total} = \sum_{j=1}^{J} K_j \tag{3.2.4}$$

where K_j is a subband *DFB* applied at the j^{th} level ($j = 1,2,...,J$).

Figure 3.5 depicts the *CTr* filter-bank of a sampled image grid, decomposed to the finest scale, which is partitioned into four directional subbands.

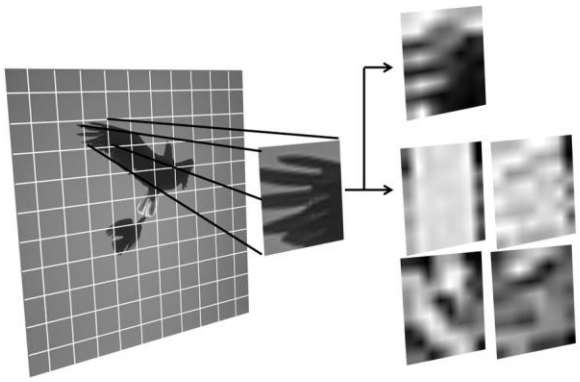

Figure 3.5: The *CTr* filter-bank of a sample grid decomposed to one level of *LP* and four band-pass directional subbands.

Each $q \times q$ image grid is fed into the *CTr* filter-bank through an iterative procedure and is decomposed into one pyramidal level, which is then transformed into four directional subbands: 0°, 45°, 90° and 135°. This grid must be appropriately selected in order to preserve the orientation of the main structures of the target region. The size of the $q \times q$ image grid is experimentally determined as the minimum of the negative power of two of the original image size, which still maintains at least an edge region. The band-pass directional subbands represent the local image structure. *OE* is calculated on each directional subband image I_{jk} as follows:

$$OE_{jk} = -\sum_{n=1}^{N_{jk}} \sum_{m=1}^{M_{jk}} p_{jk}(m,n) \cdot \log p_{jk}(m,n) \tag{3.2.5}$$

$$p_{jk}(m,n) = \frac{|I_{jk}(m,n)|^2}{\sqrt{\sum_{n=1}^{N_{jk}}\sum_{m=1}^{M_{jk}}[I_{jk}(m,n)]^2}} \quad (3.2.6)$$

where OE_{jk} is the *OE* of the subband image I_{jk} in the k^{th} direction and the j^{th} level of decomposition, M_{jk} is the row size and N_{jk} the column size of the subband image. Among the *OE* values calculated for each subband image, the maximum value OE_{jk} of the most informative direction k is calculated and assigned to all pixels of each grid. The result is considered as an *OE* 'heatmap' reflecting local image structure.

OE obtains high values in cases of unstructured edge regions, which are associated with noise and artifacts and low values in cases of structured edge regions, which are associated with the actual region boundaries. Figure 3.6(a) depicts a schematic representation of edge regions consisting of single and multiple orientations, whereas Figure 3.6(b) depicts the *OE* behavior on each edge region of Figure 3.6(a).

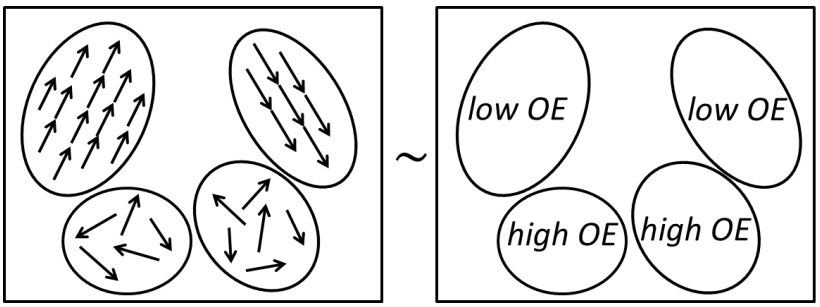

(a) (b)

Figure 3.6: Schematic representation of: (a) edge regions, (b) *OE* behavior on each edge region.

3.3.2 Automated Parameter Adjustment

Regularization and data fidelity parameters are matrices of the same dimensions as the original image, and are calculated according to the following equations:

$$w_{reg}^{auto} = a \times \left(\frac{1}{w_{df}^{auto}}\right), \quad w_{df}^{auto} = \arg_{I_{jk}} \max(OE_{jk}(I_{jk})) \tag{3.3.1}$$

where *a* depends on the dimensions of the image grid. The core idea is to guide the active contour towards structured, target edge regions in the early stages of evolution by appropriately amplifying data fidelity forces in randomly oriented, high-entropy regions. As a result the contour will be repelled and iterations dedicated to misleading local minima will be bypassed, speeding up contour convergence towards target edges. It should be highlighted that both parameters are calculated *only once*. The aim is to guide the contour directly to target edge regions, already from the beginning and to prevent any erroneous behavior during evolution by 'constantly reminding' where the target edge regions lie.

Figure 3.7 illustrates: (a) an artificial bipartite textured image consisting of a target region and the initial contour (green circle), (b) a sketch of data fidelity forces on an iteration of contour evolution, where F_{df}^{A} (white arrows) relate to edge regions which correspond to noise and F_{df}^{B} (black arrows) reflect structured target edge regions and, (c) a sketch of these forces on a next iteration of contour evolution, where F_{df}^{A} is amplified (long white arrows) and F_{df}^{B} is reduced (short black arrows).

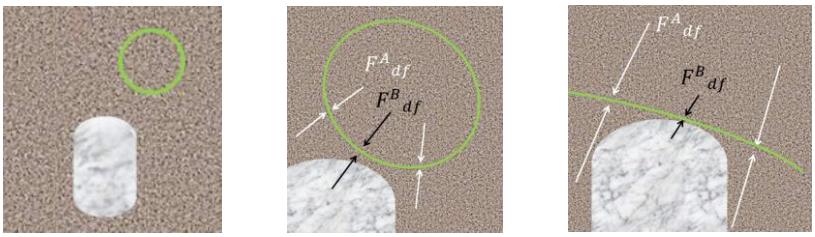

(a) (b) (c)

Figure 3.7: (a) Artificial bipartite textured image consisting of a target region and the initial contour (green circle), (b) sketch of data fidelity forces on an iteration of contour evolution, (c) sketch of data fidelity forces on a next iteration of contour evolution.

Equation (3.3.1) is an interpretation of *OE* values adaptive to the orientation of data fidelity forces. Apart from separately adjusting each parameter, the presented framework also achieves a balanced trade-off between regularization and data fidelity parameters. It should also be noticed that, the automated parameterization is spatially-adaptive, so as to reflect local variations over the image.

It can be mentioned that, the presented framework is not confined in using *CTr* and could also embed alternative multi-scale, multi-directional approaches for image representation. In any case, the encoded local image geometry will allow the formation of *OE* 'heatmaps', which can be used to weight regularization and data fidelity forces. The pipeline of the presented framework is portrayed in the block diagram of Figure 3.8.

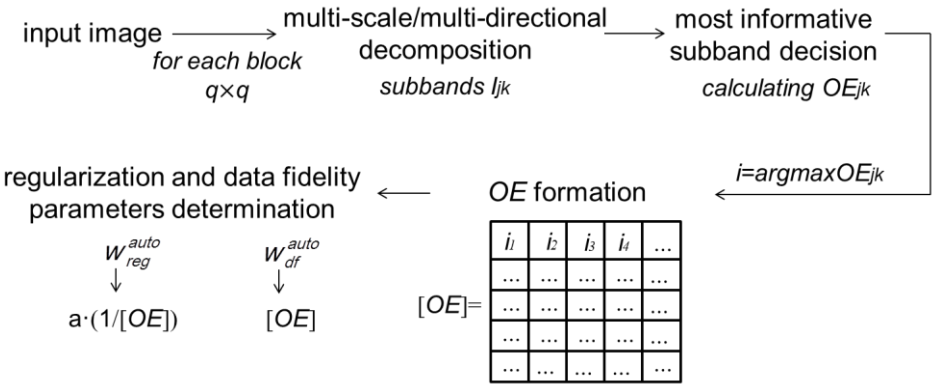

Figure 3.8: Block diagram of the pipeline of the presented framework.

3.4 Experimental Evaluation

The presented framework has been integrated into two region-based [2], [53] and one hybrid [43] *AC* model, in order to evaluate the segmentation performance of the automated versus empirical parameterization. The well-known Chan-Vese model [2] has been implemented in Matlab [73], whilst Matlab codes of the models of Li et al. [43] and Bresson et al. [53] can be downloaded from the authors' homepages [74] and [75], respectively. The '9-7' biorthogonal filter for the multi-scale and multi-directional decomposition stage of *CTr* is applied [76]. The results of the automated versions were compared to those obtained by the original, empirically parameterized algorithms. Apart from experiments on the Berkeley segmentation dataset [1] and on test images obtained by various datasets [77], [78], additional experiments were conducted on the Amsterdam Library of Object Images (*ALOI*) database [79].

It should be stressed that, rather than comparing one *AC* method with another, the experiments to follow aim to evaluate the effectiveness of the presented parameterization framework by examining whether the segmentation performance of the automated version is *at least comparable* to the one obtained by the empirically fine-tuned version.

Figure 3.9 illustrates: (a),(b) test images obtained by the Berkeley segmentation dataset [1], (a_1),(b_1) ground-truth images and (a_2),(b_2) segmentation results of the presented framework. Aiming to evaluate the obtained results, the region overlap measure, known as the Tanimoto Coefficient (*TC*) [80], is considered:

$$TC = \frac{N(A \cap B)}{N(A \cup B)} \tag{3.4.1}$$

where A is the region delineated by the segmentation method under evaluation, B is the ground truth region and $N(\,)$ indicates the number of pixels of the

enclosed region. The results of Figure 3.9(a_2) and (b_2) correspond to *TC* values of 90.3% and 88.7%, respectively.

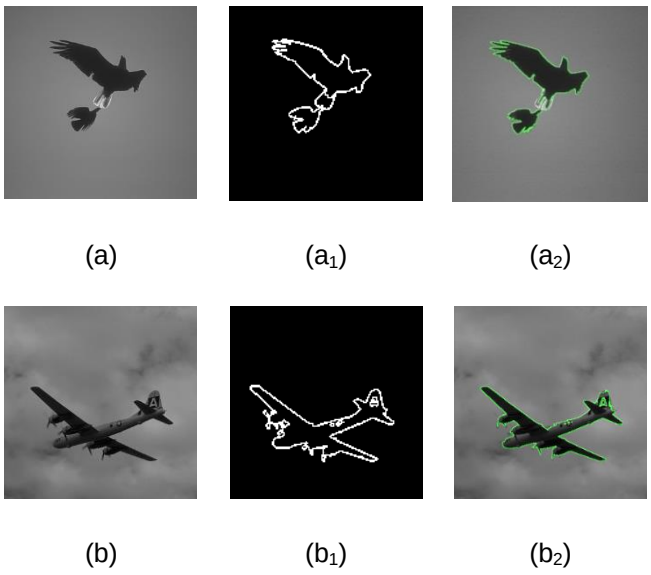

(a) (a_1) (a_2)

(b) (b_1) (b_2)

Figure 3.9: Segmentation based on local image geometry: (a),(b) original test images obtained by [1], (a_1),(b_1) ground-truth images and (a_2),(b_2) segmentation results of the presented framework.

3.4.1 Integration into the Chan-Vese Model

The Chan-Vese model [2] determines the level set evolution by minimizing the energy functional and solving Eq. (2.5.17). For the empirical case, the optimal parameters are set according to the original paper [2]. For the presented framework, the regularization and data fidelity parameters are automatically calculated according to Eq. (3.3.1).

The segmentation performance of the Chan-Vese model for both automatically and empirically parameterized versions is evaluated on test images obtained by the authors of [77], [78] utilizing the database of [1]. The test images contain a foreground object of interest over an inhomogeneous background. The contour is initialized as a closed circle with the same center and radius for all test images and for both automatically and empirically parameterized versions, so as to ensure consistency.

Figure 3.10 illustrates the contour obtained on two test images, for the second as well as for the final iteration. The first image contains a target region of high average intensity over a darker background, whereas the second image contains a dark target region over a brighter background. Yellow color is used for the initial contour in both versions whereas blue and green colors are used for the contours obtained by empirical and automated version, respectively on the second and final iteration. The dilation operator has been used to morphologically reconstruct contours and enhance image appearance. In the case of the first image, the automated version converges faster to the target boundaries since the forces guiding contour evolution are appropriately amplified in high-entropy edges associated with noise (*see Figure 3.7*). In the case of the second image, the empirical version is delayed on the misleading local minima of the "land parcel" and converges to erroneous boundaries. This can be explained by the gross nature of the Chan-Vese model, which is guided by region-based forces and thus, is delayed on misleading local intensity minima associated with brighter background clutter. On the contrary, the automated version is guided by region-based forces, as well as by local geometry information, incorporated in the parameters matrices and is capable to identify the actual target edge regions.

Aiming to evaluate the convergence rate of both versions, we define the Difference of Mean Intensity values (*DMI*) between inside and outside region terms and implement the following algorithm:

$\forall$ Iteration *i*

1. Calculate inside $|I(x,y)-c_{in}|^2$ and outside $|I(x,y)-c_{out}|^2$ region terms.

2. Normalize and quantize both terms in the range [0,255].

3. Calculate mean values.

4. Calculate *DMI.*

Figure 3.11 depicts *DMI* calculated for the early stages of evolution of the automated versus empirical version of the Chan-Vese model presented in Figure 3.10. It can be observed that, *DMI reaches higher values in the automated case in the early stages of contour evolution*. Again, this is explained by the fact that the forces guiding contour evolution are appropriately amplified in edge regions associated with noise. Figure 3.12 compares the segmentation performance for the early stages of evolution of the automated versus empirical version in terms of *TC (see Eq. (3.4.1))*.

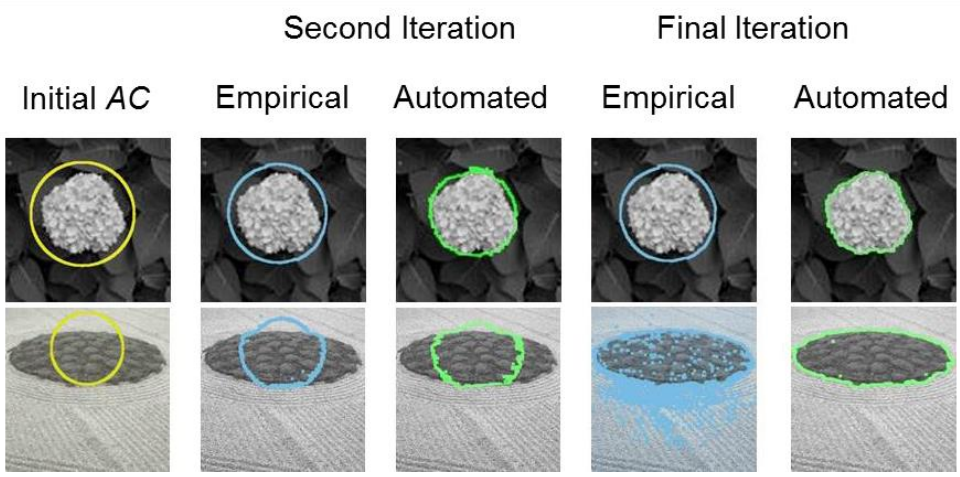

Figure 3.10: Examples of contour evolution of the Chan-Vese model [2]. Yellow color is used for the initial contour in both versions; blue and green colors are used for the contours obtained by the empirical and automated version, respectively.

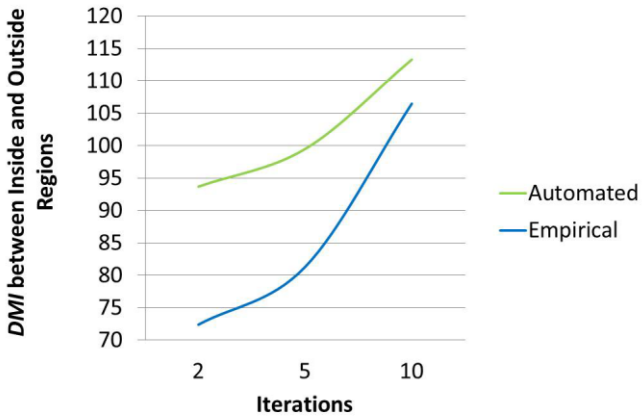

Figure 3.11: *DMI* calculated for the early stages of evolution of the automated versus empirical version of the Chan-Vese model, presented in Figure 3.10.

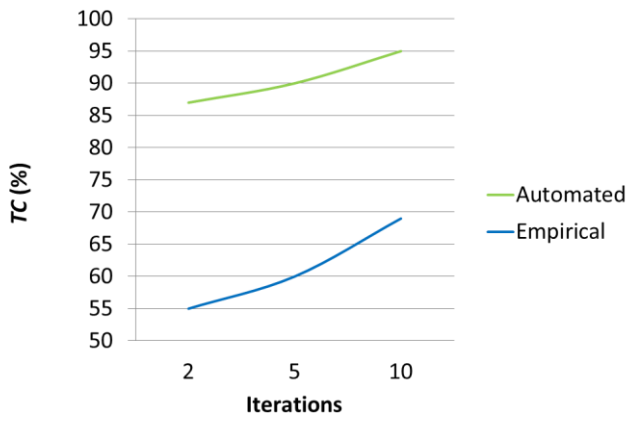

Figure 3.12: *TC* for the early stages of evolution of automated versus empirical version presented in Figure 3.10.

3.4.2 Integration into the Model of Bresson et al.

The model of Bresson et al. [53] minimizes the energy functional described in (2.5.18). For the empirical case, the data fidelity parameter is set according to the original paper [53]. For the presented framework, the data fidelity parameter is automatically calculated according to Eq. (3.3.1). The model of Bresson et al. is evaluated on test images obtained by the first author's homepage [75]. Figure 3.13 presents segmentation results for 'cheetah' and 'zebra' textured images. The final contour satisfies:

$$\{(x,y) \in \Omega \,|\, I^{final}(x,y) > 0.5 \ \} \tag{3.4.2}$$

Magenta and green colors correspond to empirical and automated version, respectively. It is evident that, both versions converge to the actual target boundaries, resulting in *comparable segmentation accuracy*. It should be pointed out that, the empirical version of the model of Bresson et al. convexifies energy in order to compute a global minimizer. The automated version captures local geometry information correctly and converges to the actual target edge regions.

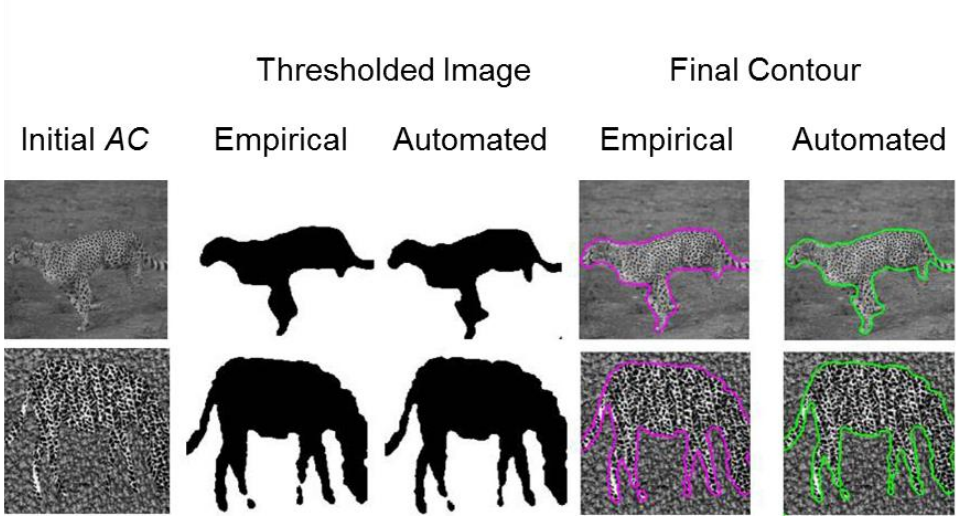

Figure 3.13: Segmentation results of the model of Bresson et al. [53]. Magenta and green contours correspond to empirical and automated parameterization, respectively.

3.4.3 Integration into the Model of Li et al.

The presented framework has also been applied on the model of Li et al. [43] so as to evaluate it on a hybrid energy functional, i.e. consisting of region-based as well as edge-based terms. Li et al. minimize the energy functional described in Eq. (2.5.12). For the empirical case, the optimal fixed parameters are set according to the original paper [43]. For the presented framework, the optimal fixed value of a is maintained, whereas the regularization and data fidelity parameters are automatically calculated according to Eq. (3.3.1). It should be noted that, the optimal fixed value of a is maintained since it is unrealistic to automatically adjust all *AC* parameters of different *AC* variations.

In a similar fashion, the segmentation performance of both automated and empirical versions of the model of Li et al. is evaluated on test images obtained by the author's homepage [74]. Figure 3.14(a) and (b) illustrate a test image and the initial level set function, respectively, whereas the images below present contours obtained in three different iterations, as well as the final level set functions. The latter exhibit the shape of a signed distance function in the vicinity of the zero level set and a flat shape outside this vicinity. Red and green colors correspond to empirical and automated parameterization, respectively. It should be pointed out that, the level set evolution is applied without re-initialization and is

guided also by edge-based forces. It is evident that the segmentation results of the empirical and automated versions are *comparable*.

Figure 3.15 depicts *TC* results of automated versus empirical version, based on contour evolution presented in Figure 3.14. In the automated version, *TC reaches slightly higher values from early iterations*. One should take into account that, with empirical parameterization it is always possible to set "optimal" parameters after laborious, time-consuming experimentation. The presented framework is capable of obtaining *comparable results in an automated fashion*.

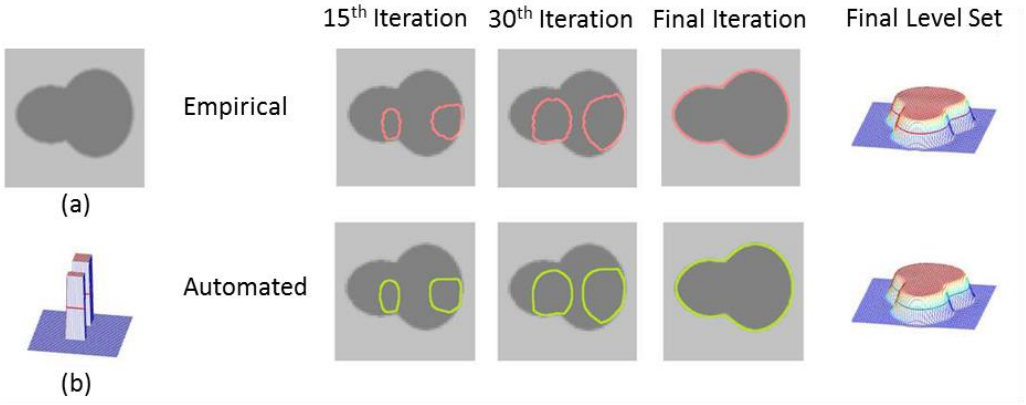

Figure 3.14: Evolution of segmentation for the model of Li et al. [43]. Red and green contour corresponds to empirical and automated parameterization, respectively, (a) original test image, (b) initial level set function.

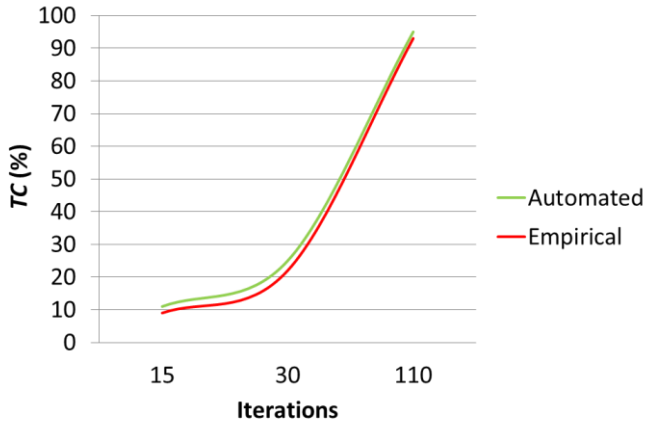

Figure 3.15: *TC* for the early stages of evolution of automated versus empirical model presented in Figure 3.14.

The presented framework is also tested on images obtained by the *ALOI* database [79] in order to enable evaluation on a large benchmark dataset. Figure 3.16 illustrates segmentation results for both automated and empirical parameterization. The first and second columns illustrate test images and their ground truth, respectively. The third column provides the iteration number, for which the automated version converges. The fourth and fifth columns illustrate segmentation results of the automated and empirical case for that iteration, respectively. The sixth and seventh columns illustrate the iteration number for which the empirical version converges and the segmentation results for that iteration, respectively. All test images were recorded with varying viewing and illumination angles, resulting in challenging shades. Several images of *ALOI* database, including the illustrated 'teapot', 'bear', 'basket' and 'wire', contain intensity-based information whereas some also contain textured regions, as is the case with 'basket' and 'wire'. It is evident that after convergence, the segmentation results of both automated and empirical versions are *comparable*. However, in the empirical case, the contour is delayed in misleading local intensity minima associated with shades and hence, *requires approximately 10-20 times more iterations in order to converge*. On the contrary, in the automated case, forces which guide contour evolution are appropriately amplified in high-entropy edges, accelerating convergence. The automated case achieves an average *TC* value of 96.9±1.6%, which is comparable to the *TC* value obtained by the empirical case. However, the empirical case achieves a *TC* value of 58.4±14.3% in the same iteration that the automated version has converged, with regards to all *ALOI* images tested.

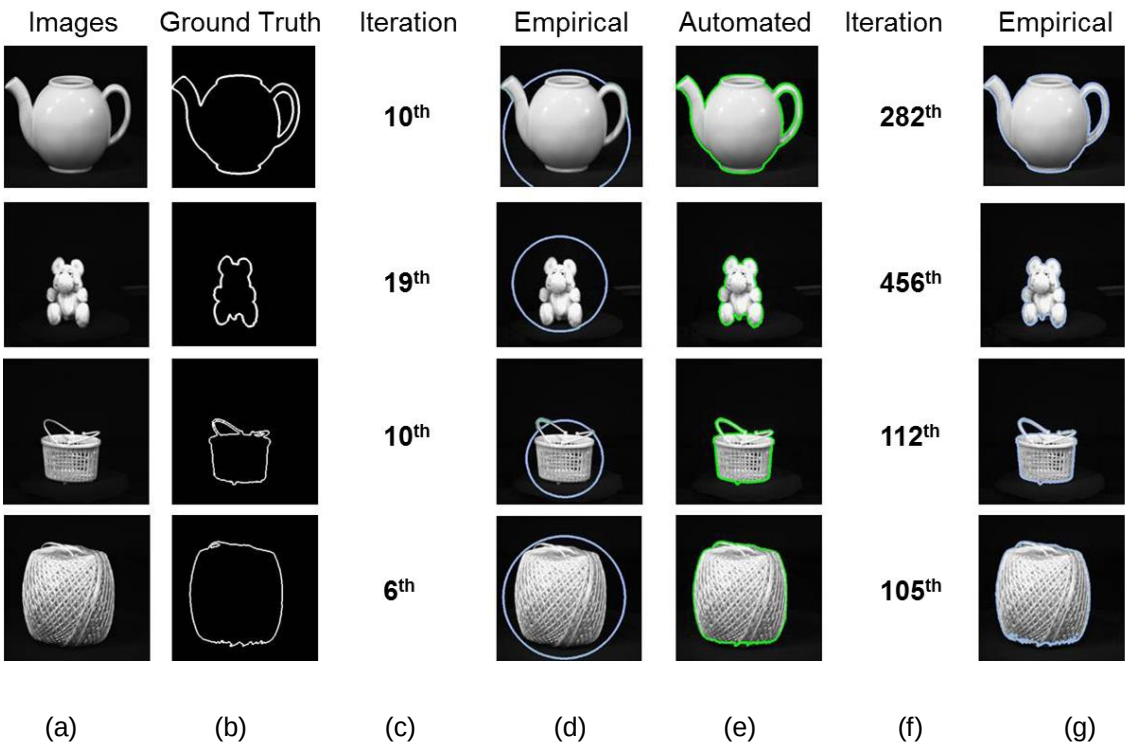

Figure 3.16: Segmentation results of the automated and empirical case. (a) test images obtained by *ALOI* database [79], (b) corresponding ground truth images, (c) final iteration in the automated case, (d) segmentation results of the empirical case for (c), (e) segmentation results of the automated case, (f) final iteration in the empirical case, (g) segmentation results of the empirical case for (f).

3.5 Summary

This chapter presents a novel framework for automated regularization and data fidelity parameterization of region-based *ACs*, which is motivated by the observation that the weighting factors of regularization and data fidelity terms and the eigenvalues of structure tensors are associated with the same orthogonal directions. The presented framework is unsupervised and does not require technical skills from the domain user. In addition, it is applicable to several imaging modalities and does not require prior knowledge on the target regions. Moreover, it avoids iterations dedicated to misleading local minima, speeding up contour convergence.

The presented framework has been experimentally evaluated on various datasets of natural, textured and real-world images. Its segmentation performance was

compared with two state-of-the-art region-based and one hybrid empirically parameterized *AC* variations. The experimental results demonstrate that it is capable of *maintaining a segmentation quality comparable to the one obtained with empirical parameterization, yet in an automated fashion*.

CHAPTER 4

4. PROTEOMICS AND MEDICAL IMAGES

4.1 Introduction

This chapter provides a coherent overview of proteomics and medical images, which were utilized in our segmentation experiments. The provided information covers the biomedical background as well as the physics-based principles of the acquisition devices, which generate these images. Furthermore, several factors which obstruct the segmentation task are thoroughly examined.

4.2 Proteomics Images

Proteomics images, called electrophoretograms, are the result of proteins' electrophoresis, which provides the movement of charged particles over time on a gel. It reflects the phenotype, i.e. the biochemical properties of an organism at a given time under a specific condition. On such images, proteins appear as spots over a grey level surface. A proteomics image consists of a few hundred up to several thousands of protein spots and each individual protein spot represents a single protein. The amount of each protein can be estimated by the cumulative intensity of the associated protein spot region. Ideally, each protein spot is represented by a Gaussian distribution. In literature, there are two types in proteomics image representation. In one case, proteins are represented as white spots over a dark surface whereas in the other case, proteins are represented as black spots (typically smaller in size) over a light surface. In the former case, protein intensities reach maximum values whereas surface intensities reach minimum ones. Figure 4.1 depicts the two types of proteomics image representation.

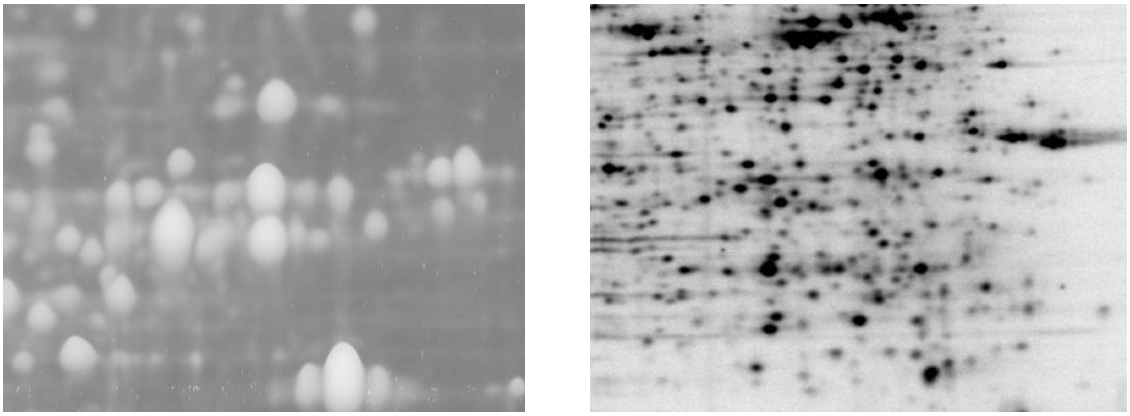

(a) (b)

Figure 4.1: Two types of proteomics image representation, (a) proteins are represented as white spots over a dark surface, (b) proteins are represented as black spots over a light surface.

In this thesis, proteomics image analysis is conducted on the former image representation in accordance with the datasets provided by the Biomedical Research Foundation of the Academy of Athens. In addition, the provided proteomics images have sufficient resolution of 2000×3000 pixels and 16-bit image depth in agreement with the databases utilized in proteomics research such as SWISS 2D-PAGE [81] and PROSITE [82]. A resolution of 300 dpi is generally sufficient for gel analysis. It should be noted that, by augmenting resolution and depth, the computational analysis time and cost are increased.

4.2.1 Biological Background

The structural and functional core units of all known organisms are the cells. Various organisms, such as bacteria, consist of a single cell which performs all functions required for living whereas others, such as humans, consist of multiple cells which differentiate and undertake specific tasks as part of more complex ones. The former types of cells are called prokaryotic whereas the latter are called eukaryotic. Unlike prokaryotic, eukaryotic cells consist of the membrane-delineated compartment called nucleus which contains the cell's genetic material defined as the genome. Most organisms' genetic material is DeoxyriboNucleic Acid (*DNA*) however; few viruses, such as HIV, consist of RiboNucleic Acid

(*RNA*). The biological information of an organism is encoded in *DNA* or *RNA* sequences. *DNA* sequences consist of discrete units called structural genes which code for proteins [83].

Proteins were discovered in the 19th century by Jöns Jakob Berzelius [84] who named them “πρωτειοξ” in Greek, meaning “of primary importance”. They are fundamental components since they participate in core cellular processes such as cell motility, *DNA* synthesis, signaling and mitosis. Proteins are organic complex macromolecules called polypeptides composed of amino acids linked to each other with peptide bonds. An amino acid structure incorporates an amino group, a carboxylic acid group and a side chain which are all attached to a central carbon atom (*see Figure 4.2*). The amino acid’s side chain and protein’s three-dimensional structure highly affect the hydrophobic (water-repelling) or hydrophilic (water-soluble) biochemical properties as well as the way of the polypeptide’s folding, respectively. Protein denaturation occurs when the structure is destroyed and protein unfolds. As a result, it is no more capable of fulfilling required tasks [85].

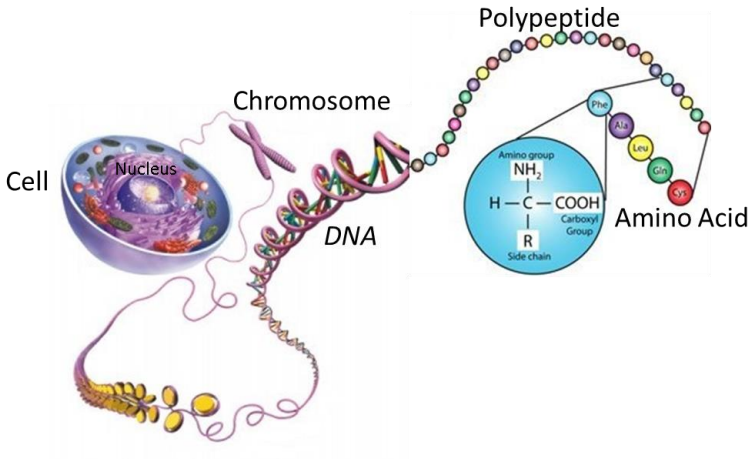

Figure 4.2: From cell to amino acid structure.

Protein synthesis requires two main processes, transcription and translation. During the first process, *DNA* is transcribed to messenger-*RNA* (*mRNA*) which holds essential information for protein synthesis whereas during the second, *mRNA* is further translated by transfer-*RNA* (*tRNA*) to a protein. The complete set

of proteins expressed in a cell is named as proteome. Post-Translational Modifications (*PTMs*) refer to differences between a translated polypeptide sequence and the final protein. They are crucial functions since they are responsible for alterations in biological activity of polypeptides. For instance, proteins are known to be constructed from 22 amino acids [86].

4.2.2 Introduction to the Field of Proteomics

Genomics revolution was only the beginning of an enormous metamorphosis of life sciences. The analysis of the proteome has provoked even more radical changes in biological research. Most biological functions are carried out by proteins that interact with each other within a complex biological system. The proteome is defined as a protein complement in a specific cell, tissue or organism. However, it is more complicated than the genome since a gene may encode a number of different proteins. In other words, genes are just the instructions for making proteins whereas proteins make life [87].

The field of proteomics corresponds to the large-scale analysis of proteins expressed in a cell, tissue or biological organism. Numerous technologies are involved with the aim to identify and quantify proteins as well as to decode their *PTMs* and inner interactions [88]. Unlike the genome, proteome provides more vital information considering the processes that occur within the cell. By examining biological samples stemmed from cells at different stages of development, in the presence of drugs or upon infection by a pathogen, crucial information on alterations in protein expression profiles can be derived [89]. This information is essential for numerous biological applications such as the development of prognostic and diagnostic systems as well as the identification of personalized drugs and vaccine targets. It should be mentioned that, pharmaceutical companies spend an enormous amount of resources in animal experiments in order to develop new “intelligent” drugs. Proteome analysis is expected to yield disease markers called biomarkers for disease diagnosis and therapy monitoring. Biomarkers may be genes as well as proteins. They are measurable indicators which reflect a specific normal biological state, pathogenic process or pharmacologic response to a therapeutic intervention [90].

Proteome analysis was originally performed in the mid-seventies by O' Farell [91] who produced protein maps from Escherichia Coli and mouse cells. He detected about 1100 different proteins by means of a workhorse technique called Two-Dimensional Gel Electrophoresis (*2D-GE*) [92], [93] and was able to investigate the phenotype of an organism on the level of protein expression. The objective in *2D-GE* is to identify differentially expressed proteins when comparing healthy and diseased biological samples in order to discover proteins that have appeared, disappeared, increased and decreased in size.

4.2.3 Two-Dimensional Gel Electrophoresis (*2D-GE*)

In *2D-GE*, an indicative portion of the total protein component of a cell is resolved and information about different *PTMs* attributed to proteins is provided. The biological sample under investigation is separated in two independent dimensions according to two high resolution properties: isoelectric point (*pI*) and molecular weight (*Mw*). *2D-GE* consists of biochemical and electrokinetic processes namely: a) labeling, b) denaturation, c) isoelectric focusing, d) incubation, e) molecular weight separation and f) image digitization [94].

During the labeling process, cells are cultured in a medium consisting of radioactive amino acids such as methionine (^{35}S) and formaldehyde (^{14}C). These amino acids, which enable the detection of radioactively labeled proteins, are incorporated into the biological sample. Various anionic dyes such as coomassie, silver or fluorescent can also be utilized. The key scope is to provide an effective linear response over as broad a range of concentrations as possible. By labeling the sample with radioisotopes, an image with higher resolution is generated and even low-abundance proteins can be detected. Consecutively, the proteins of the biological sample are denatured in a detergent lysis buffer comprising urea and thiourea [95]. The former is effective in disrupting hydrogen bonds whereas the latter is appropriate for destroying hydrophobic interactions. As a result, proteins' structures are destroyed, proteins unfold and aggregations together with proteolysis are highly prevented. Furthermore, non-protein components such as artifacts are removed [96].

During Isoelectric Focusing (*IEF*), the unfolded proteins are placed on an Immobilized pH Gradient (*IPG*) gel strip [97]. The pH scale reflects the amount of hydrogen ions and ranges from 0 to 14 units with 7 being neutral. Assuming that the pH scale is less or more than 7, the gel is acidic or basic, respectively. Proteins are differently charged and an electric field is applied across the gel strip in order to provoke their migration towards the electrode of the opposite charge in the first dimension. The migration rate hinges on the complex relationship between the electrophoresis system and the proteins. As a result, each protein will be immobilized at that pH value where the number of positive and negative charges on the protein is the same. This value is called *pI* and refers to protein state of equilibrium. The pH scale utilized in most experiments ranges from 4 to 7. Most proteins occupy different positions since they have different charges. Nevertheless, some proteins tend to obtain the same *pI* and thus, a second separation is required so as to identify individual proteins. The incubation process which follows, prepares the gel under investigation. The gel is being washed in a detergent called Sodium Dodecyl Sulfate (*SDS*), which aims to maintain the same charge on all proteins [98].

During the *Mw* separation (*SDS-PAGE*), the *IPG* gel strip is placed on the upper edge of a thin polyacrylamide gel slab (matrix). The amount of polyacrylamide affects the pore size and the sieving properties of the gel slab. An electric field is applied in the tangent direction again provoking migration in the presence of *SDS*. The electrical force imposed on each protein is the same for all of them since they have the same charge. The electrophoretic mobility of proteins is primarily determined by the volume fraction of pores. Hence, large proteins meet more resistance and migrate slower compared to smaller ones. The electric field is no longer applied and the process ends when small proteins reach the bottom of the gel slab. The result is a two-dimensional map of proteins obtaining unique coordinates (*pI*, *Mw*) [99]. The gel slab is dried down and autoradiography is applied for protein visualization. Staining procedures also take place in the case that coomassie, silver and fluorescent dyes are utilized. It is of mandatory importance that these dyes are compatible with the subsequent Mass Spectrometry (*MS*) [100] analysis. Since gels do not last forever, it is essential that the data is stored in a format easily maintained. Hence, gel data is mutated to

image data. Figure 4.3 illustrates the two main processes of *2D-GE*, i.e. *IEF* and *SDS-PAGE*.

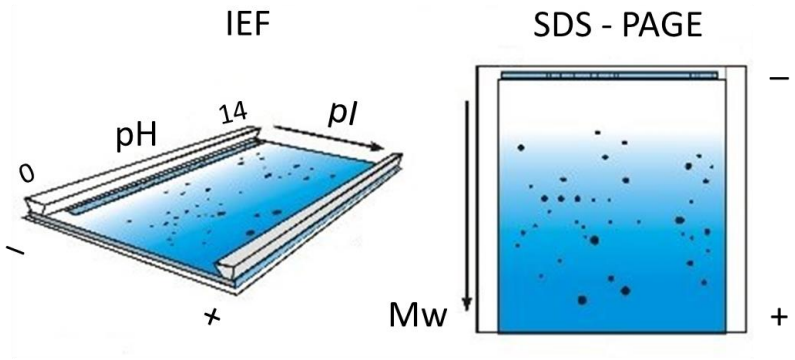

Figure 4.3: *IEF* and *SDS-PAGE* of *2D-GE*.

During image digitization, the gel is transferred to high resolution scanners, laser densitometers, fluorescent and phosphor imagers or charged couple device cameras so as to be digitized into images. The radioactively labeled proteins excite the electrons of the atoms to a high energy state. The electrons return to their equilibrium state emitting electro-magnetic radiation captured by an imaging technology device which in return generates the digital image [101].

Several important merits of *2D-GE* should be highlighted. First and foremost, *2D-GE* is a robust technique which enhances reproducibility of protein expression provided that it is conducted under a defined temperature. Secondly, it is capable of investigating thousands of proteins on a single gel at the same time. Finally, by introducing *IPGs* and narrowing the pH gradient range, high resolution could be achieved. It should be noticed that two proteins may be resolved provided that their *pI* values differ by 0.001 units [102].

Even though *2D-GE* is performed by expert biologists, the processes and the final results are prone to subjectivity and human errors. There are numerous challenges in *2D-GE* images derived by human errors as well as by the inner biochemical properties of the biological sample which reduce image quality. Common unwanted factors that influence the results emerging from the analysis

of *2D-GE* images are: the presence of noise, dust particles, fingerprints, cracks in the surface and other artifacts such as streaks or tails that are not related to proteins. The main challenges in *2D-GE* images are the inhomogeneous background and the existence of faint and overlapping spots.

4.2.4 Challenges in *2D-GE* Images

One major challenge in *2D-GE* images derives from the inhomogeneous background intensity, i.e. the fact that it is not uniform and increases non-linearly in protein spot regions. It is often caused either by flawed illumination during the scanning process or by local variations in gel density which become visible during the staining process.

Another crucial challenge comes from the wide range of protein concentration. Low- and high-abundance proteins are represented by faint and saturated spots, respectively. Faint spots are mainly caused due to labeling discrepancies. The contrast between the intensity of faint spots and the background is very poor. Saturated spots are caused by the incapability of the imaging technology device to capture color differences above a certain value (saturation) at which the light colors cannot be distinguished. As a result, saturated protein spots are characterized by a flat surface of uniform intensity with the maximum value around their centers (*see Figure 4.4(a) and (b)*).

One of the core challenges in *2D-GE* images comes from the complex spot regions containing overlapping spots. Due to the mixture complexity of the biological sample, protein migration is obstructed and multiple proteins called ‘multiplets’ tend to occupy the same locations on the gel surface. In some cases, incomplete protein denaturation may also be responsible for the presence of spot clusters. High-abundance protein spots are visible however, low-abundance protein spots are being covered and their peaks can hardly be distinguished. In addition, the boundaries of the overlap cannot be delineated by the human eye and the resolution in these regions is deteriorated (blurred regions) (*see Figure 4.4(b)*).

Moreover, protein tails called streaks tend to occupy a large portion of the surface. Streaks can be horizontal and/or vertical and are caused during migration where protein residues are produced in both dimensions. The density of each individual streak primarily depends on the corresponding protein concentration (*see Figure 4.4(c)*).

Several artifacts such as dust particles, cracks and *SDS* residues not related to protein components as well as the high level of speckle noise are also inherent flaws in *2D-GE* images (*see Figure 4.4(d)*).

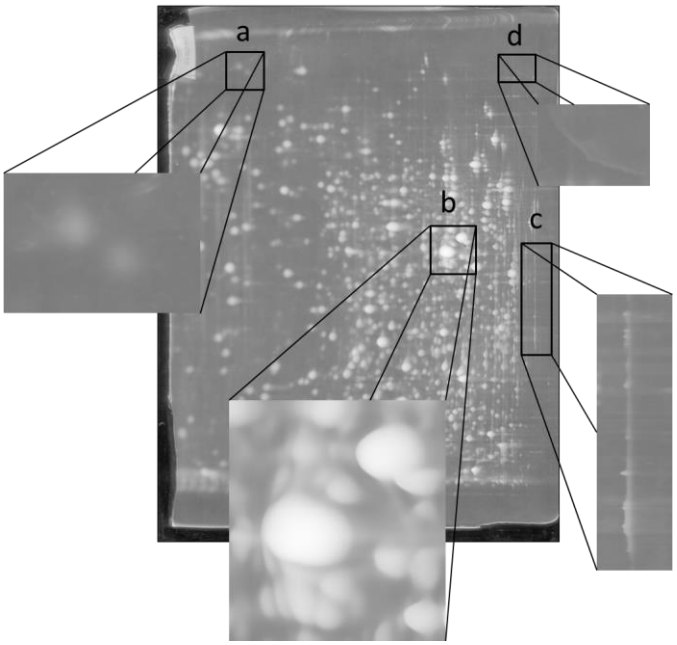

Figure 4.4: Challenges in *2D-GE* images: (a) faint spots, (b) saturated and overlapped spots, (c) streaks and (d) artifacts.

4.2.5 *2D-GE* Image Analysis

The *2D-GE* image analysis pipeline consists of six established processes: a) pre-processing, b) alignment (warping), c) detection, d) segmentation, e) quantification, f) matching and g) statistical analysis. Several image analysis systems utilize combinations of the aforementioned processes which are not interconnected necessarily in this order.

The state-of-the-art in *2D-GE* image pre-processing consists of noise removal by applying smoothing techniques. The latter are implemented by utilizing a Gaussian or a polynomial kernel however; there are more sophisticated smoothing techniques such as wavelets [103] and contourlets [70].

The pre-processed images are aligned (warped) by adjusting geometric distortions. Starting from a pixel at a specific position (landmark) in the reference image, all pixels at that identical position in all other images are compared. Landmarks do not need to be associated with spots. Warp vectors are generated so as to represent pixel correspondences between two gel images and positional corrections are performed. As a result, all images are fused into one final image which consists of all spots stemmed from all images and is considered to be the proteome map of the sample under investigation. The alignment of proteomics images cannot be considered challenging since satisfactory results are already obtained by commercial software packages.

Aiming at protein identification, the next step is protein spot detection. The scope in protein spot detection is to identify differentially expressed proteins such as proteins which are active during the different stages of a disease. Hence, it is of vital importance to detect protein spots which have appeared or disappeared between samples of healthy and diseased origin. In the process of detection, the centers of each individual spot are identified in order to determine the exact position, i.e. the unique coordinates (*pI*, *Mw*) of each individual spot on the gel surface. Spot centers correspond to mass spot centers. Protein spot detection is hindered by artifacts, streaks and multiplets, which have already been discussed in the previous section. Several features such as shape, size and intensity values usually vary between artifacts and protein spots. Nevertheless, there are cases where the above features are similar and the detection of true protein spots is often unsuccessful. Moreover, streaks consist of proteins as well as protein residues which correspond to migrated proteins. The detection of proteins and non-protein residues in streaks is a complicated, non-trivial task. In addition, multiplets are really challenging since spot centers of smaller proteins are overlapped by spot centers of larger ones. Thus, overlapping spots are hardly

distinguished. This thesis presents an unsupervised protein spot detection technique which is based on the principles of mathematical morphology in order to locate regional intensity maxima associated with protein spots (*see Chapter 6, § 6.2*).

Protein spot segmentation is the process of separating spots from the background and other non-protein components. Each segment ideally represents the spot of a single isolated protein and reflects the amount of protein expression. The accurate delineation of protein spot boundaries is the key requirement for successful spot matching in order to detect alterations in protein expression and identify proteins which may be further utilized as biomarkers. In this thesis, a protein spot segmentation scheme is presented, which is based on the principles of region-based *AC* models. The latter are prior candidates for spot segmentation since they are topologically adaptable, i.e. they are capable of splitting on the boundaries of multiplets and merging on the boundaries of single spots. Moreover, they are insensitive to the inhomogeneous background and the presence of noise (*see Chapter 6, § 6.3*).

The segments created in the previous procedure are exploited for protein spot quantification. In this process, the amount of each individual protein spot is estimated by calculating the cumulative intensity of the associated spot area, i.e. the spot volume embedded in a spot boundary. In this thesis, an established volume metric for spot quantification is utilized.

After quantification, spot matching is performed. In this process, pixels associated with the center coordinates of individual spots representing the same protein in all aligned images, are matched. As opposed to alignment, spot detection should be performed prior to matching. Typically, it is more accurate to match spots emerged from the same biological sample than spots emerged from different biological samples. Similar to alignment, spot matching is performed satisfactorily by commercial software packages according to *2D-GE* image analysis experts.

Finally, in statistical analysis the quantified segments in all aligned images are compared in order to investigate both significant differences and similarities in protein expression profiles in response to different treatments or disease states. Several spot parameters may be used such as spot area and spot volume. The most popular statistical tools utilized are ANalysis Of VAriance (*ANOVA*) and Student's t-Test. Any significant differences and similarities observed are referenced back to the corresponding proteins. Protein identification is achieved by using mass spectrometric analysis which determines peptide molecular weights. Protein characterization is performed by searching protein databases such as the HUman Proteome Organization (*HUPO*) [104] and correlating proteins with the resulted molecular weights. Protein identification and characterization are beyond the scope of this thesis since the former requires signal analysis algorithms and the latter database algorithms.

4.2.6 State-of-the-Art

2D-GE Image Analysis Models Proposed in Literature

Numerous models have been suggested to tackle with *2D-GE* image analysis such as stepwise thresholding [105], edge detection [106] and Watersheds Transform (*WST)* [107]. Stepwise thresholding applies an increasing threshold on the *2D-GE* image of interest, starting from the lowest intensity level which can be associated with a protein spot. As the applied threshold increases, each connected image area may be split into multiple connected sub-areas. This process is iterative and stops when no more splits are possible. The segmentation result is determined by the connected sub-areas remaining in the last split.

Edge detection methods aim to identify discontinuities in image intensity often associated with protein spot boundaries. Both stepwise thresholding and edge detection methods are highly sensitive to noise, artifacts, non-uniform background and overlapping spot clustering [108], whereas manual editing may be required in the case of edge detection [109].

WST methods model a *2D-GE* image as a landscape where rain falls downhill formulating pools around each local intensity extremum. Areas collecting the water can be associated with protein spots. Although this approach copes with the presence of noise, artifacts and non-uniform background, it calls for additional post-processing since all pixels in the image are assigned to a catchment basin, resulting in over-segmentation [110]. Aiming to cope with this issue, Kim et al. [111] introduced a hybrid *2D-GE* image segmentation approach based on *WST* and stepwise thresholding. However, the background removal process incorporated in this hybrid approach cannot cope with the presence of faint spots. Similar variations have been introduced for the segmentation of cell images.

2D-GE Image Analysis Software Packages

2D-GE image analysis is usually performed by visual inspection of an expert gel analyst with the aid of a software package. The scope of the software package is to meliorate visualization as well as data analysis in order to identify significant variations in protein expression profiles. Numerous software packages are nowadays adapted to biological laboratories around the world. A list of them is cited in Table 4.1.

Table 4.1: List of available *2D-GE* image analysis software packages

Name	Company	Country	Website
Melanie (under ImageMaster 2D Platinum platform)	Geneva Bioinformatics (GeneBio) SA	Switzerland	www.genebio.com
PDQuest	Bio-Rad Laboratories	USA	www.bio-rad.com
Delta2D	Decodon	Germany	www.decodon.com
Progenesis SameSpots (superseded Phoretix 2D)	Nonlinear Dynamics	UK	www.nonlinear.com
Gellab II	Scanalytics	USA	www.scanalytics.com
Impressionist	Genedata	Switzerland	www.genedata.com

Kepler	Large Scale Biology	USA	www.lsbc.com
ProteinMine	Scimagix	USA	www.scimagix.com
Z3	Compugen	Israel	www.cgen.com
Dymension	Syngene	UK	www.syngene.com

2D-GE image analysis software packages utilize methods which are hidden from the user. To this end, the development of a golden reference *2D-GE* image analysis pipeline is impeded. Moreover, such software packages require human intervention for empirical parameter selection based on heuristic considerations. This yields to a notable output variance where results lack objectivity and reproducibility as well as the necessity of technical support to calibrate the software. Furthermore, the results obtained by each software package require manual editing by gel expert analysts so as to eliminate spots that have been falsely detected, reconsider spots that have not been detected or correct boundaries which define the spot area. The latter occurs since most software packages assume that spot intensity values distribution is sufficiently described by a Gaussian distribution, which is not the case.

For instance, Melanie [112] requires empirical adjustment of three detection parameters namely smooth, saliency and min area (*see Chapter 6, § 6.2.3*). In addition, the supported input and output image formats are not typical and can only be processed with Melanie. PDQuest [113] requires empirical calibration based on intensity values of faint, saturated and overlapping spots of each gel image imported whereas Delta2D requires inner markers which operate as landmarks for spot identification.

Most *2D-GE* image analysis software packages are capable of performing sufficient image alignment and spot matching however, they fail during spot detection and segmentation. Hence, development of improved spot detection and segmentation methods is of dire need and this is the motivation for part of the work of this thesis.

4.3 Medical Images

Medical imaging is capable of aiding clinical practice by means of imaging acquisition techniques applied on the human body. Medical imaging modalities provide vital measures of internal anatomical structures and are investigated by *MDs* for the detection and diagnosis of various diseases in order to select and guide the most appropriate treatment. Since the geometry of anatomical structures is of great importance, automated and reliable image segmentation methods are in demand.

4.3.1 Mammograms

The female breast is a sweat gland which produces and secretes milk during lactation [114]. Each breast is divided into 15 to 20 sections, called lobes, separated from each other by fatty tissue and each lobe is divided into smaller lobules which end in dozens of tiny bulbs that secrete milk in response to hormonal signals. The lobules and bulbs are linked by thin tubes called ducts. Each duct contains a number of glandular cells clustering around it and opens on the tip of the nipple. The latter is a dark-pigmented area accommodating the ducts and their openings to allow milk to flow out once it is sucked. Figure 4.5 depicts the anatomy of the female breast gland. The most common types of breast cancer are the ductal and lobular carcinomas which arise in the cells of ducts and lobules, respectively.

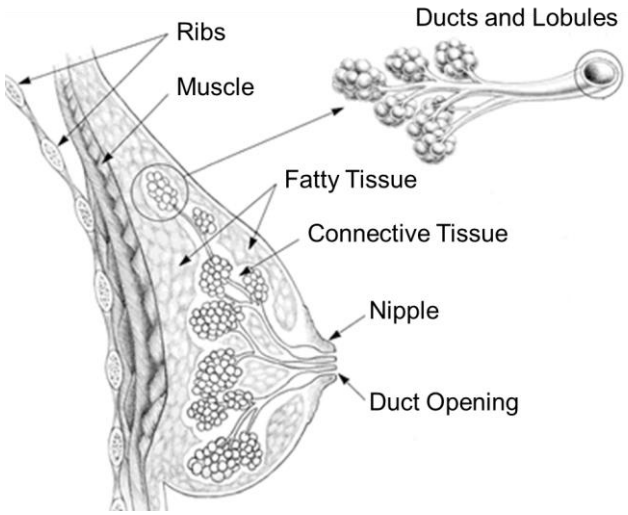

Figure 4.5: Anatomy of the female breast gland.

Breast abnormalities occur mainly in the glandular tissue and can be divided into benign and malignant. They are characterized in four classes: (a) microcalcifications, (b) well-defined/circumscribed masses, (c) speculated masses and (d) ill-defined masses, which are depicted in Figure 4.6.

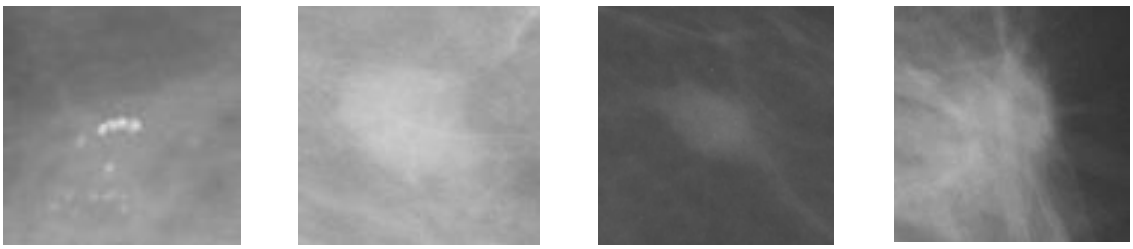

(a) (b) (c) (d)

Figure 4.6: Samples of breast abnormalities characterized as: (a) microcalcifications, (b) well-defined/circumscribed masses, (c) speculated masses and (d) ill-defined masses.

Breast abnormalities are categorized in five types of breast cancer [115]:

a) Stage 0: the size of tumor is less than 2cm in diameter and is only present where it was first detected, i.e. it has not spread to other parts of the body.

b) Stage I: the size of the tumor is less than 2cm in diameter and has spread beyond margins into the surrounding tissue.

c) Stage II: the size of the tumor is between 2 and 5cm in diameter and has spread beyond margins to other parts of the body.

d) Stage III: the size of the tumor is greater than 5cm in diameter and has spread beyond margins to other parts of the body.

e) Stage IV: the stage of the tumor is any size, has attached to the chest wall and has spread to the lymph nodes.

Mammography is an X-ray screening imaging modality and its key role is to detect breast abnormalities [116]. An X-ray beam emits radiation through the breast and is absorbed selectively by different tissue types. On the other side of the breast the radiation is recorded onto a film or plate. Since different tissues in the breast absorb different amounts of radiation, it is possible to distinguish features and details about the tissues being examined. The fatty tissue in the

breast has a low density, allowing the X-rays to pass through easily to expose the film. Hence, fatty areas of the mammogram are dark. The glandular tissue in the breast has a higher density, resulting in brighter areas. The muscle is a characteristic feature of the mammogram and presents itself as a bright triangle in one corner of the image. During a screening for breast cancer, radiologists inspect the mammogram for areas that may indicate further investigation through biopsy. Figure 4.7 illustrates a typical mammogram obtained by the Mammographic Image Analysis Society (mini-*MIAS*) database [117].

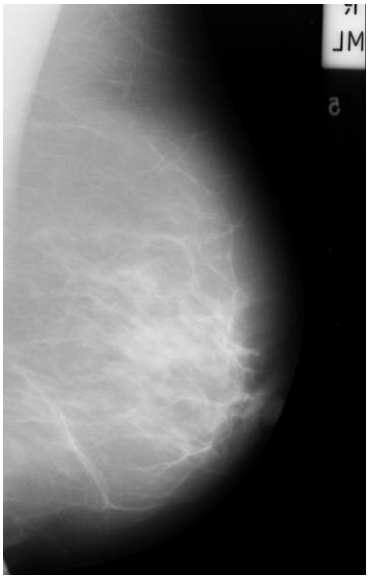

Figure 4.7: Typical mammogram obtained by the mini-*MIAS* database [117].

4.3.2 Ultrasounds of Thyroid Gland

The thyroid gland is a butterfly-shaped endocrine gland located in front of the trachea (windpipe) and below the thyroid cartilage (Adam's apple) [118]. It consists of two lobes one on each side of the windpipe connected by a tissue called the isthmus. Figure 4.8 depicts the anatomy of the thyroid gland.

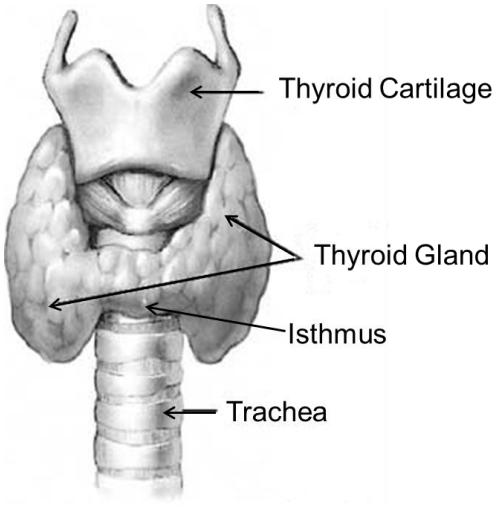

Figure 4.8: Anatomy of the thyroid gland.

The thyroid gland plays a key role in regulating the body's metabolism and calcium balance. It comprises two types of cells namely follicular and parafollicular. The former secrete two iodine hormones called thyroxine (*T4*) and triiodothyronine (*T3*), whereas the latter secrete the hormone calcitonin. These hormones are secreted into blood and travel across every tissue in the body in order to stimulate it to produce proteins and increase the amount of oxygen. The conditions under which the thyroid gland does not produce enough hormones or produces too many hormones are called hypothyroidism or hyperthyroidism, respectively. In either case, several body systems may be affected resulting in alterations in weight, heartbeat, body temperature, digestion and muscle function [119].

Thyroid nodules are abnormal growths of thyroid cells which form lumps/bumps or irregularities within the thyroid gland. They are caused either by constant exposure to radiation or by heredity. The vast majority of thyroid nodules are benign however, a small proportion is malignant and surgery is required in order to remove them. In terms of early diagnosis, thyroid nodules need some type of evaluation and are categorized in four types of thyroid cancer [120]:

a) Papillary carcinoma: they account for 80% of diagnosed cases. They grow slowly only in one lobe of the thyroid gland but spread to the lymph nodes in the neck. They can be successfully treated and are rarely fatal.

b) Follicular carcinoma: they account for 15% of diagnosed cases. They are more aggressive as they can spread to lungs and bones and they are common in countries where people do not have enough iodine in their diet. Cure rates are also high.

c) Medullary carcinoma: they account for 5% of thyroid tumors and can spread to lymph nodes, lungs or liver even before a nodule is discovered. Cure rates are low compared to the aforementioned types.

d) Anaplastic carcinoma: they account for 2% of thyroid tumors and can spread into the neck and other parts of the body. They derive from papillary or follicular carcinomas and are hardly treated.

Ultrasound imaging (*US*) is a non-invasive, low-cost diagnostic imaging technique widely utilized for the detection of thyroid nodules compared to other non-invasive modalities such as Magnetic Resonance Imaging (*MRI*) and Computed Tomography (*CT*), which are more expensive and less available [121]. It poses no risks to the patient since it does not use ionizing radiation (as in X-rays devices) which causes cancer development. An electric field is applied to a transducer which consists of piezoelectric crystals. As a result, the latter emit high-frequency sound waves greater than the upper limit of human hearing (1-10 MHz). Sound waves penetrate the human body by means of the ultrasound gel and propagate with the aid of pressure variations. The latter obtain high and low values in areas of compression (high-pressure areas) and in areas of rarefaction (low-pressure areas), respectively. The penetration of the ultrasound wave is proportional to the wavelength of the sine wave and the propagation velocity is relatively constant at 1540 m/sec. The transducer records the electrical current generated by the echoes produced as the sound waves bounce back from thyroid nodules. These echoes form the basis of all ultrasound imaging and the amount reflected highly depends on the density of the tissue. A computer receives the electrical current and produces images in real-time consisting of vital information with regards to the size, structure and pathology of the nodule.

Thyroid nodules are classified by means of ultrasound imaging with regards to the degree of malignancy into four basic types [122] and are depicted in Figure 4.9:

a) Grade 1: small round and anechoic areas suggestive of thyroid cysts.

b) Grade 2: i) isoechoic or hyperechoic solid nodules with or without cystic change and coarse calcifications suggestive of adenomatous goiter.

ii) isoechoic solid nodules or complex nodules with normal appearance of the thyroid gland suggestive of follicular adenoma.

c) Grade 3: i) hypoechoic solid nodules with regular border suggestive of follicular neoplasms.

ii) cystic nodules with solid component suggestive of papillary carcinomas.

d) Grade 4: hypoechoic solid nodules with an irregular border and with the presence of calcifications suspicious for malignancy and highly suggestive of thyroid carcinoma.

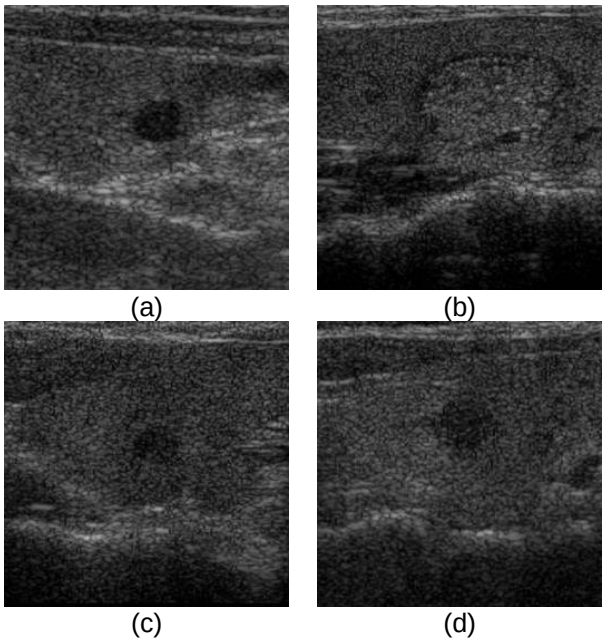

Figure 4.9: Samples of thyroid nodules classified in: (a) Grade 1, (b) Grade 2, (c) Grade 3 and (d) Grade 4.

4.3.3 Endoscopy Images

The colon is an important organ since it forms the last part of the digestive tract where food is digested. Food travels down the esophagus to the stomach and from there to the large intestine. The latter contains the colon which absorbs

water and nutrients from food and takes part in the synthesis of certain vitamins. The colon consists of five sections: the cecum, the ascending colon, the transverse colon, the descending colon and the sigmoid colon as depicted in Figure 4.10 [123].

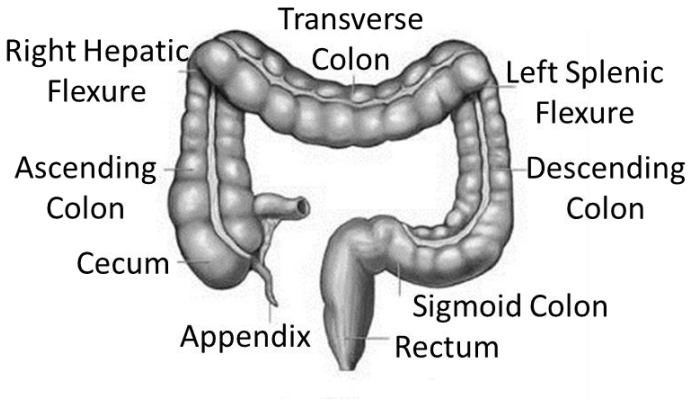

Figure 4.10: Anatomy of the colon.

Colon polyps are growths that range from a few millimeters to several centimeters. They are generated when the genetic material within cells changes and mutates. There are two common types of polyps: a) hyperplastic polyps and b) adenomas. The former are not at risk for cancer. Nevertheless, the adenomas are considered to be the precursors for almost all colon cancers. Even though it is impossible to tell which adenomatous polyps will become cancers, larger polyps are more likely to become cancers [124].

Endoscopy is a minimally invasive diagnostic technique which allows the *MD* to examine the human body without performing surgery by means of the endoscope [125]. The latter is a long, thin, flexible tube with a lens at one end and a video camera at the other. The endoscope may also be used for enabling biopsies and retrieving foreign objects. The end with the lens is inserted into the patient. Light passes down the tube (via bundles of optical fibers) to illuminate the relevant area, and the video camera magnifies the area and projects it onto a screen so that the doctor can see what is located. Typically, an endoscope is inserted through one of the body's natural openings, such as the mouth, urethra, or anus. Figure 4.11 illustrates samples of polyps on endoscopy images.

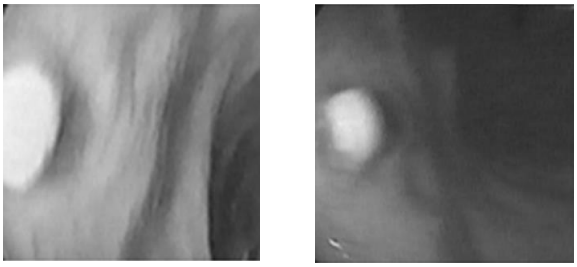

(a) (b)

Figure 4.11: Samples of colon polyps on endoscopy images.

4.3.4 Dermoscopy Images

The skin is the largest organ of the human body. Its thickness ranges from 0.5mm on eyelids to 4mm on the palms of hands and soles of feet. Its key role is to protect the body and keep the integrity of internal systems intact. It is also responsible for vital functions such as insulation, temperature regulation, sensation as well as the production of vitamin D.

The skin comprises three layers: a) the epidermis (outer layer), b) the dermis (middle layer) and c) the hypodermis (bottom layer). The epidermis consists of keratinocytes, melanocytes and Langerhans cells. Keratinocytes are the barriers against environmental pathogens, melanocytes are responsible for skin pigmentation as a defense against sun rays and Langerhans cells are part of the immune system. The dermis is divided into the papillary dermis and the reticular dermis and consists of collagen and elastin fibers which are responsible for repairing the skin. The hypodermis is mainly composed of fatty tissue and its primary role is to manage the functions of feeding, excreting and heat exchange. Sweat glands which emerge from this layer are able to control body's temperature by evaporating and cooling the skin surface [126]. The anatomy of the skin is portrayed in Figure 4.12.

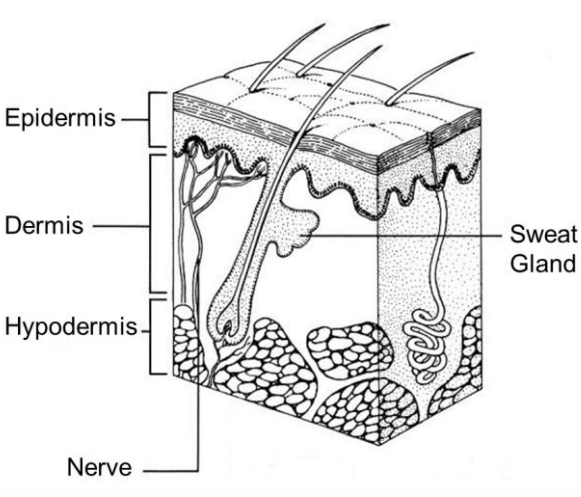

Figure 4.12: Anatomy of the skin.

Skin cancer is divided into two main categories: non-melanocytic and melanocytic skin lesions which are further characterized as benign or malignant [127]:

a) Benign non-melanocytic lesions are defined as seborrhoeic keratosis and dermatofibroma. The former is a benign tumor composed of epidermal keratinocytes, whereas the latter is a common fibrous lesion occurring on the legs and arms.

b) Benign melanocytic lesions are defined as melanocytic and atypical nevi. The former are lesions which result from the proliferation of melanocytes at the dermo-epidermal junction, whereas the latter have irregular and indistinct borders.

c) Malignant non-melanocytic lesions are Basal Cell Carcinoma (*BCC*) and Squamous Cell Carcinoma (*SCC*). The former is the most common type of skin cancer and arises in the basal keratinocytes in the deepest layer of the epidermis. Even though it rarely metastasizes, it is still considered malignant since it causes destruction and disfigurement. The latter starts when the atypical keratinocytes grow through the basement membrane and invade the dermis.

d) Malignant melanocytic lesions are called melanomas and are the most serious form of skin cancer. They are characterized by the uncontrolled growth of melanocytes. A melanoma might appear on the epidermis and dermis suddenly without warning and if the body itself is unable to fight it, it spreads to lymph nodes and internal organs. There is today no effective

treatment against advanced melanoma and the only way to treat it is to physically remove it in its early stage.

The clinical ABCD rule for diagnosing skin lesions is widely used [128]. This rule states that the skin lesion is likely to be a melanoma if the following criteria are fulfilled: Asymmetry, Border irregularity, Color variation and Diameter of more than 6 mm. Figure 4.13 illustrates samples of benign/malignant non-melanocytic and melanocytic skin lesions obtained by the Atlas of Dermoscopy [129].

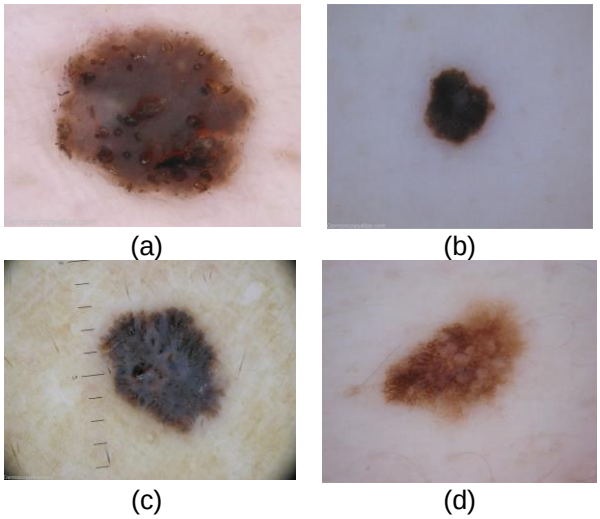

Figure 4.13: Samples of skin lesions obtained by [129] characterized as: (a) benign non-melanocytic, (b) benign melanocytic, (c) malignant non-melanocytic and (d) malignant melanocytic.

Dermoscopy is an in vivo non-invasive skin imaging technique which is utilized for the diagnosis of melanoma and pigmented skin lesions [130]. It allows the magnification of structures of the epidermis, dermo-epidermal junction and papillary dermis in order to be investigated for irregularities and possible malignancy. A dermoscope (or dermatoscope), is a combination of a magnifying glass (lens) and polarized light. The lens is encircled by light sources and is put in direct contact with the skin. Fluid (usually water or oil) is used to refract the light. Without the polarized light and the fluid, light is reflected at the surface of the skin, and only the patterns visible there can be examined by the physician. When the light is refracted by the polarized light and the fluid, it is the reflections from the

subsurface that reach the dermatologist's eye. In this way, the physician is able to extract more information from a simple non-invasive examination.

4.3.5 *CT* Scans of Lung Parenchyma

The lungs are located in the thoracic cavity and between them lies the heart. The lungs are supplied by three major tubular systems: the airways or bronchi responsible for air transport, the pulmonary arteries responsible for transporting deoxygenated blood from the (right) heart into the lungs and the pulmonary veins, responsible for returning the oxygen-rich blood to the (left) heart to be redistributed into systemic circulation. More peripherally, where diameters are down to two millimeters or less, the airways are named bronchioles. The alveoli are the primary site of gas exchange. Supplied with air by the terminal bronchioles, the alveoli represent the leaves in the bronchial hierarchy. The collection of alveoli is called the lung parenchyma [131]. Figure 4.14 portrays the anatomy of the lungs.

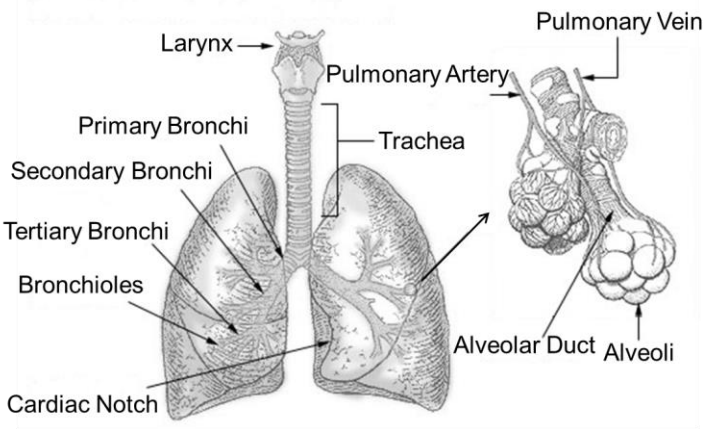

Figure 4.14: Anatomy of the lungs.

Lung diseases are divided into three categories [132]:

a) Parenchymal diseases, which include pulmonary emphysema, pneumonia, pulmonary fibrosis, asthma, acute bronchitis and sarcoidosis. Emphysema and chronic bronchitis are called Chronic Obstructive Pulmonary Disease (*COPD*), which is listed as the fourth cause of death in the world. It causes

a loss of elasticity of the lung parenchyma and a deterioration of the structures that support the alveoli.

b) Primary lung cancer, which stems from lung cells and is strongly smoking related. There are two main types of lung cancer: Non-Small-Cell Lung Carcinoma (*NSCLC*) and Small-Cell Lung Carcinoma (*SCLC*). For the former, the choice of therapy highly hinges on the tumor stage. For the latter, chemotherapy is the only option even if it has been detected in an early stage.

c) Lung metastases, which are caused by tumor cells within the blood stream metastasizing in breast, kidney, head, neck and colon. The standard treatment of lung metastasis is chemotherapy.

Computed Tomography (*CT*) lung screening is a non-invasive, painless imaging technique which uses X-rays [133]. It allows the radiologist to examine different levels and slices of the lungs using a rotating X-ray beam. *CT* imaging is capable of visualizing the effects of parenchymal diseases as well as lung cancer. Figure 4.15 illustrates: a) the axial and b) coronal view of a *CT* lung image produced by a multi-detector *CT* scanner obtained by the Lung Image Dataset Consortium Image Collection (*LIDC-IDRI*) [134].

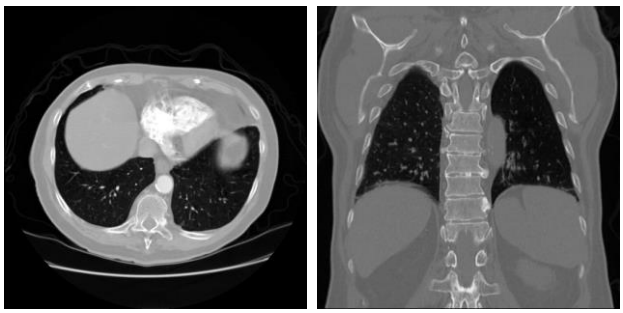

(a) (b)

Figure 4.15: Two views of a *CT* lung image: (a) axial and (b) coronal obtained by [134].

4.3.6 Labial Teeth and Gingiva Photographic Images

The gingiva is the component of oral masticatory mucosa which covers the alveolar process and surrounds the cervical areas of the teeth. It consists of three structures: a) the epithelium, b) the lamina propria and c) the mucoperisoteum.

The gingiva obtains its final shape and texture in conjunction with eruption of the teeth. The gingiva is divided into two categories: the Free Gingiva (*FG*) and the Attached Gingiva (*AG*). *FG* is bordered by the free gingival margin, the gingival groove and the sulcular epithelium, whereas *AG* lies between *FG* and the mucogingival junction. The area which lies within *AG* is called interdental groove [135]. Figure 4.16 portrays the anatomy of the gingiva.

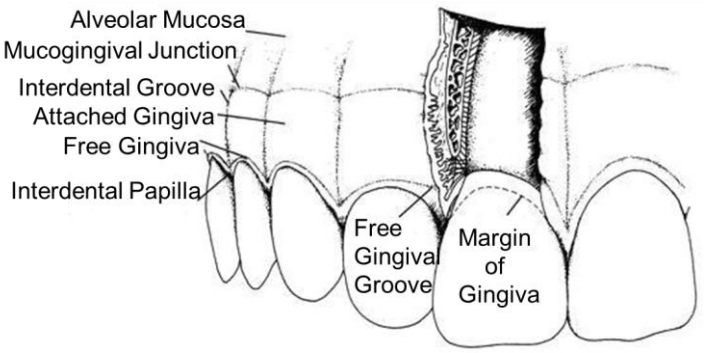

Figure 4.16: Anatomy of the gingiva.

Gingivitis is an inflammatory periodontal disease caused by bacterial plaque. The latter accumulates in the small gaps between teeth and releases toxins which yield to the destruction of supporting structures for the tooth such as gums, periodontal ligament and alveolar bone. Gingivitis is a reversible disease but may progress to periodontitis in the absence of treatment. Therapy is aimed primarily at plaque control and reduction or elimination of gingival inflammation in order to allow gum tissues to heal, followed by appropriate patient hygiene instruction, dentist monitoring and teeth cleanings to prevent re-initiation of inflammation [136].

The labial teeth and gingiva photographic images (*LTG*) utilized in this thesis have been conceived by using a combination of a Canon EOS 7D digital single-lens reflex color camera with a Canon EFS 18-135mm standard zoom lens. A circular polarization filter was used in front of the lens and a linear polarization filter in front of the internal camera flash. The transmission axis of the polarization filters were set to be perpendicular in order to minimize specular reflection in the images. A tripod with camera and another tripod were used to keep the head

constant as well as a standard mouth opener for dentistry to avoid occlusion by cheeks and lips. Figure 4.17 illustrates samples of *LTG* images obtained by [137].

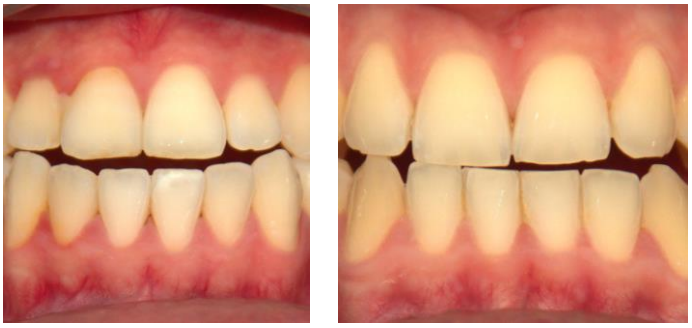

(a) (b)

Figure 4.17: Samples of *LTG* images obtained by [137].

4.4 Summary

In this chapter, a concise overview of proteomics and medical images, which were used in our segmentation experiments, is presented. The latter include several imaging modalities such as: a) mammograms, b) ultrasounds of thyroid gland, c) endoscopy images, d) dermoscopy images, e) *CT* scans of lung parenchyma as well as f) labial teeth and gingiva photographic images. A biological and medical background on either case is provided along with the imaging technologies which produce these images.

CHAPTER 5

5. MEDICAL IMAGE SEGMENTATION UTILIZING THE AUTOMATIC FRAMEWORK

5.1 Introduction

Active Contours (*ACs)* are prominent in medical image segmentation, due to their inherent noise-filtering mechanism and their topological adaptability [138]-[140]. Typically, they are parameterized empirically by *MDs*, who are unfamiliar with the intrinsic mechanisms of the underlying algorithms. Consequently, they depend on technical support by engineers. A key challenge is to develop reliable unsupervised parameterization *AC* approaches in order to set *MDs* free from the tedious and time-consuming process of parameter tuning, as well as to bolster the objectivity and reliability of the segmentation results.

Region-based *ACs* have been proposed in medical image analysis literature as suitable for several medical imaging modalities since they cope well with regions of weak edges, such as human tissues [141]-[144]. Like most *AC* models, they rely on parameters weighting the regularization and data fidelity energy terms. Regularization and data fidelity parameters are of critical importance in region-based *AC* segmentation, since they act as amplifiers on the forces guiding contour evolution. Despite this importance, in most existing methods, both regularization and data fidelity terms are manually set and kept intact over the image. As a result, segmentation results are suboptimal and subjective.

In this chapter, the presented framework described in detail in Chapter 3, is applied on various medical imaging modalities. The latter are provided by various acquisition devices whose settings are often altered in clinical practice. Such alterations naturally affect the acquired image features. As a result, in the case of empirical parameterization, manual fine-tuning might be required on a per-image basis, raising doubts on the actual value of a computational segmentation approach. Our application demonstrates that the presented framework is not

sensitive on the shape/size of the target region and on alterations in the settings of the acquisition devices.

5.2 Experimental Evaluation on Medical Images

The presented framework is embedded into the Chan-Vese model [2] by replacing the empirically fine-tuned parameters with the automatically adjusted ones (*see Eq. (3.3.1)*), in order to evaluate the segmentation performance of the automated versus the empirically fine-tuned version. Experiments are conducted on databases of various medical imaging modalities so as to confirm the framework's generality with respect to image content. All images used were investigated by *MDs* who provided ground truth images. The shape of all abnormalities as well as the irregularity of their margins are malignancy risk factors which are highly considered by *MDs* before proceeding to fine needle aspiration biopsy. It should be noted that, contour initialization was the same for both the presented framework and the empirically fine-tuned version in order to facilitate fair comparisons.

5.2.1 Segmentation of Abnormalities on Mammograms

The first database consists of 50 mammographic images containing abnormalities randomly obtained by the mini-*MIAS* database [117]. The background tissue is characterized as: a) fatty, b) fatty-glandular and c) dense-glandular, whereas the abnormality is classified as: a) well-defined/circumscribed and b) ill-defined. In terms of its severity, the abnormality is defined as benign or malignant. Figure 5.1 illustrates segmentation results obtained by the automated version on mammographic images containing abnormalities, as well as by the empirically fine-tuned version. It is evident that the automated version delineates the boundaries of abnormalities in greater detail and the contour is less jagged than the one generated by the empirically fine-tuned version.

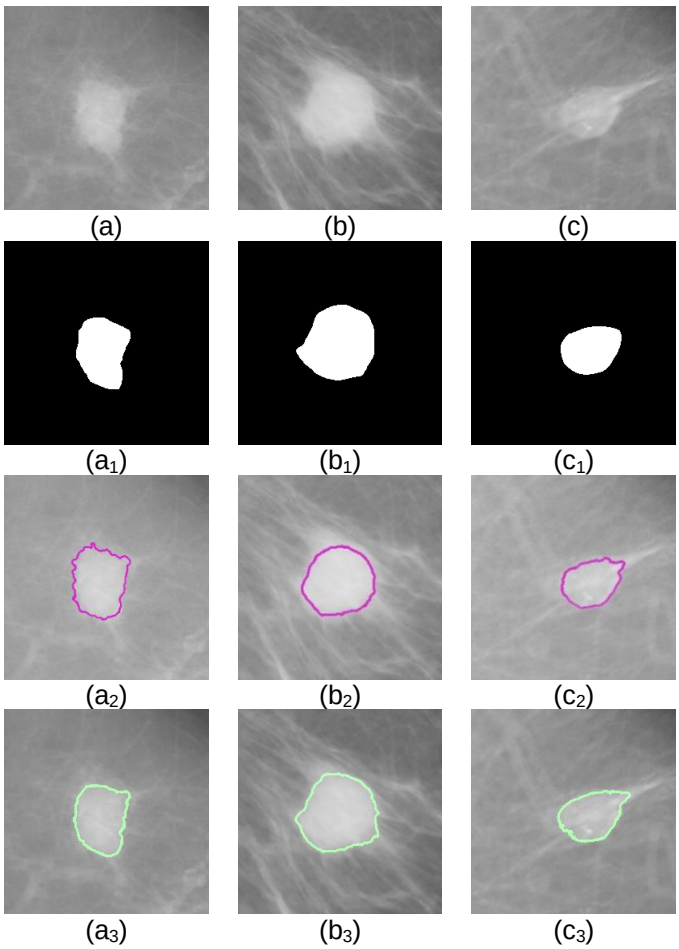

Figure 5.1: (a)-(c) Mammographic images containing abnormalities, (a_1)-(c_1) ground truth images, (a_2)-(c_2) segmentation results of the empirically fine-tuned version, (a_3)-(c_3) segmentation results of the automated version.

5.2.2 Segmentation of Thyroid Nodules on Ultrasound Images

The second database consists of 45 thyroid ultrasound images containing hypoechoic nodules provided by the Radiology Department of Euromedica S.A., Greece. All ultrasound images were acquired using a digital ultrasound imaging system HDI 3000 ATL with a 5-12 MHz linear transducer. Instrument settings were fixed accordingly to the built-in 'SmallPartTest' Philips protocol, magnification was set to 1:1 and dynamic range was set to 150 dB/C4. Hypoechoic nodules with regular boundaries may represent follicular neoplasms of medium-risk, whereas hypoechoic nodules with irregular boundaries are considered suspicious for malignancy and may represent thyroid carcinomas. Figure 5.2 illustrates segmentation results obtained by the automated version on ultrasound images containing thyroid nodules, as well as by the empirically fine-tuned version. It is clear that the automated version embeds more pixels

corresponding to a nodule according to the ground truth inside the contour than the empirically fine-tuned version.

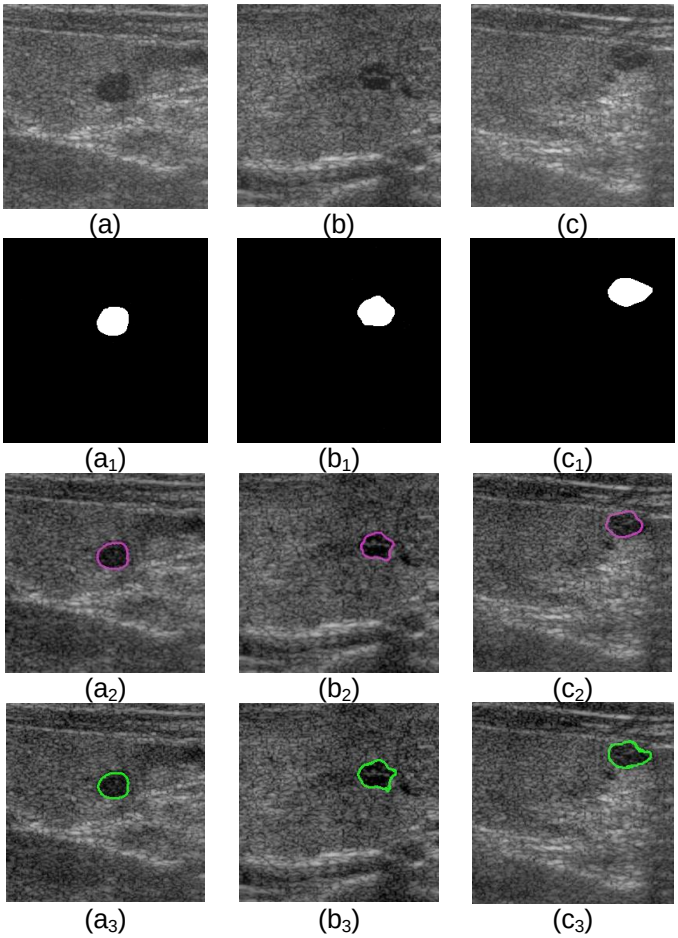

Figure 5.2: (a)-(c) Thyroid ultrasound images containing nodules, (a_1)-(c_1) ground truth images, (a_2)-(c_2) segmentation results of the empirically fine-tuned version, (a_3)-(c_3) segmentation results of the automated version.

5.2.3 Segmentation of Polyps on Endoscopy Images

The third database consists of 32 endoscopy frame images containing polyps provided by the Gastroenterology Section, Department of Pathophysiology, Medical School of the University of Athens, Greece and partially by the Section for Minimal Invasive Surgery, University of Tübingen, Germany. The endoscopic data was acquired from sixty-six different patients with an Olympus CF-100 HL endoscope. All frame images consist of small size adenomatous polyps which are not easily detectable and are more likely to become malignant. Figure 5.3 illustrates segmentation results obtained by the automated version on endoscopy

images containing polyps, as well as by the empirically fine-tuned version. It should be noted that the automated version achieves comparable segmentation results to the ones obtained by the empirically fine-tuned version yet in an unsupervised fashion.

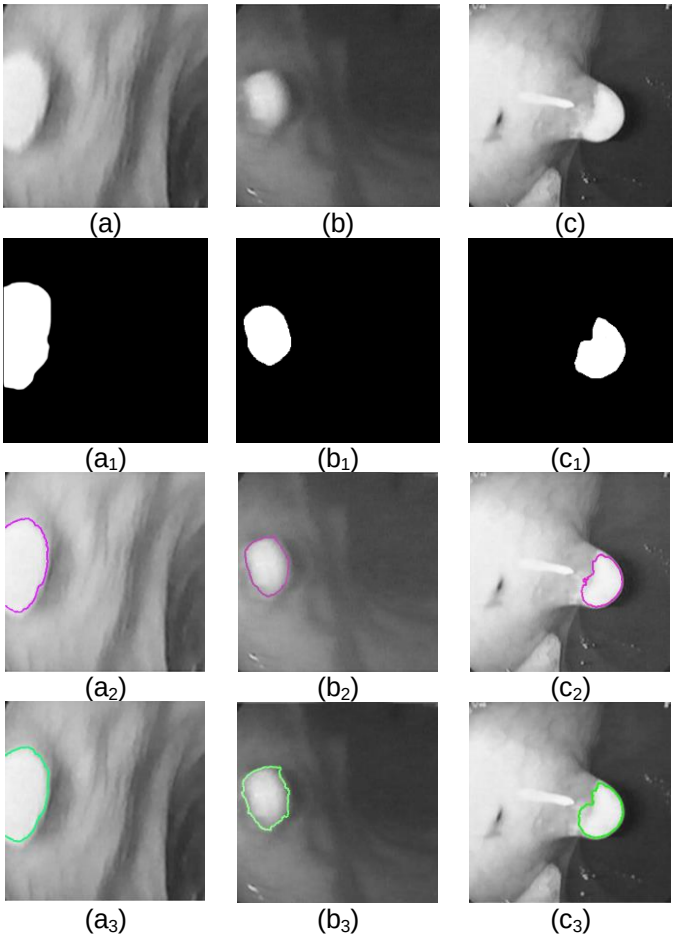

Figure 5.3: (a)-(c) Endoscopy images containing polyps, (a_1)-(c_1) ground truth images, (a_2)-(c_2) segmentation results of the empirically fine-tuned version, (a_3)-(c_3) segmentation results of the automated version.

5.2.4 Segmentation of Skin Lesions on Dermoscopy Images

The fifth database consists of 50 dermoscopy images containing skin lesions randomly obtained by the Dermoscopy Atlas [129], which is provided by the Skin Cancer College of Australia and New Zealand. The more asymmetrical the distribution of the pigmented lesion is, the more it is considered as an evolving growing nevus or a melanoma. Figure 5.4 illustrates segmentation results obtained by the automated version on dermoscopy images containing skin lesions, as well as by the empirically fine-tuned version. Apparently, the

automated version generates more detailed outlines of the lesions, whereas the empirically fine-tuned version includes pixels associated with background inside the contour.

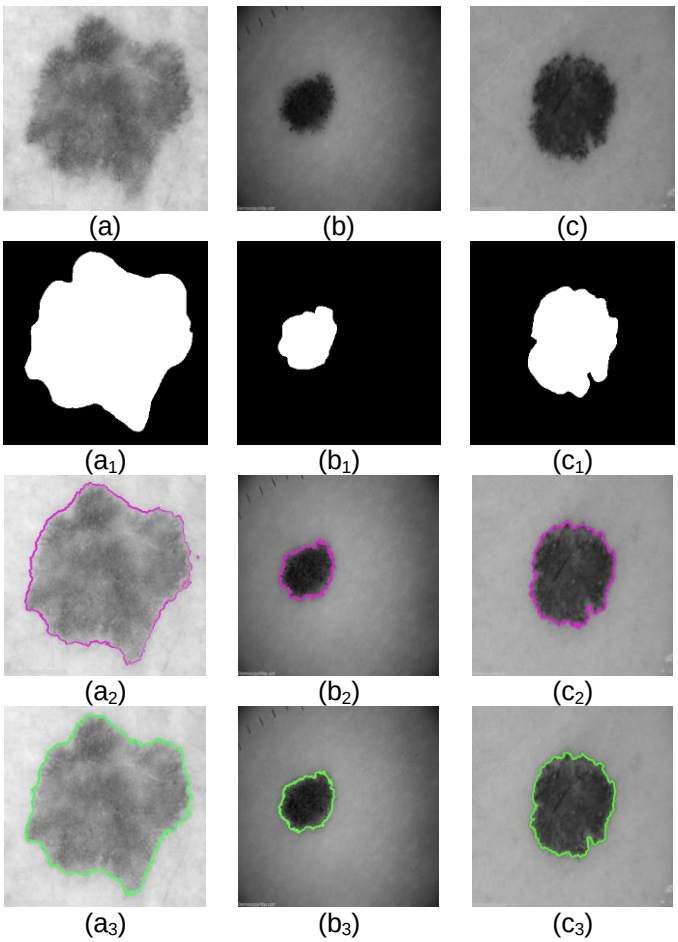

Figure 5.4: (a)-(c) Dermoscopy images containing skin lesions, (a_1)-(c_1) ground truth images, (a_2)-(c_2) segmentation results of the empirically fine-tuned version, (a_3)-(c_3) segmentation results of the automated version.

5.2.5 Segmentation of Lung Parenchyma on *CT* scans

The sixth dataset consists of 30 axial and 26 coronal *CT* scans of lung parenchyma obtained by *LIDC-IDRI* [134]. The aim of segmentation is to separate the lung parenchyma from the surrounding anatomy, which is typically impeded by airways or other "airway-like" structures in the right and left lung. The segmentation result is used for the computation of emphysema measures. Figure 5.5 and Figure 5.6 illustrates segmentation results obtained by the automated version on axial and coronal *CT* scans of lung parenchyma, respectively as well

as by the empirically fine-tuned version. It is notable that both versions achieve comparable segmentation results.

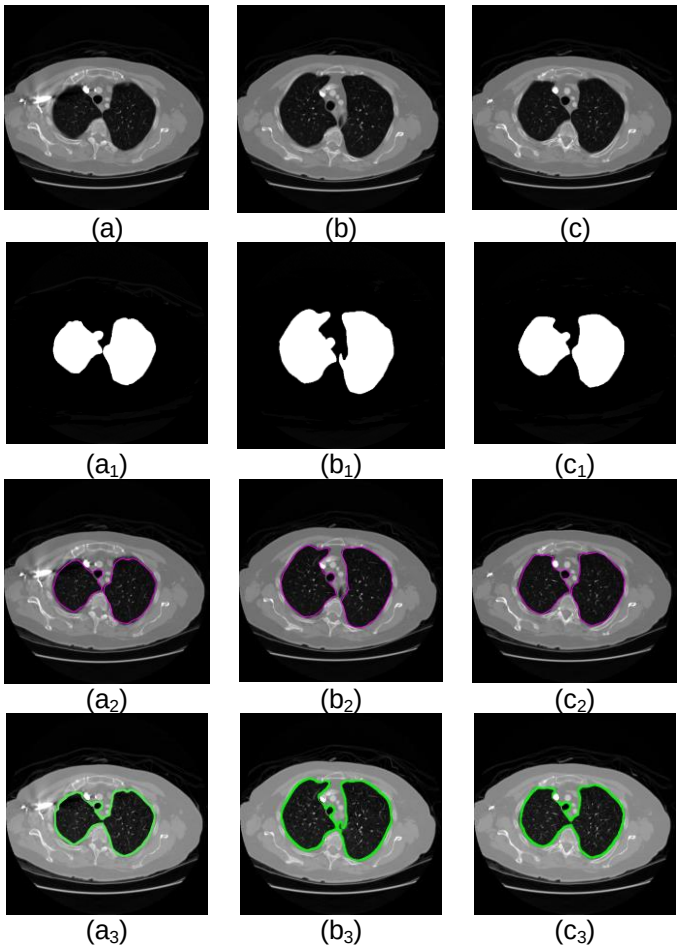

Figure 5.5: (a)-(c) Axial *CT* scans of lung parenchyma, (a_1)-(c_1) ground truth images, (a_2)-(c_2) segmentation results of the empirically fine-tuned version, (a_3)-(c_3) segmentation results of the automated version.

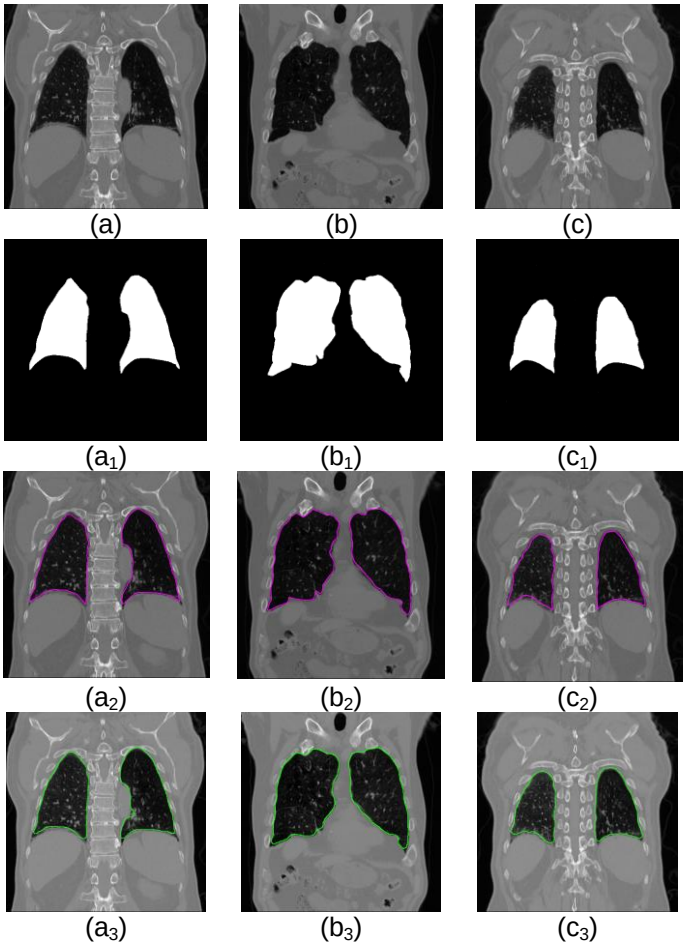

Figure 5.6: (a)-(c) Coronal *CT* scans of lung parenchyma, (a_1)-(c_1) ground truth images, (a_2)-(c_2) segmentation results of the empirically fine-tuned version, (a_3)-(c_3) segmentation results of the automated version.

5.2.6 Segmentation of Teeth on Gingiva Photographic Images

The fourth database consists of 40 labial teeth and gingiva photographic images randomly obtained by the *LTG-IDB* database [137] created by the Color Imaging Lab at the Optics Department of the University of Granada, Spain. For the image acquisition, a Canon EOS 7D digital single-lens reflex color camera combined with a Canon EFS 18-135 mm standard zoom lens was used. The scope of this database usage is the task of teeth/non-teeth segmentation. Figure 5.7 illustrates segmentation results obtained by the automated version on gingiva photographic images, as well as by the empirically fine-tuned version. It is evident that the segmentation results obtained by the automated version are alike the corresponding ground truth images, whereas the ones obtained by the empirically fine-tuned version differ from the ground truth images, more so in the left and right edges of each image (white arrows).

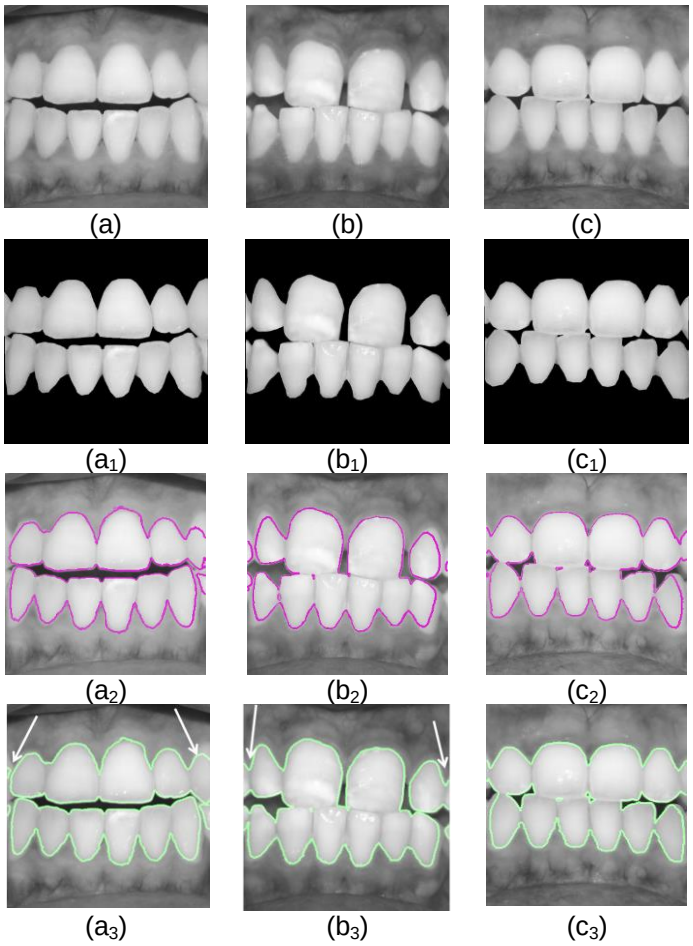

Figure 5.7: (a)-(c) Labial teeth and gingiva photographic images, (a_1)-(c_1) ground truth images, (a_2)-(c_2) segmentation results of the empirically fine-tuned version, (a_3)-(c_3) segmentation results of the automated version.

The segmentation results depicted in Figures 5.1-5.7 demonstrate that the presented framework achieves *comparable segmentation quality* to the one obtained by the empirically fine-tuned version *in an automated fashion*.

The experimental results are quantitatively evaluated by means of two metrics:

a) *TC* (*see Chapter 3, Eq. (3.4.1)*)

b) the Hausdorff distance *H* [145] defined as:

$$H(A,B) = \max_{a \in A} \min_{b \in B} ||a - b|| \tag{5.2.1}$$

where *A* is the ground truth set, *B* the set under evaluation and *a, b* the points defined in sets *A, B*, respectively. Table 5.1 presents *TC* and *H* values, obtained by both versions, for each utilized database.

Table 5.1: *TC* and *H* values for each utilized database

Database	***TC (%)***		***H (mm)***	
	Empirical	**Automated**	**Empirical**	**Automated**
Mini-MIAS	82.3±1.8	83.4±1.2	42.3±2.5	41.2±1.7
Thyroid US	82.8±1.2	83.7±0.8	43.7±3.3	41.7±2.1
Endoscopy	81.4±1.5	82.3±1.4	41.4±3.8	40.8±1.3
Dermoscopy Atlas	81.7±0.9	82.8±1.6	41.2±4.2	40.1±1.5
Axial *CT* scans	80.2±1.5	81.8±1.7	40.7±2.6	39.3±2.2
Coronal *CT* scans	82.5±1.8	83.8±1.3	42.2±4.2	41.2±1.6
LTG-IDB	82.9±1.6	84.2±1.8	44.8±5.7	42.4±2.5

The automated version achieves an average *TC* and *H* value of 83.1±1.4% and 40.9±1.8 mm, respectively *with regards to all images tested*, which is comparable to the *TC* and *H* value of 82.0±1.5% and 42.3±3.8 mm respectively obtained by the empirically fine-tuned version. This comparable segmentation accuracy verifies the value of the presented framework for automated parameter adjustment, without the need for laborious fine-tuning from *MDs*.

Aiming at highlighting the importance of the presented framework, further experiments are conducted in order to investigate the sensitivity of the empirical version to small alterations of parameters. The empirical version, except of being adjusted with optimal parameters, is also adjusted with parameters which are randomly set. Parameters w_{reg}^{fixed} and w_{df}^{fixed} were set to randomly selected values,

which fluctuated up to 10% from the optimal ones. Figure 5.8 depicts: (a) sample images of utilized databases, (b) segmentation results obtained by the empirically fine-tuned version and (c) segmentation results obtained by one case of the randomly-tuned version where w_{reg}^{fixed} and w_{df}^{fixed} were randomly set to $0.001 \cdot 255^2$ and 0.1, respectively. It is evident that, the segmentation results obtained by the randomly-tuned version differ significantly from the ones obtained by the fine-tuned version.

The randomly-tuned version achieves average *TC* and *H* of 58.3±1.7% and 62.1±1.9mm, respectively, *with respect to all values tested*, which differ significantly from the ones achieved by the fine-tuned version. Hence, the empirical version is sensitive even to small alterations of parameters and the segmentation results are highly questioned. On the contrary, the presented framework achieves a high segmentation quality in an automated fashion, endowing segmentation results with objectivity.

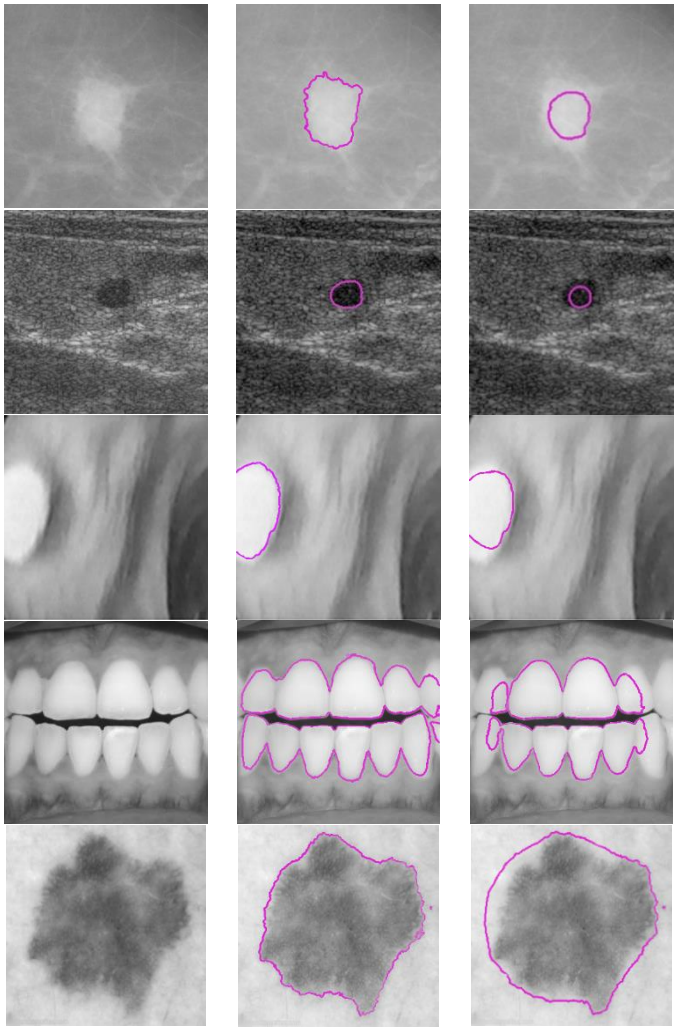

Figure 5.8: (a) Sample images of utilized databases, (b) segmentation results obtained by the empirically fine-tuned version and (c) segmentation results obtained by the randomly-tuned version.

Figure 5.9 illustrates the elapsed time of contour convergence for automated versus empirical parameterization, for each reference database. It is evident that, contour converges approximately 5-10 times faster in the case of the automated version. This is because region-based forces guiding contour evolution are appropriately amplified in randomly oriented, high-entropy regions, driving the contour away (*see Figure 3.7*). Hence, iterations dedicated to false local minima, which are associated with such regions, are avoided. On the contrary, in the case of empirical parameterization, region-based forces are uniformly weighted, irrespectively of the Orientation Entropy (*OE)*. Hence, the contour is delayed in false local minima and kept away from target edge regions for more iterations.

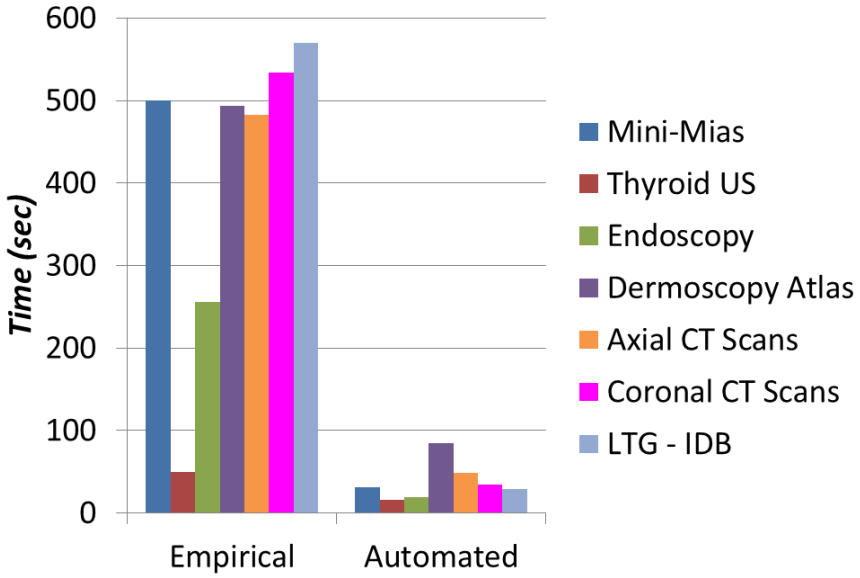

Figure 5.9: Elapsed time of contour convergence for automated versus empirical parameterization for each utilized database.

5.3 Summary

In this chapter, the novel framework for automated adjustment of *AC* regularization and data fidelity parameters is applied for medical image segmentation. This work is motivated by the need for automated parameterization, which is prominent in medical imaging applications, so as to relieve *MDs* from the laborious, time-consuming task of empirical parameterization and bolster the objectivity of the segmentation results.

The presented framework is validated on several medical image databases by comparing its segmentation performance with the empirically fine-tuned version. The experimental results demonstrate that the automated version *maintains a high segmentation quality, comparable to the one obtained empirically, yet in an unsupervised fashion*. Hence, *MDs* are set free from the laborious process of empirical parameterization and the objectivity of the results is enhanced.

CHAPTER 6

6. AN UNSUPERVISED *AC*-BASED MODEL FOR THE DETECTION AND SEGMENTATION OF PROTEOMICS IMAGES

6.1 Introduction

The emerging field of proteomics has progressed enormously in the past few years with the publication of the genome sequences of organisms. The complexity of the proteome intrigues researchers to study all the post-transcriptional control and Post-Translational Modifications (*PTMs)* maps, which decode the fundamental biological mechanisms. The goal is the quantitative assessment of protein expression. The latter is highly indicative of various pathological conditions ranging from neoplasms and tumors to infectious diseases and genetic disorders. In this light, protein patterns of normal and diseased origin are compared in order to allow the identification of possible differences in protein expression during the various cell-cycle stages. Proteomic research is challenged technically in the need of separation, characterization and quantification of thousands of complex protein mixtures (*see Chapter 4, § 4.2.3*). The computational analysis of protein content on *2D-GE* images is a challenging pattern recognition task, which involves several layers of processes including *2D-GE* image detection and segmentation.

In this chapter, a novel *AC*-based model is presented for the detection and segmentation of protein spots in *2D-GE* images. This is the first complete analysis model exploiting the appealing properties of the *AC* formulation in order to cope with crucial issues in *2D-GE* image analysis, including the presence of noise, streaks, multiplets and faint spots. In addition, it is unsupervised, providing an alternative to the laborious, error-prone process of manual editing, which is still required in state-of-the-art *2D-GE* image analysis software packages. The detection technique utilizes the dilation image operator [146], which embeds a disk-shaped Structuring Element (*SE*) [147], adjusted to the dominant roundish shape of protein spots. The disk-shaped *SE* limits the falsely detected streaks.

SE size is set considering that a certain radius value minimizes the detection of false negatives, whereas it allows the detection of local maxima associated with small spots, even in cases where they overlap with larger spots in complex regions. The presented detection technique imposes regional intensity constraints on the dilation-generated maxima so as to cope with the presence of noise and artifacts. The accompanying segmentation scheme comprises four main processes, namely: (a) a detection process capable of identifying boundaries of spot overlap in regions occupied by multiplets, based on the observation that such boundaries are associated with local intensity minima, (b) histogram adaptation and morphological reconstruction so as to avoid unwanted amplifications of noise and streaks, as well as to facilitate the identification of faint spots, (c) a contour initialization process aiming to form a level set surface initializing the subsequent level set evolution, based on the observation that protein spots are associated with regional intensity maxima and (d) a level set evolution process guided by region-based energy terms determined by image intensity as well as by information derived from the previous processes.

6.2 Protein Spot Detection

6.2.1 Mathematical Morphology (*MM*)

Mathematical Morphology (*MM*) [146] is a well-known image analysis approach, which can be applied for the extraction or suppression of image components of interest by probing the image with a suitable *SE* [147]. It is based on set theory, considering images as sets of points. Set operations such as union, intersection, addition and subtraction are performed between two sets; the target region and the *SE*. The key morphological operations are dilation and erosion, forming the basis for more complex operations such as opening and closing. Morphological operations are capable of preserving topological properties such as connectivity and homotopy [148], whereas they are suitable for detecting geometric characteristics, such as intensity peaks, which are associated with protein spots on *2D-GE* images. They have been successfully applied on various biomedical imaging domains, including electron micrographs of muscle cross-sections [149], gastric tumor pathologic cell images [150], digital color eye fundus images [151] as well as on *2D-GE* imaging [152], [153].

Morphological dilation involves the intensity transformation $I(x,y)$ of each pixel to the maximum intensity of a region centered on pixel (x,y). Each region is specified by a *SE* defined by $B(i,j)$ over a domain B_Δ . Pixel values within the region of the *SE* are marked either with one or zero. The morphological operation is applied on the neighborhood formed by pixels marked with one. The gray-scale dilation operator of $I(x,y)$ with $B(i,j)$ is denoted as $I \oplus B$ and defined by:

$$I \oplus B = \max\{I(x+i, y+j) + B(i,j) \mid (i,j) \in B_\Delta\} \tag{6.2.1}$$

The *SE* plays the exact same role as the convolution kernel in the linear filter theory (*see Chapter 2, § 2.3*). Figure 6.1 illustrates the dilation image operator on a sample image with a Four Nearest Neighbors (*4NN*) *SE*. The *SE* is placed over the upper left pixel until the whole image has been processed. The maximum intensity value within $B(i,j)$ centered to each $I(x,y)$ is set to the pixel (x,y) of the output image.

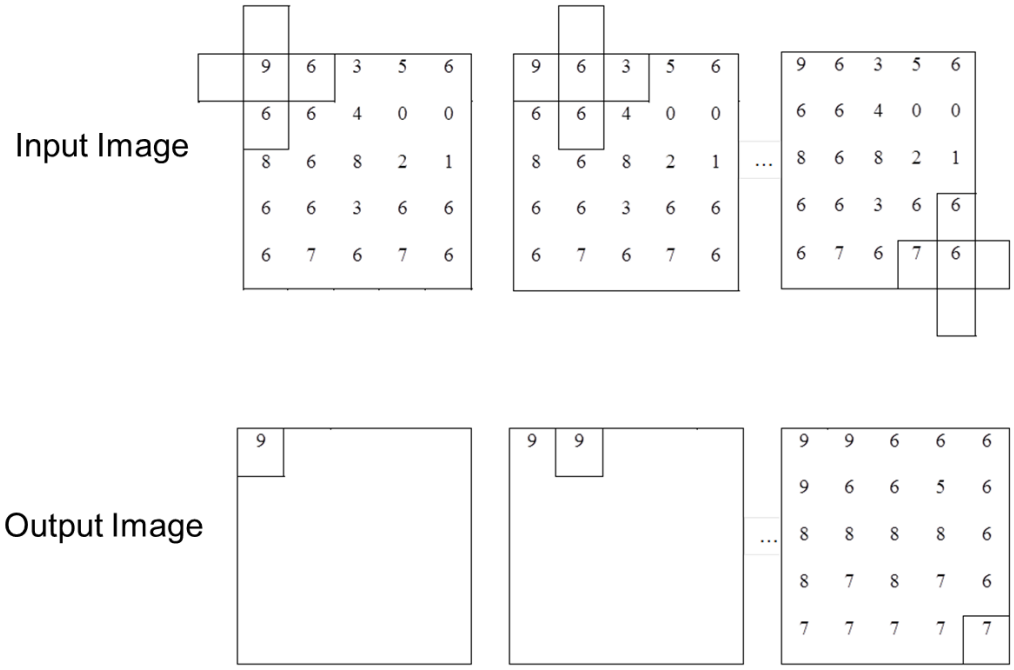

Figure 6.1: Dilation operator with a *4NN SE* on a sample image.

Variations in *SE* size and shape may alter the effect of morphological operations and should be taken into account [154]. Both are often selected in accordance with the shape of the target region [155]. Square and rectangular shapes are selected when the interest lies on edge detection, whereas in some cases a disk-shaped *SE* unrelated to directions may lead to better results. In the case of *2D-GE* images, the dominant shape of protein spots is circular. As it comes to size, a large disk tends to ignore most of regional intensity maxima. Based on these considerations, the *SE* is selected disk-shaped and the radius *R* is selected small in order to minimize missed regional intensity maxima. The latter are connected components of pixels with a constant intensity, bounded from pixels of lower intensity. A regional intensity maximum M at elevation t is defined by:

$$\left\{ \begin{array}{c} I(p) = t, \ \forall p \in M \\ I(p) < t, \ \forall p \in \delta_{SE}(M) \setminus M \end{array} \right\} \tag{6.2.2}$$

where p is the pixel location, $I(p)$ is the intensity of p and δ_{SE} is the region generated by the dilation of M according to the *SE*. It is evident that, a regional maximum M is not restricted to one pixel but is extended to a connected neighborhood M. The main attribute of M is that no higher intensity value exists in δ_{SE}. In the case of a *2D-GE* image, a regional intensity maximum is associated with a bright protein spot over a dark background, often corresponding to a saturated spot region.

6.2.2 Implementation

As a first step, median filtering is applied on the *2D-GE* image, so as to tackle with the presence of noise and minimize the detection of background intensity peaks. The application of the median filter on *2D-GE* images has been supported in literature [156]. In cases of *2D-GE* images depicting proteins spots as bright regions over a dark background, as the image illustrated in Figure 6.2(a), protein spots can be associated to regional intensity maxima. These maxima can be determined by means of Eq. (6.2.2). A disk-shaped *SE* is selected to form the

connected regions associated with the regional intensity maxima in agreement with the prevalent roundish shape of the majority of protein spots, ignoring rectangular-shaped streaks. *SE* radius *R* is set according to the results of preliminary experimentation on *2D-GE* images, considering that a certain radius value minimizes the detection of false negatives, whereas it allows the detection of local maxima associated with small spots even in cases where they overlap with larger spots in complex regions. Figure 6.2(b) illustrates the result of the dilation of the *2D-GE* image of Figure 6.2(a) with the utilized *SE*. The latter is illustrated in Figure 6.3.

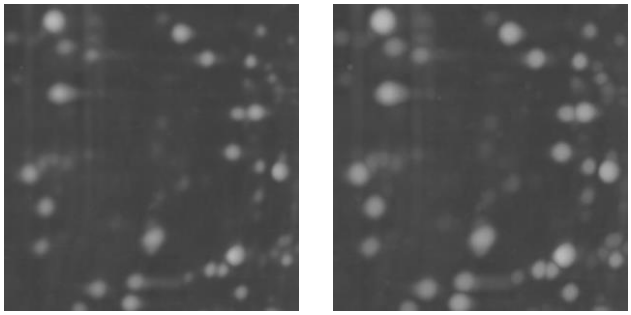

(a) (b)

Figure 6.2: (a) *2D-GE* image containing bright spots over a dark background, (b) dilation of the image of Figure 6.2(a) with a disk-shaped *SE*.

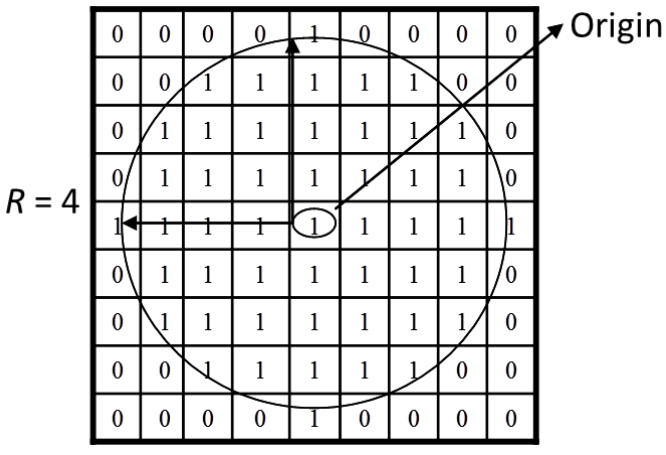

Figure 6.3: Disk-shaped *SE* of radius *R* = 4.

Regional intensity constraints are imposed on regional maxima in order to cope with the presence of noise and artifacts. The selection of regional intensity maxima is based on the following criteria:

a) intensity of the selected regional maxima should be equal to or higher than a $k \times k$ adjacent region. This constraint is applied so as to include salient maxima associated with spots and avoid local maxima associated with noise.

b) intensities of the $z \times z$ square neighborhood of each pixel of the selected regional maxima should exceed a threshold value T in order to avoid the detection of spurious maxima associated with unwanted artifacts and background peaks.

6.2.3 Experimental Evaluation on Detection Results

The presented technique has been experimentally evaluated on 13 real *2D-GE* images provided by the Biomedical Research Foundation of the Academy of Athens. The utilized dataset contains approximately 26,000 protein spots. The *2D-GE* images were obtained in a digital format at 16-bit gray level depth, with field of view of approximately 56810 mm² and size of 700×650 pixels. Three ground truth images were provided by the expert biologists of the Biomedical Research Foundation of the Academy of Athens for each *2D-GE* image. The application of the majority rule resulted in the final ground truth images used in the experiments performed. The algorithm has been implemented in Matlab R2009b [73] and executed on a 3.2 GHz Intel Pentium workstation.

Parameters T, k and R were set to 75, 8 and 4, respectively and were used in all experiments to follow based on the considerations listed below:

- threshold value T is selected equal to or lower than the intensity of the faintest spot so as to allow the detection of local maxima associated with faint spots,
- $k \times k$ size of adjacent region should be equal to or higher than 20 pixels considering that the typical size of a protein spot ranges from 20 to 300 pixels in order to allow the detection of local maxima associated with spots and avoid local maxima associated with noise and,

- radius *R* is selected smaller than the smallest protein spot radius in order to allow the detection of local maxima associated with small spots even in cases where they overlap with larger spots in complex regions.

Parameters *T*, *k* and *R* are not directly affected by the total image size. However, as it can be derived from the considerations listed above, parameters *k* and *R* are affected by the range of protein spot sizes in pixels, which is determined by image resolution. In addition, parameters *k* and *R* are invariable to image contrast, as opposed to parameter *T*. The latter decreases as image contrast increases, since contrast increase lowers faint spot intensities, which provide the upper bound of *T*, as described.

Melanie 7 [112] software package is used for comparisons. Melanie 7 parameters “smooth”, “saliency” and “min area” were set to 4, 70 and 60, respectively. These values were selected by an expert biologist, following his experience. According to the documentation provided with Melanie 7: a) “smooth” parameter determines the number of iterative executions of the diffusion smoothing algorithm, which is a component of Melanie 7, b) “saliency” parameter indicates how far a spot stands out with respect to its environment. Real spots generally have high saliency values whereas artifacts and background noise have small saliencies, c) “min area” parameter eliminates spots of area smaller than the specified value, which is expressed in number of pixels.

Figures 6.4(a)-(c) illustrate three of the final ground truth images, whereas Figures 6.4(d)-(f) depict the detection results obtained by Melanie 7 software package. It can be observed that, much more actual protein spots are missed (red arrows), whereas more artifacts are falsely detected as spots (green arrows), especially in the cases of Figure 6.4(e),(f).

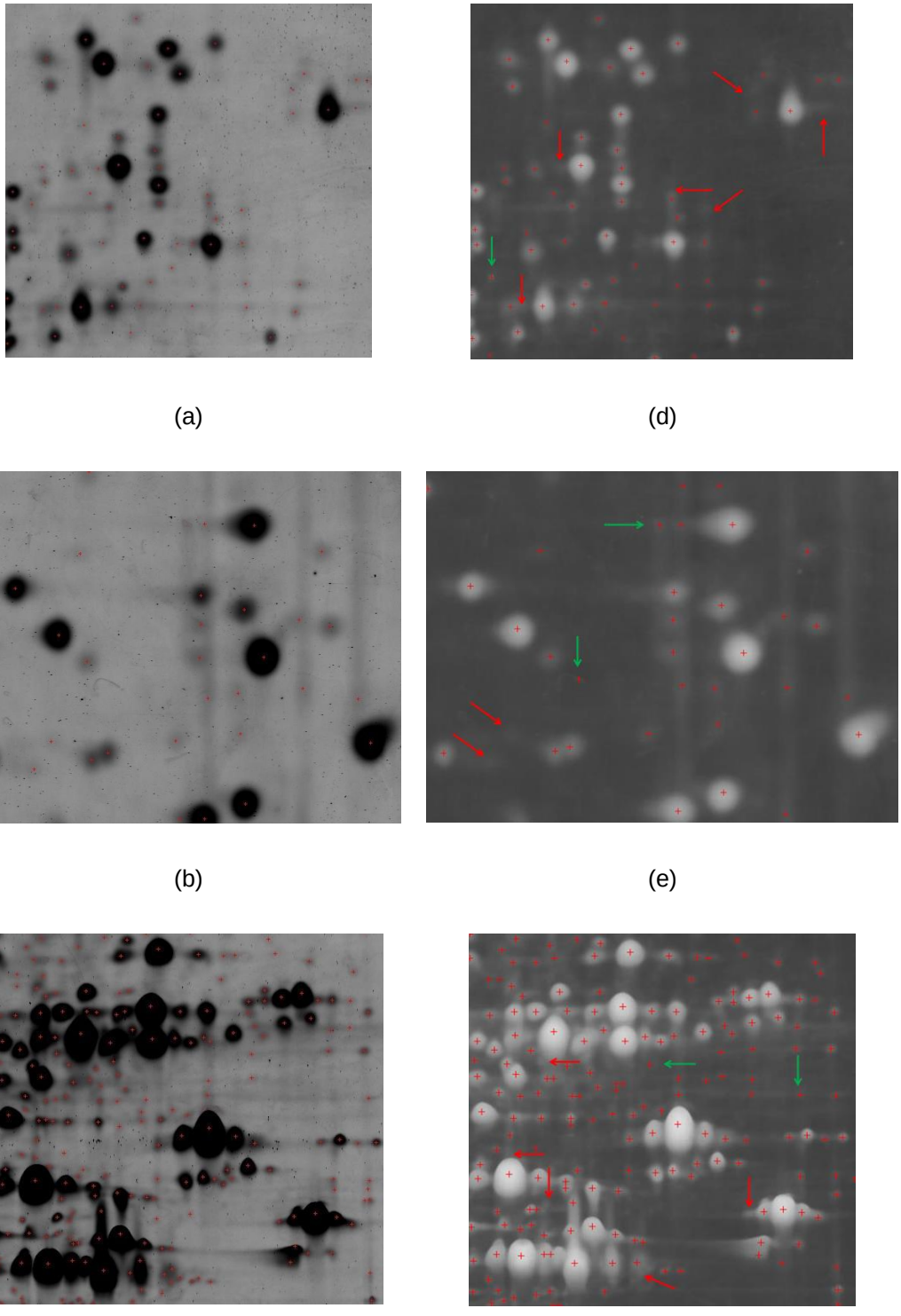

Figure 6.4: (a)-(c) Ground truth images, (d)-(f) detection results obtained by Melanie 7 [112].

Figures 6.5(a)-(c) illustrate the ground truth images, whereas Figures 6.5(d)-(f) depict the detection results obtained by the presented detection technique. It is evident that, the vast majority of the actual protein spots are correctly detected.

For instance, in the case of Figure 6.4(e) and 6.5(e) Melanie 7 and the presented technique detected 31 and 27 spots, respectively out of a total of 28 protein spots.

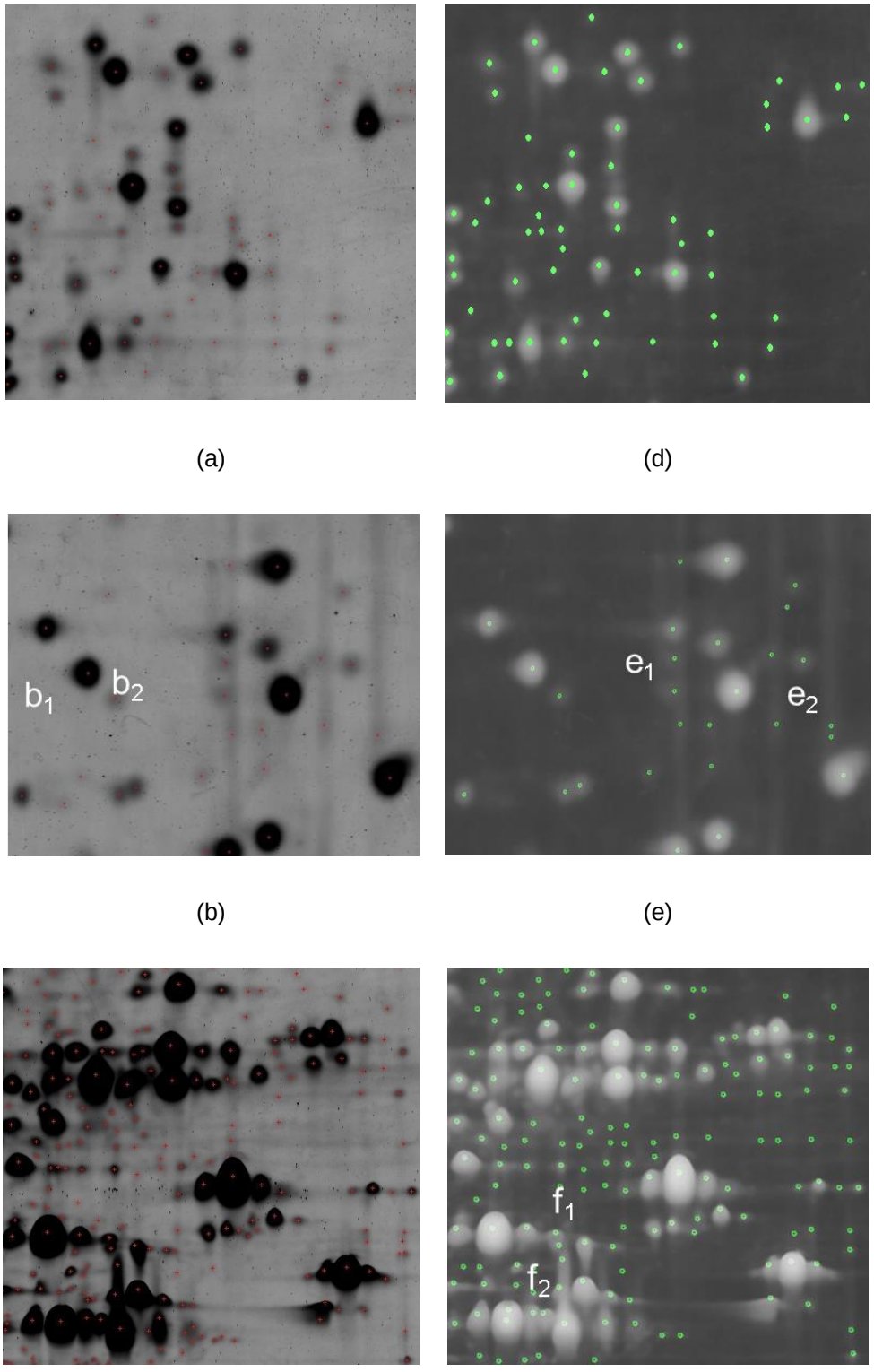

(a) (d)

(b) (e)

(c) (f)

Figure 6.5: (a)-(c) Ground truth images, (d)-(f) detection results obtained by the presented detection technique.

The detection results are quantified by means of the Predictive Value (*PV*), Specificity (*SP*) and Detection Sensitivity (*DS*) [157], which are defined as:

$$PV = \frac{TP}{TP + FP}, \quad SP = \frac{TN}{TN + FP}, \quad DS = \frac{TP}{FN + TP} \tag{6.2.3}$$

where True Positives (*TP*) and False Negatives (*FN*) are defined as correctly detected and falsely detected spots. *TP* and *FN* are calculated based on the final ground truth images. Table 6.1 presents *PV*, *SP* and *DS* obtained by Melanie 7 and the presented detection technique for each *2D-GE* image of Figure 6.4. The presented technique obtains a *DS*, which exceeds 90% in all image cases. In the cases of Figure 6.5(d) and 6.5(e) it misses only 4 and 2 actual protein spots out of 57 and 26, respectively. In the case of the *2D-GE* image of Figure 6.5(f), the presented technique misses 17 out of a total of 154 protein spots. These *FN* cases are a side effect of median filtering, which may affect some regional intensity maxima.

Table 6.1: Indicative detection results obtained by Melanie 7 and the presented detection technique

	Melanie 7			**Presented Detection Technique**		
Image of Figure 6.4	***PV(%)***	***SP(%)***	***DS(%)***	***PV(%)***	***SP(%)***	***DS(%)***
d	90	43	90	92	83	93
e	90	35	89	91	81	92
f	75	25	85	85	77	90

The comparison of *PV*, *SP* and *DS* presented in Table 6.1 lead to the conclusion that the presented detection technique outperforms Melanie 7 software package in all image cases. Figure 6.6 illustrates detailed sub-images of the images of Figure 6.5, so as to focus on the response of the presented detection technique with respect to the presence of overlapping spot regions, streaks and artifacts. The detailed sub-images of Figures 6.6(a),(b) depict complex regions with multiple overlapping spots. In both cases, it manages to separately detect each overlapping spot. This discriminative capability of the presented technique is attributed to the size of the *SE*, which is smaller than the protein spot sizes.

Figures 6.6(c),(d) illustrate sub-images containing multiple vertical streaks. Such streaks occur due to flawed calibration or insufficient *SDS* in electrophoresis buffer (*see Chapter 4, § 4.2.3*) and pose difficulties for the consistent spot detection by biologists. The main challenge is the localization of protein spots within streaks. The presented technique succeeds in detecting such spots. The *DS* of the presented technique in such cases can be attributed to the utilization of the disk-shaped *SE*, which tends to ignore the rectangular-shaped streaks.

Figures 6.6(e),(f) present sub-images containing artifacts. In both cases, the presented technique correctly ignores all artifacts present. This can be attributed to the selectivity of the constraints imposed, which are parameterized so as to select salient intensity maxima.

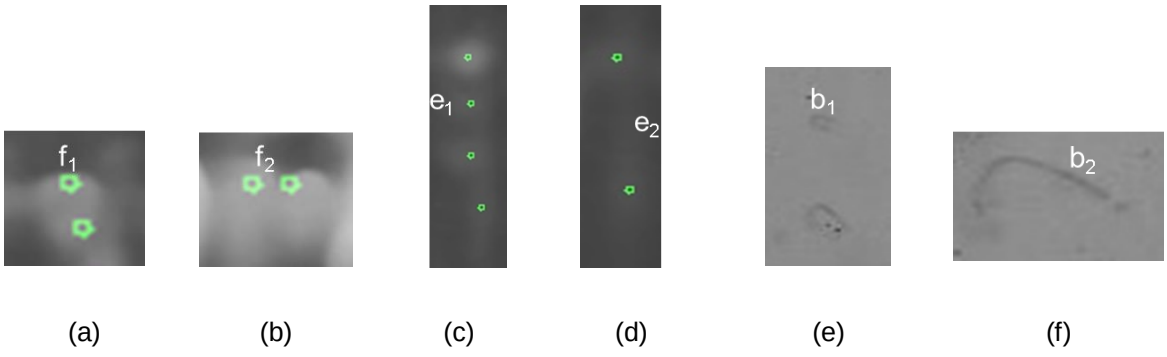

Figure 6.6: Detailed sub-images containing overlapping spots (a),(b), vertical streaks (c),(d) and artifacts (e),(f), extracted from Figure 6.5(f),(e) and (b), respectively.

Table 6.2 presents the *PV*, *SP* and *DS* obtained by the presented detection technique and Melanie 7, in a total of approximately 26,000 protein spots appearing in a dataset of 13 *2D-GE* images. Figure 6.7 provides a visualization of the results of Table 6.2. It is evident that, the presented detection technique outperforms Melanie 7 in terms of all performance criteria. In addition, *ANOVA* has been performed so as to validate the statistical significance of the obtained results. *ANOVA* involves the so-called null hypothesis testing, where the null hypothesis is that the means among the compared populations are equal, under the assumption that these populations are normally distributed [158]. *ANOVA* yielded a *p*-value of less than 0.05 for all performance criteria, indicating that the performance difference of the presented detection technique and Melanie 7 is statistically significant.

Table 6.2: Overall detection results obtained by Melanie 7 and the presented detection technique

	Melanie 7		**Presented Detection Technique**	
	mean	**standard deviation**	**mean**	**standard deviation**
PV(%)	73.6	17.4	88.2	4.2
SP(%)	33.2	13.5	81.6	5.3
DS(%)	77.4	12.6	87.3	6.2

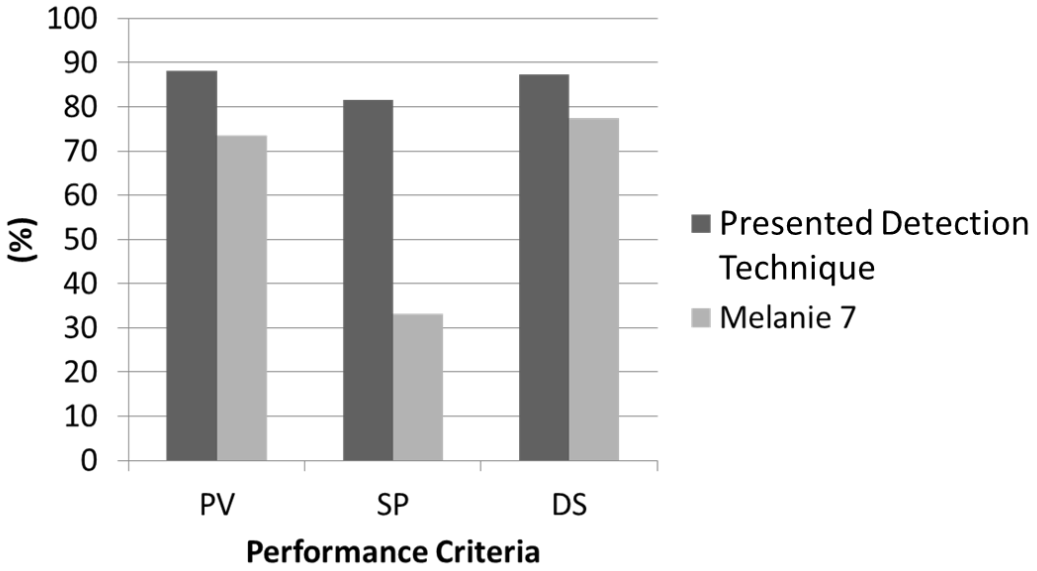

Figure 6.7: Overall detection results in terms of *PV*, *SP* and *DS*, obtained by the presented detection technique and Melanie 7.

Considering the experimental evaluation it can be concluded that the presented detection technique achieves a *PV* and a *DS* which exceed 80%, outperforms Melanie 7, distinguishes multiple overlapping spots, locates spots within streaks and ignores artifacts.

6.3 Protein Spot Segmentation

The presented segmentation scheme is based on the Chan-Vese model [2] and comprises four main processes: (a) separation of multiplets, (b) histogram adaptation and morphological reconstruction, (c) level set initialization and (d) contour evolution.

6.3.1 Separation of Multiplets Based on Directionality

It can be observed that, the region of overlap between two protein spots is associated with local intensity minima, with respect to a particular direction. Figure 6.8 illustrates this point by three-dimensional representations of protein spot intensities, in cases of partly overlapped (*see Figure 6.8(a)*) and highly overlapped (*see Figure 6.8(b)*) protein spots. This observation yielded to the

incorporation of information derived by such local intensity minima in the presented *2D-GE* image segmentation scheme.

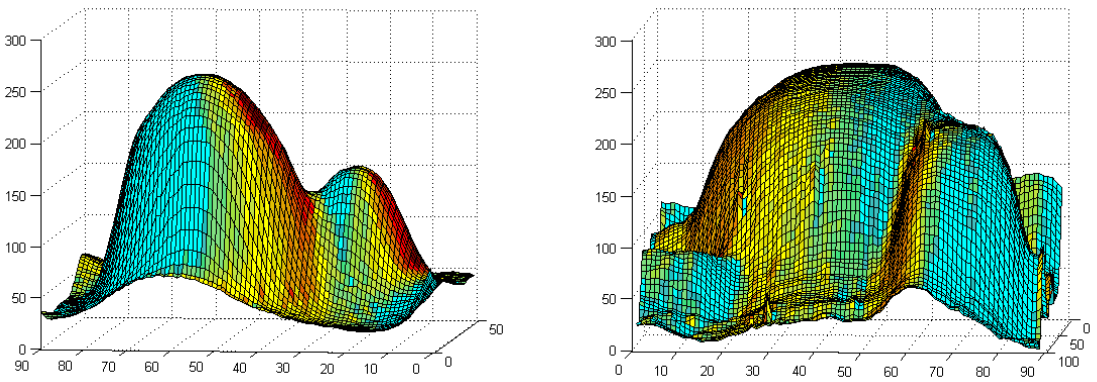

(a) (b)

Figure 6.8: 3D representations of protein spots: (a) partly overlapped and (b) highly overlapped.

The original *2D-GE* image is pre-processed with median filtering [156] aiming to reduce the side effects of noise on the following processes. The pre-processed image is scanned with parallel straight-line segments of variable lengths and multiple directions (*see Figure 6.9*), so as to facilitate the detection of local intensity minima, associated with each particular direction.

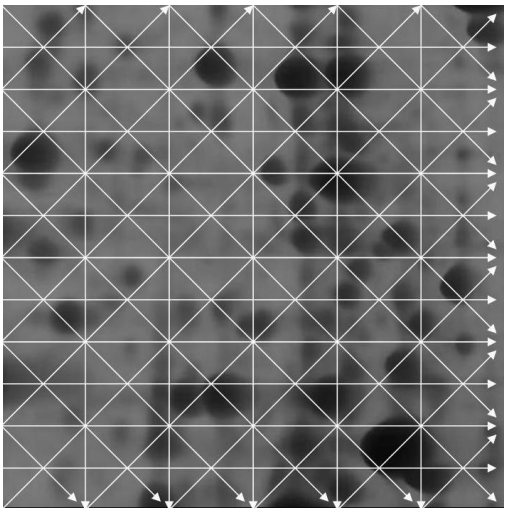

Figure 6.9: Multiple directions of straight-line segments for local intensity minima detection.

Local intensity minima are identified for each parallel straight-line segment. However, the ones which are eventually selected conform to the following two criteria: a) intensity value exceeds a threshold value T_1 and b) intensity value is a global minimum over a square sub-segment of width exceeding a minimum value *w*. These criteria are imposed to exclude local intensity minima associated with background clutter. Figure 6.10 illustrates: a) a real *2D-GE* image, b) the detection results obtained by the local intensity minima process, with each minimum marked as black and (a_1)-(b_1) respective sub-images as marked in (a) and (b). In Figure 6.10(b_1) it is evident that, the detection process actually identifies boundaries of spot overlap. Therefore, alterations in the pre-processing techniques as well as further manual editing are not required.

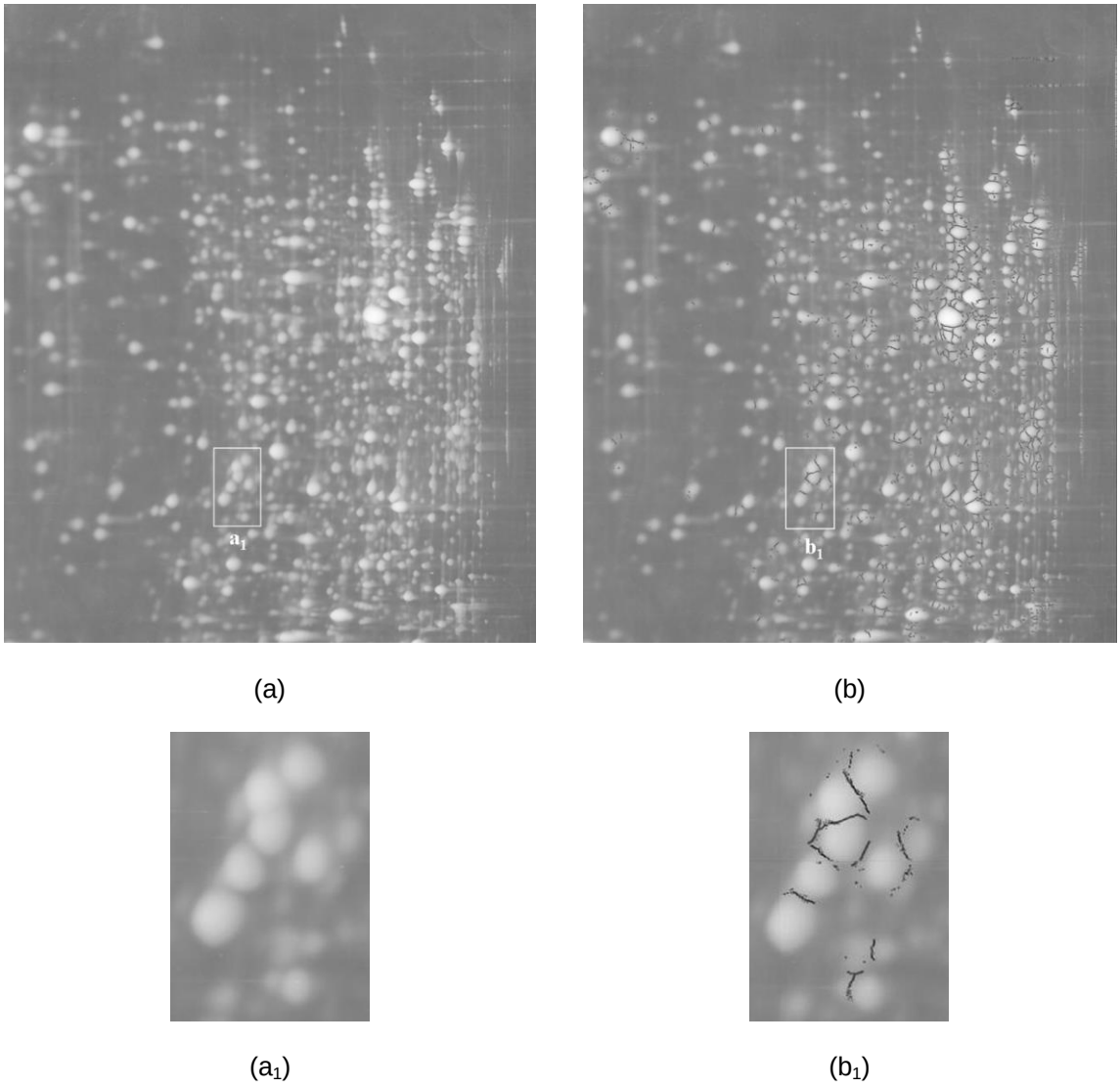

Figure 6.10: (a) Real *2D-GE* image, (b) detection results obtained by the local intensity minima process, (a_1) sub-image of (a), and (b_1) sub-image of (b).

6.3.2 Enhancement of Faint Spots Using *CLAHE* and *MM*

A popular histogram equalization variant called Contrast-Limited Adaptive Histogram Equalization (*CLAHE*) [159] is utilized to enhance the segmentation performance of the presented scheme with respect to the presence of faint spots in *2D-GE* images. *CLAHE* involves a grayscale transformation function which has been effectively applied on various medical imaging modalities including mammographic [160] and chest *CT* [161] imaging. The core idea is to adaptively enhance image contrast in a local fashion, contrary to the original histogram equalization which is uniformly applied on the entire image.

CLAHE separately applies histogram equalization on $n \times n$ small non-overlapping image regions called tiles. The histogram of each transformed tile approximates the uniform distribution, which results in amplification of faint regions such as the faint protein spots in *2D-GE* images. The local nature of *CLAHE* prevents unwanted amplifications of noise and streaks, as opposed to the original histogram equalization which has the same amplifying effect on noise and artifacts as on faint spots. In addition, *CLAHE* imposes a constraint on the resulting contrast providing a mechanism to cope with a possible over-saturation of the resulting image. This constraint can be adjusted by a parameter *h*, called clip limit. The clip limit *h* determines the maximum number of pixels which are allowed to occupy a bin in the resulting histogram. In cases of over-saturation, where certain histogram bins are occupied by more than $h \times (2^{gray\ level\ depth} - 1)$ pixels, the excessive amount of pixels is redistributed over the rest of the histogram. The neighboring transformed tiles are then merged using bilinear interpolation to reduce artificially induced boundaries and the pixel intensity values are updated in accordance with the adapted histograms [162].

Figure 6.11 illustrates the images resulted from the application of: (a) histogram equalization and (b) *CLAHE*, on the original *2D-GE* image of Figure 6.10(b). A sub-image of this original *2D-GE* image is illustrated in Figure 6.11(c), whereas the corresponding sub-images of Figure 6.11(a) and (b) are magnified in Figure 6.11(a_1) and (b_1), respectively. It can be observed that, both techniques amplify spots which were faint in the original *2D-GE* image; however *CLAHE* avoids

unwanted amplifications of noise and streaks, which is not the case with the plain histogram equalization. Figure 6.12 illustrates the histograms of: (a) the original *2D-GE* image illustrated in Figure 6.10(b), as well as the histograms of the images illustrated in: (b) Figure 6.11(a) and (c) Figure 6.11(b). It can be observed that the histogram of the image resulted from the application of *CLAHE,* is much denser than the one generated by plain histogram equalization, indicating that the former maintains much more detailed image-related information.

It should be noted that, the application of *CLAHE* could not benefit the detection of local intensity minima, as well as the contour initialization process which is described later on. Accordingly, both processes are applied on the original *2D-GE* image. This can be justified by considering that the clipping involved in *CLAHE* redistributes pixels over the histogram, introducing intensity minima which are not necessarily associated with spot boundaries, as well intensity maxima which are not necessarily associated with spots.

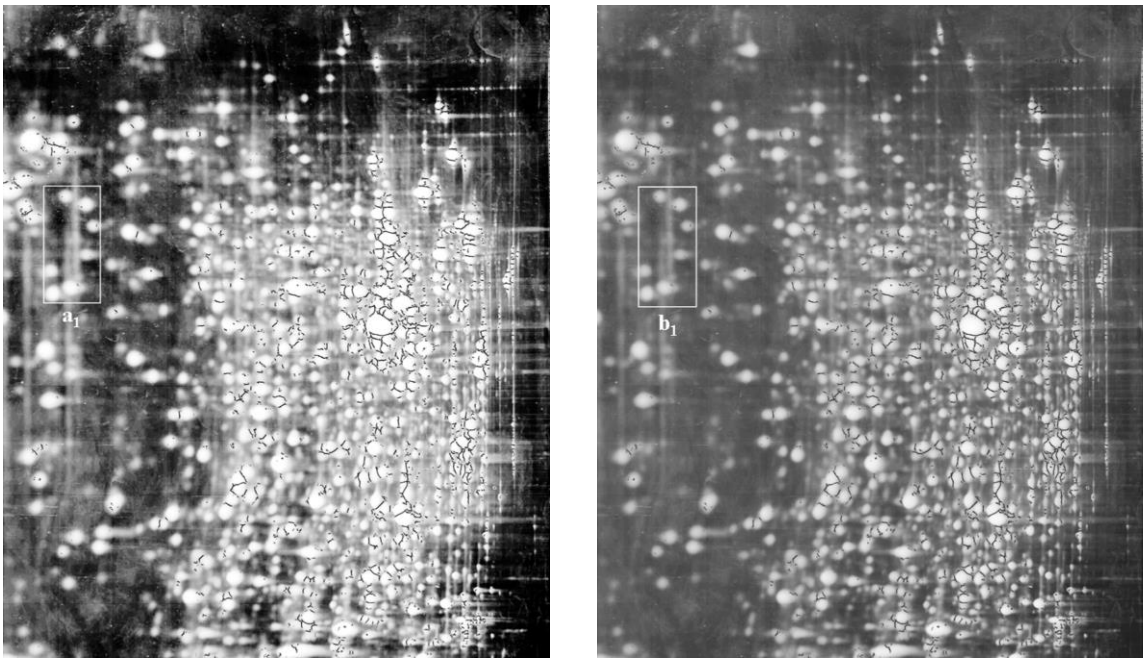

(a) (b)

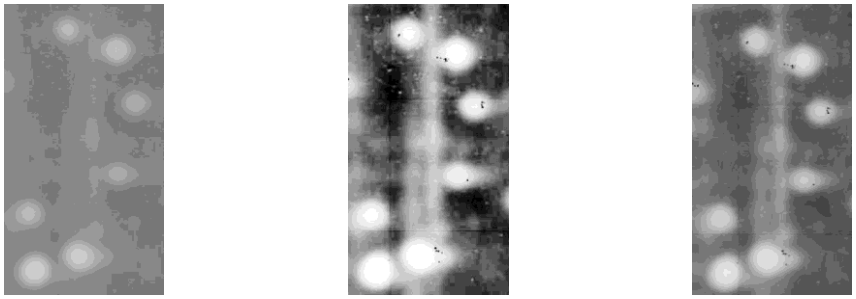

(c) (a_1) (b_1)

Figure 6.11: *2D-GE* images obtained by the application of: (a) histogram equalization and (b) *CLAHE*, on the *2D-GE* image of Figure 6.10(b). A sub-image of the original *2D-GE* image is illustrated in (c), whereas the corresponding sub-images of (a) and (b) are magnified in (a_1) and (b_1), respectively.

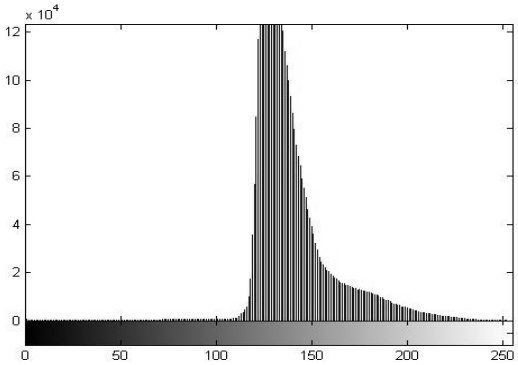

(a)

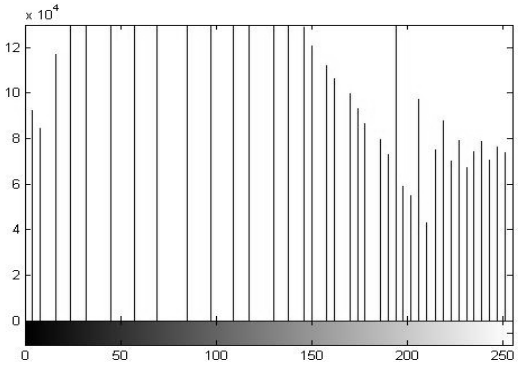

(b)

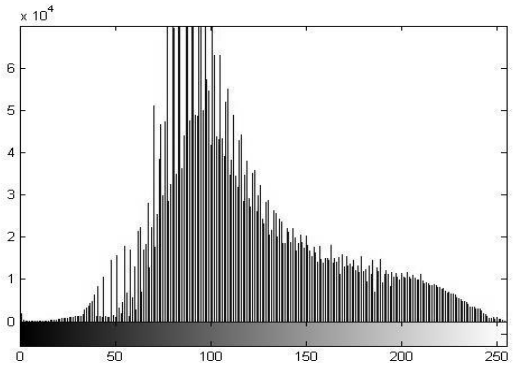

(c)

Figure 6.12: Histograms of: (a) the original *2D-GE* image, (b) the image resulted from the application of histogram equalization on the image of Figure 6.11(a) and (c) the image resulted from the application of *CLAHE* on Figure 6.11(b).

The protein spot regions depicted on the enhanced image generated by *CLAHE* are still characterized by intensity inhomogeneity which would affect the subsequent *AC* evolution. Another morphological processing step is performed in order to cope with this issue. The enhanced image is binarized according to a threshold value T_2. However, the protein spot regions of the binary image contain holes as a result of intensity inhomogeneity. The flood-fill morphological operation [146] is applied so as to eliminate such holes. This morphological operation alters the connected background pixels to foreground pixels until it reaches the target boundaries.

Figure 6.13 illustrates the results obtained by the flood-fill morphological operation on: (a) the original *2D-GE* image illustrated in Figure 6.10(b) and (b) on the enhanced image of Figure 6.11(b), which is generated by the application of *CLAHE*. A sub-image of the original *2D-GE* image is illustrated in (c), whereas (a_1) and (b_1) are the corresponding sub-images of Figure 6.13(a) and (b), respectively. Missing regions in Figure 6.13(a_1), as compared to Figure 6.13(b_1), correspond to faint protein spots. It is evident that, the utilization of *CLAHE* is essential, since most faint spots are missed when *CLAHE* is omitted. The obtained binarized image represents protein spots, including faint ones, as well as the boundaries of spot overlap in regions occupied by multiplets. This indispensable information is incorporated into the later stage of contour evolution.

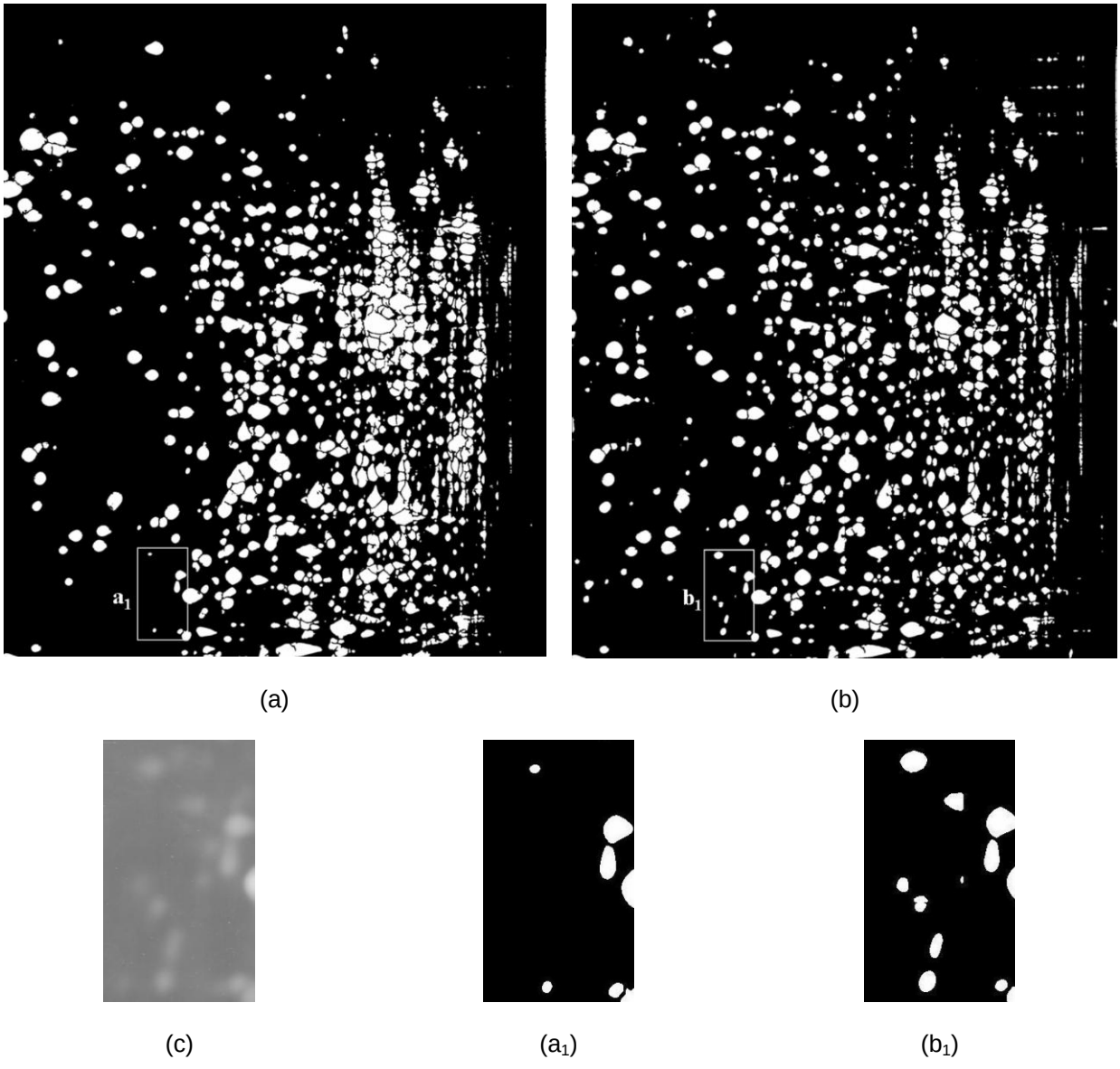

Figure 6.13: Results obtained by the flood-fill morphological operation on: (a) the image illustrated in Figure 6.10(b) and (b) on the enhanced image of Figure 6.11(b), which is generated by the application of *CLAHE*. A sub-image of the original *2D-GE* image is illustrated in (c), whereas (a_1) and (b_1) are the corresponding sub-images of (a) and (b), respectively.

6.3.3 Automatically Initialized Level Set Function

The Chan-Vese model is not completely insensitive to initialization [163]. It suffers in the sense that it is susceptible to the initial level set surface, which is often manually determined. Figure 6.14 illustrates segmentation results obtained by the straightforward application of the Chan-Vese model where the contour is initialized: (a) inside a protein spot, (b) to embed a single protein spot and (c) to

embed multiple protein spots. It is evident that, the convergence state is subject to initial contour positioning.

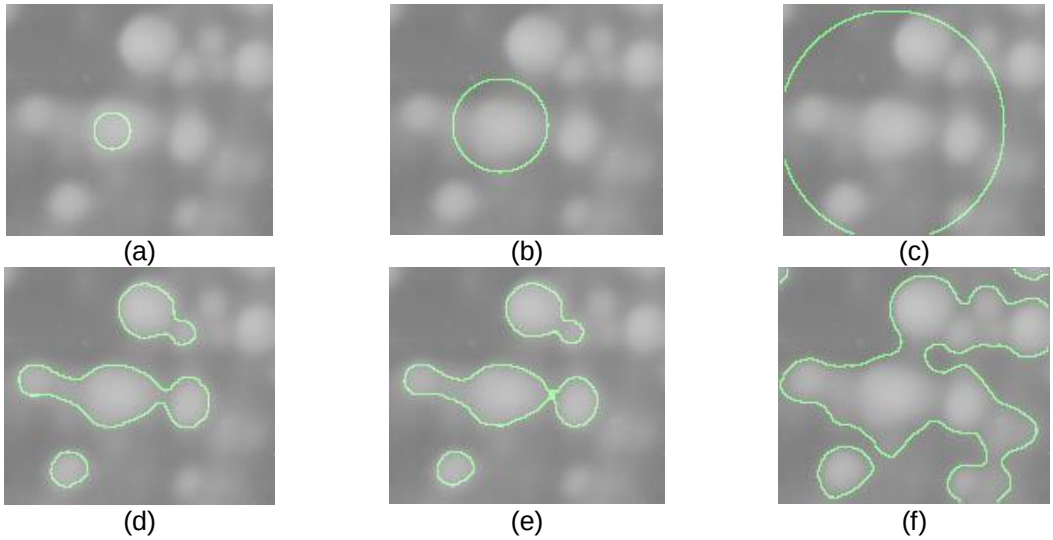

Figure 6.14: The initial contour: (a) is positioned inside a protein spot, (b) embeds a protein spot and (c) embeds the majority of protein spots, (d)-(f) segmentation results emerged from the application of the Chan-Vese model according to the initialization of (a)-(c), respectively after 200 iterations.

Hitherto, it is essential to initialize the level set function so that the associated zero levels approximate the actual protein spots. Starting from the observation that regional intensity maxima of a *2D-GE* image are associated with protein spots, the presented initialization process constructs a level set surface of multiple cones centered at maxima positions. This surface can serve as a spot-targeted initialization of the level set function. Such an initialization process is particularly important within the context of the presented segmentation scheme, in the sense that it provides the capability of unsupervised segmentation. In this light, this process is one of the novel elements of the presented scheme, since it extends a straightforward *AC* application, which would have required supervised initialization in order to avoid sub-optimal segmentation results. It should be noted that, the level set function is initialized on the *2D-GE* image instead of the binarized image described in the previous process, since regional intensity maxima are not maintained in the latter image.

The positions of regional intensity maxima selected in the detection process are used as centers of cones forming the surface of the initial level set function. Apart

from cone centers, the presented initialization process determines the zero-level regions associated with each cone. Figure 6.15 illustrates a three-dimensional representation of the level set surface of multiple cones obtained by the application of the presented initialization process on a real *2D-GE* image.

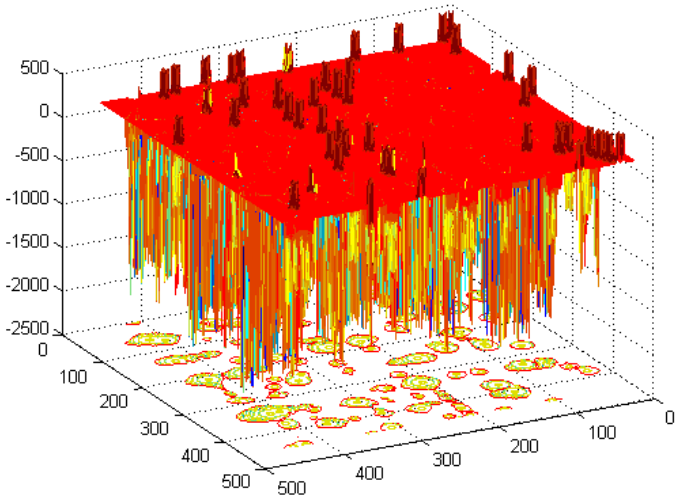

Figure 6.15: 3D representation of the level set surface of multiple cones obtained by the application of the presented initialization process on a real *2D-GE* image.

6.3.4 Contour Evolution Endowed with Information on Multiplets and Faint Spots

Aiming to enhance segmentation performance, contour evolution is initialized by the spot-targeted level set surface generated by the previous initialization process. In addition, the *AC* evolves in separate $g \times g$ image sub-regions, which are centered at the cone centers of the level set surface. The *AC* converges according to the following equation:

$$\begin{aligned}\frac{\partial \varphi}{\partial t} &= w_{reg}^{fixed} \cdot \delta(\varphi(x,y)) \cdot div\left(\frac{\nabla \varphi}{|\nabla \varphi|}\right) \\ &- w_{df_1}^{fixed} \cdot (I_1(x,y) - c_1)^2 + w_{df_1}^{fixed} \cdot (I_1(x,y) - c_2)^2 \\ &- w_{df_2}^{fixed} \cdot (I_2(x,y) - c_3)^2 + w_{df_2}^{fixed} \cdot (I_2(x,y) - c_4)^2\end{aligned} \tag{6.3.1}$$

where I_1, I_2 are the original image and the binarized image which is the output of morphological processing, respectively, c_1, c_2 and c_3, c_4 the average intensities inside and outside of the contour of I_1 and I_2, respectively, w_{reg}^{fixed} the fixed regularization parameter, $w_{df_1}^{fixed}$ and $w_{df_2}^{fixed}$ the fixed data fidelity parameters of I_1 and I_2, respectively.

Equation (6.3.1) describing contour evolution of the presented scheme extends (2.5.17) in the sense that it encompasses information derived by: 1) the original *2D-GE* image I_1, 2) the binarized image I_2 obtained by the application of *CLAHE* and morphological processing of the original *2D-GE* image. The latter information is essential to identify the presence of faint spots as well as the boundaries of spot overlap in regions occupied by multiplets.

6.3.5 Experimental Evaluation on Segmentation Results

The experimental evaluation of the presented segmentation scheme has been conducted on a dataset of 13 real digital grayscale *2D-GE* images provided by the Biomedical Research Foundation of the Academy of Athens, as well as on a dataset of 30 synthetic *2D-GE* images, so as to facilitate qualitative and quantitative comparisons with state-of-the-art *2D-GE* image analysis software packages. The size of each real and synthetic *2D-GE* image used was approximately 2000×3000 and 1500×2000 pixels respectively, whereas image gray-level depth of both image types was 16-bit. The presented segmentation scheme has been implemented in Matlab R2009b [73] and executed on a 3.2 GHz Intel Pentium workstation.

Effects of Parameter Settings

Parameter tuning was based on preliminary experimentation, which resulted in the values presented in Table 6.3. The preliminary experiments were performed on three pilot *2D-GE* images, whereas the search on the parameter space was guided by the following considerations:

- the width *w* of the square sub-segment considered in local intensity minima detection as well as the size *z* of the square neighborhood considered in contour initialization process, were all set to 3. This value is the smallest value for these two parameters, whereas higher values of both *w* and *z* resulted in slight reduction of the obtained segmentation quality,

- thresholds T_1, T_2, T_3 were experimentally identified as 150, 160 and 75, since these values approximate: 1) the upper extreme of the intensity range of the background clutter, 2) the lower extreme of the intensity range of faint spots on the images resulted from histogram equalization and, 3) the lower extreme of the intensity range of faint spots on the original *2D-GE* images, respectively. Perturbations of T_1, T_2, T_3 within the ranges [147,152], [158,162] and [72, 77], resulted in insignificant variations of the obtained segmentation quality,

- tile size *n* considered for *CLAHE* was experimentally identified as 40, since this values approximates the typical size of a faint protein spot. Perturbations of *n* within the range [37, 42] resulted in insignificant variations of the obtained segmentation quality,

- clip limit *h* is set to 0.01 since this order of magnitude reduces over-saturation and leads to the optimal segmentation quality in all pilot *2D-GE* images. Perturbations of *h* within the range [0.006, 0.03] resulted in insignificant variations of the obtained segmentation quality,

- size *m* of adjacent regions and radius *r* considered in contour initialization process as well as image sub-region size *g* considered in contour evolution process were experimentally identified as 20, 4 and 50, since these values approximate: 1) the lower extreme of protein spot sizes and consider salient intensity maxima associated with protein spots, 2) the lower extreme of protein spot radii and allow the detection of regional intensity maxima in cases of small spots overlapping with larger spots in multiplets and 3) the average size of a typical protein spot. Perturbations of *m*, *r* and *g* within the ranges [17, 24], [3, 5]

and [42, 59] resulted in insignificant variations of the obtained segmentation quality,

- following relevant literature [2], the weights of the energy terms $w_{df_1}^{fixed}$ and $w_{df_2}^{fixed}$ were set to 1 whereas the weight w_{reg}^{fixed} was adjusted to $0.006 \cdot 255^2$, since this value leads to the optimal segmentation quality in all pilot *2D-GE* images. Perturbations of w_{reg}^{fixed} within the range $[0.003 \cdot 255^2, 0.009 \cdot 255^2]$ resulted in insignificant variations of the obtained segmentation quality.

The variations in segmentation quality are considered insignificant when the values of the associated segmentation quality measures (i.e. *VO* and *VE*, as defined in Eq. (6.3.5)), derived for each one of the three pilot *2D-GE* images are overlapping. The latter occurs when the values of the segmentation quality measure derived for a pilot *2D-GE* image are within the ranges defined by the mean values and the standard deviations of the same measure, as derived for the other two pilot *2D-GE* images. It should be pointed out that, parameter tuning is performed once on a small number of pilot *2D-GE* images generated with a certain experimental setup (pH, staining etc.) and the resulting parameter values can be used for all *2D-GE* images generated with the same setup. On the contrary, state-of-the-art software packages require parameter tuning for each single *2D-GE* image, as confirmed by expert biologists.

Table 6.3: Parameter values

Detection of local intensity minima in multiplets	$k = 3$	$T_1 = 150$	$w = 3$	
Image enhancement and morphological reconstruction	$n = 40$	$h = 0.01$	$T_2 = 160$	
Contour initialization	$m = 20$	$z = 3$	$T_3 = 75$	$r = 4$
Contour evolution	$g = 50$	$w_{reg}^{fixed} = 0.006 \cdot 255^2$	$w_{df_1}^{fixed} = 1$	$w_{df_2}^{fixed} = 1$

Real *2D-GE* Images

Figure 6.16 illustrates example segmentation results obtained by the application of PDQuest 8.0.1 [113], Melanie 7 [112], Delta2D and the presented segmentation scheme on a real *2D-GE* image. It should be noted that, the output images resulting from the application of the software packages varied with respect to size and resolution. The software packages were applied on inverted versions of the *2D-GE* images, whereas parameter settings and calibrations involved were performed by expert biologists, following their experience.

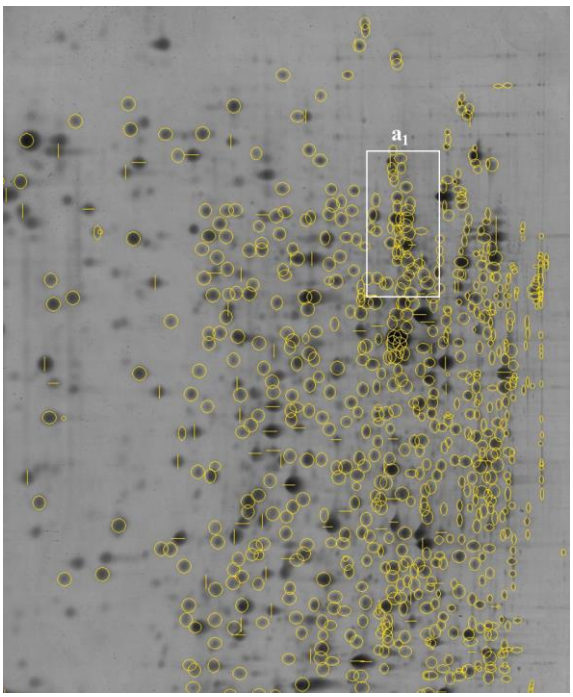

(a)

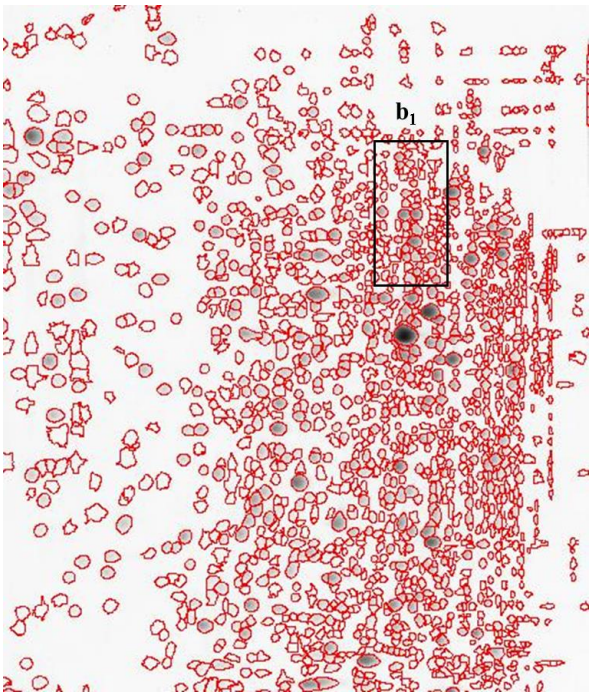

(b)

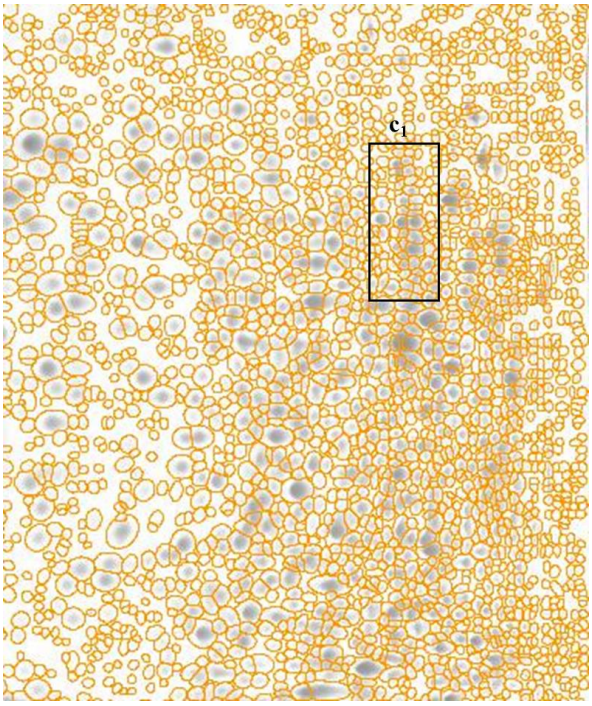

(c)

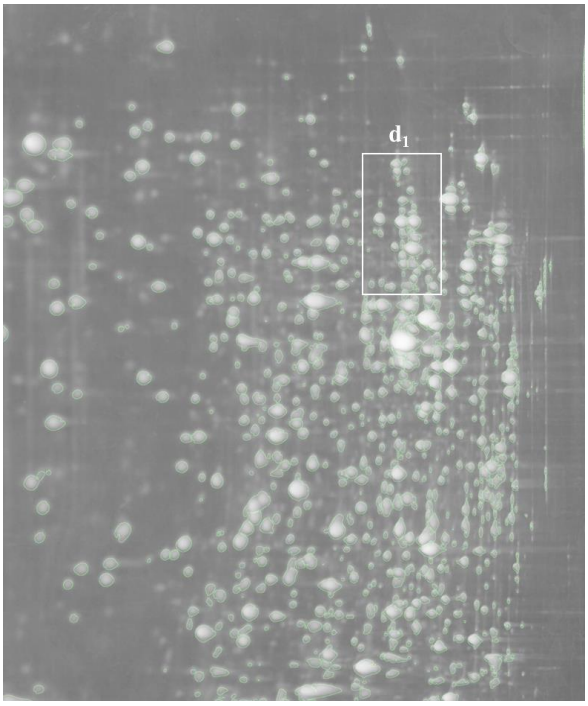

(d)

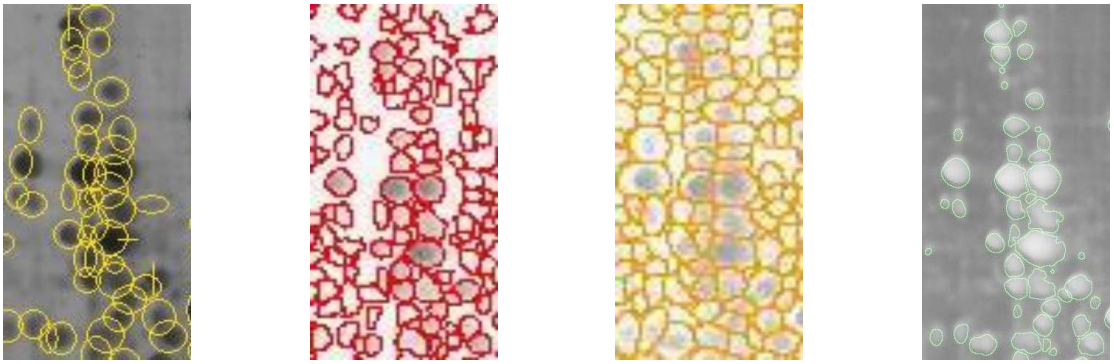

(a_1) (b_1) (c_1) (d_1)

Figure 6.16: Segmentation results obtained by the application of: (a) PDQuest 8.0.1, (b) Melanie 7, (c) Delta2D and (d) the presented segmentation scheme, whereas (a_1)-(d_1) are sub-images of the same region of (a)-(d) respectively.

It is evident that, the presented segmentation scheme results in more plausible spot boundaries (*see Figure 6.16(d_1)*) than all three image analysis software packages. PDQuest 8.0.1 results in elliptical boundaries, which do not correspond to the irregular shape of the actual spot boundaries, whereas such elliptical boundaries tend to include background regions. In the cases of Melanie 7 and Delta2D, the obtained segmentation results suffer from over-segmentation and are subject to laborious, error-prone and time-consuming correction process by the expert biologists.

Synthetic *2D-GE* Images

In order to quantitatively evaluate the presented segmentation scheme, experiments were performed on the set of synthetic images generated by the synthetic *2D-GE* image generation software, developed by the Real-time Systems & Image Analysis Lab of our Department. Figure 6.17 illustrates an example of a synthetic *2D-GE* image, as well as the corresponding ground truth. Such a synthetic image is populated by approximately 200 spots, following beta distribution. As a result of trial-and-error experimentation, parameters *a* and *b* of the beta function were set to 4 and 3 respectively, resulting in spatial frequency of singlet and multiplet occurrence, which emulates real *2D-GE* images. Synthetic background emulates inhomogeneity, streaks and clutter, which characterize the background of real *2D-GE* images.

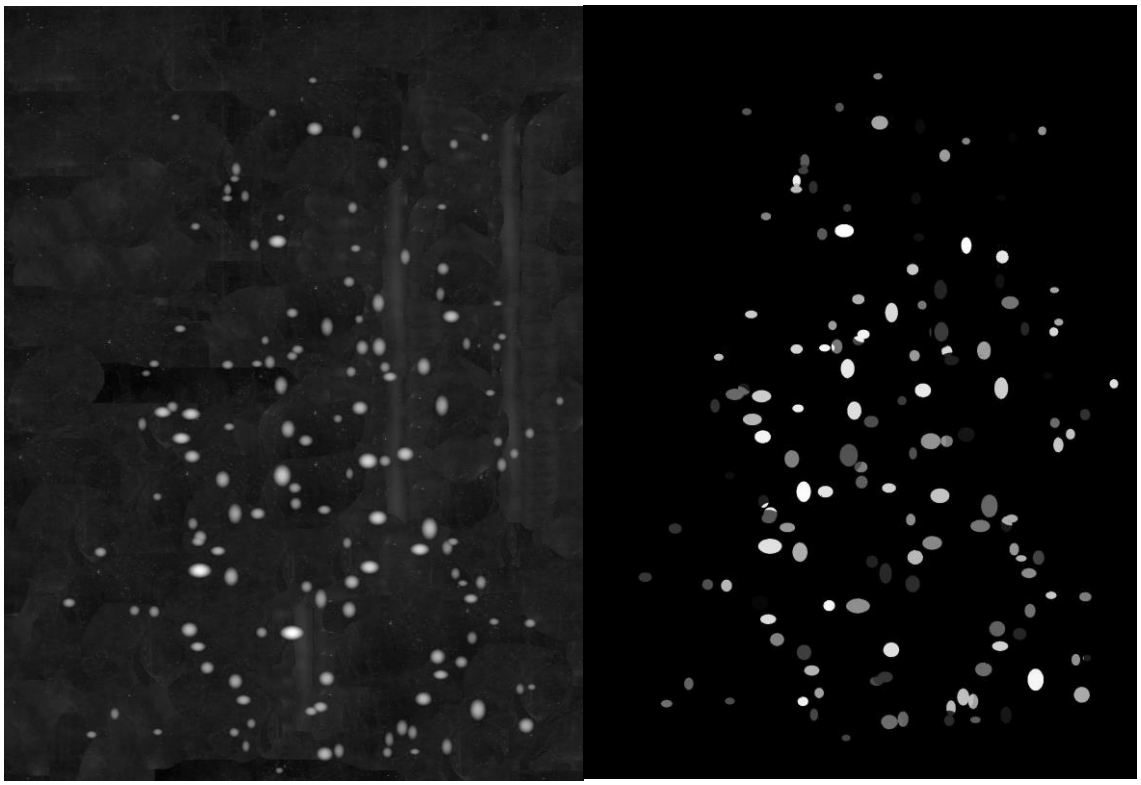

(a) (b)

Figure 6.17: (a) Synthetic *2D-GE* image and (b) the corresponding ground truth.

The intensity profile of each spot is chosen flat top in order to emulate the saturation characterizing actual protein spots and is defined by:

$$I(x,y)=\left\{\begin{array}{c} 1,\ r\le r_0 \\ \cos^2\left(\dfrac{r-r_0}{2\pi\sigma_\varphi}\right),\ r\le r_0+\sigma_\varphi \\ 0,\ otherwise \end{array}\right\} \tag{6.3.2}$$

where r_0 is the radius of the flat top, r is the Euclidean distance from the center of the spot and σ_φ^2 is an angle-dependent variance coefficient:

$$\sigma_\varphi^2=\frac{(r_0+\sigma_x)\cdot(r_0+\sigma_y)r}{\sqrt{(r_0+\sigma_x)^2\cdot(x-x_0)^2+(r_0+\sigma_y)^2\cdot(y-y_0)^2}}-r_0 \tag{6.3.3}$$

where σ_x and σ_y are the variance coefficients along the primary axes. Figure 6.18 illustrates example segmentation results obtained by PDQuest 8.0.1, Melanie 7, Delta2D and the presented segmentation scheme on a synthetic *2D-GE* image.

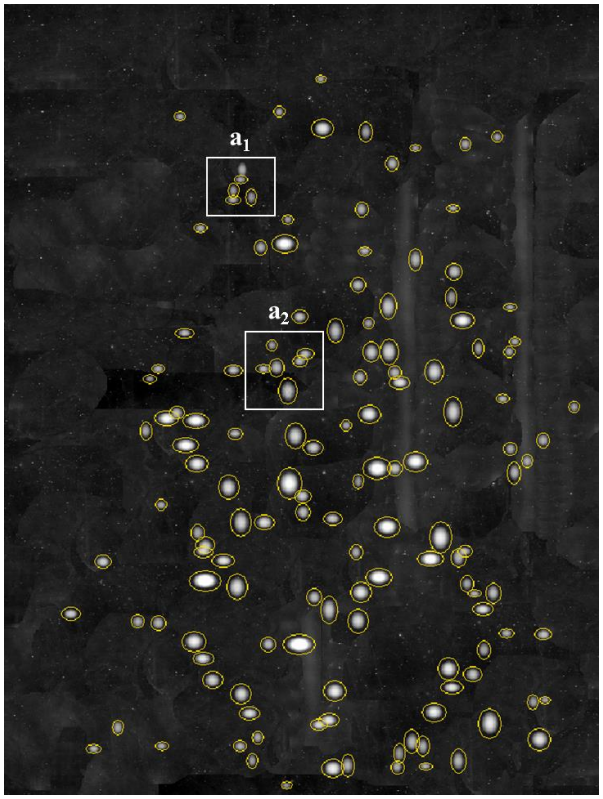

(a)

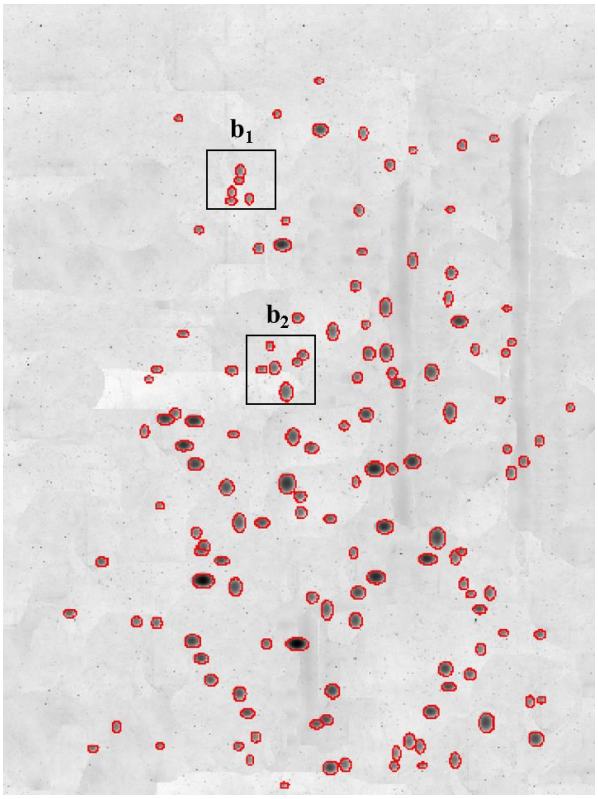

(b)

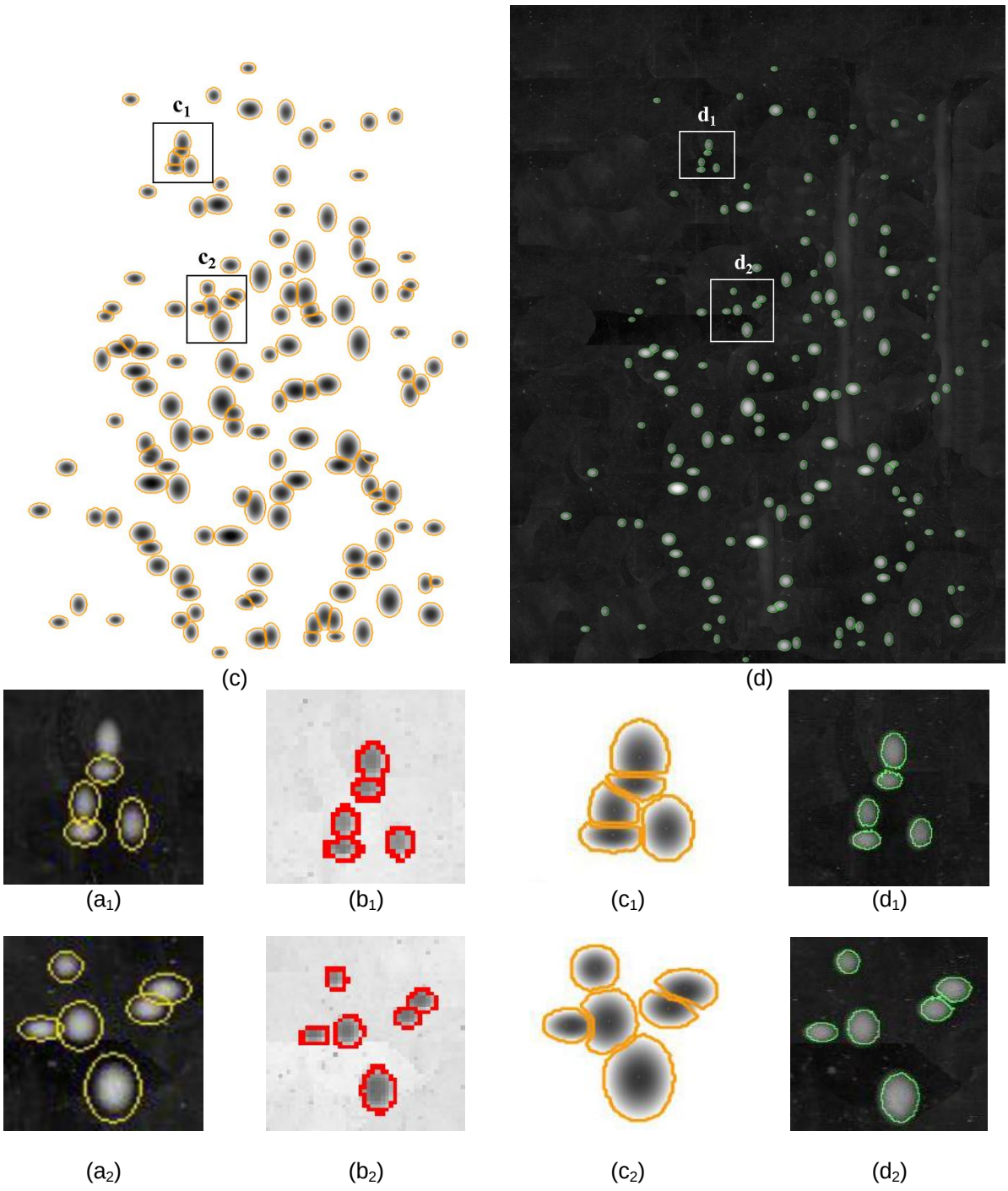

Figure 6.18: Segmentation results of the application of: (a) PDQuest 8.0.1, (b) Melanie 7, (c) Delta2D and (d) the presented segmentation scheme, (a_1)-(d_2) sub-images of (a)-(d), respectively.

The segmentation results are quantified according to the spot volume *V*, as defined in [108]:

$$V = \sum_{x,y \in Region} I(x,y) \tag{6.3.4}$$

Comparison of the segmentation results with the corresponding ground truth image, as generated by the *2D-GE* image simulation software allows the categorization of each pixel in one of the following four region types: “Actual Spot Region (*ASR*)”, “False Spot Region (*FSR*)”, “False Background Region (*FBR*)” and “Actual Background Region (*ABR*)”.

The spot volumes which are calculated according to Eq. (6.3.4) for the above four cases of regions, correspond to the “Actual Spot Volume” (*ASV*), “False Spot Volume” (*FSV*), “False Background Volume” (*FBV*) and “Actual Background Volume” (*ABV*), respectively. The segmentation performances are quantitatively evaluated in terms of Volumetric Overlap (*VO*) and Volumetric Error (*VE*), which are defined as follows:

$$VO = \frac{ASV}{ASV + FBV}, \quad VE = \frac{FSV}{ASV + FBV} \tag{6.3.5}$$

Table 6.4 presents the results obtained by PDQuest 8.0.1, Melanie 7, Delta2D and the presented segmentation scheme. Figure 6.19 provides a visualization of the results of Table 6.4. It is evident that, the presented scheme outperforms all three software packages in terms of *VO* and *VE*. In particular, *VE* obtained by the presented scheme is approximately 3 - 4 times smaller than the one obtained by the software packages, indicating that it is much more effective in avoiding the identification of *FSR*. Moreover, the presented scheme demonstrates a remarkably lower variance in both performance measures, as a result of its robustness over streaks, multiplets and faint spots.

Table 6.4: Segmentation results

	PDQuest 8.0.1	Melanie 7	Delta2D	Presented Scheme
VO	80.2±4.6%	86.5±3.2%	82.4±3.6%	92.0±1.2%
VE	83.1±8.9%	55.0±6.7%	64.3±7.6%	20.0±3.2%

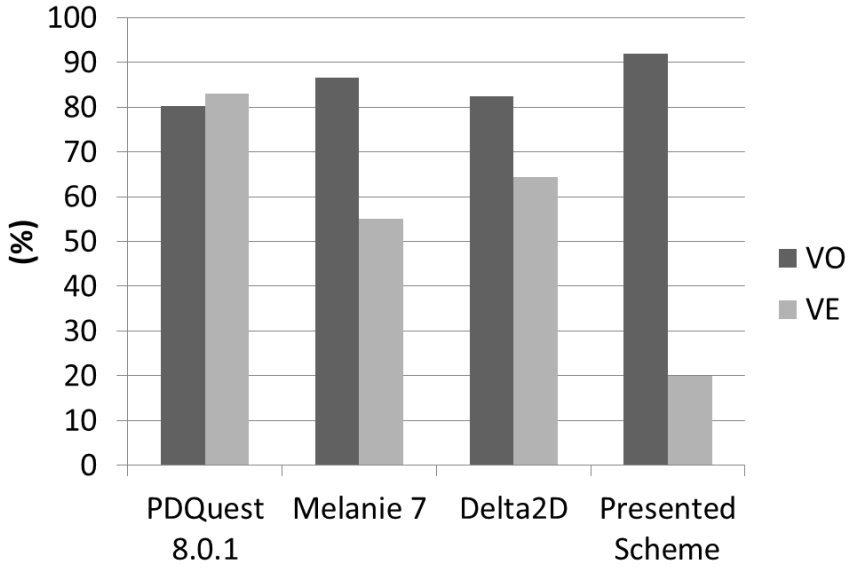

Figure 6.19: Overall segmentation results in terms of *VO* and *VE* obtained by PDQuest 8.0.1, Melanie 7, Delta2D and the presented scheme on the set of synthetic *2D-GE* images.

6.3.6 Graphical User Interface (*GUI*)

The presented *AC*-based model has been integrated into a *GUI* built in Matlab via GUIDE tools. The *GUI* is designed for spot detection and spot segmentation on *2D-GE* images. User intervention requirements are minimal. The *GUI* is designed in a simple yet effective manner so that the user can easily communicate with the computer without having to worry on the intrinsic mechanisms.

GUI comprises three main pushbuttons namely: a) read image file, b) spot detection and c) spot segmentation. Additionally, it includes three axes one for each pushbutton so as to depict the image emerged from each procedure. Waiting bars and pop-up windows are also included for a better communication between the user and the computer. Moreover, *GUI* consists of buttons which

magnify and minimize the dimensions of the image, drag the image and show the coordinates of each image, enhancing the visualization of the detection and segmentation results by the user. Figure 6.20 illustrates: a) the *GUI* setup, b) a snapshot of *GUI* during spot detection, c) a snapshot of *GUI* during spot segmentation and d) detection and segmentation results.

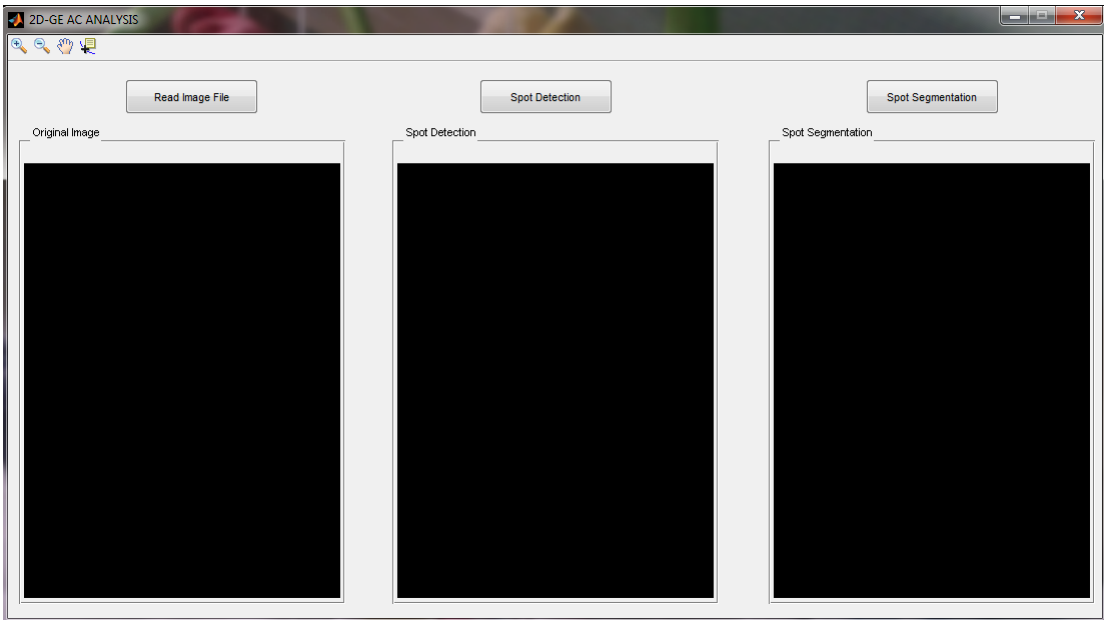

(a)

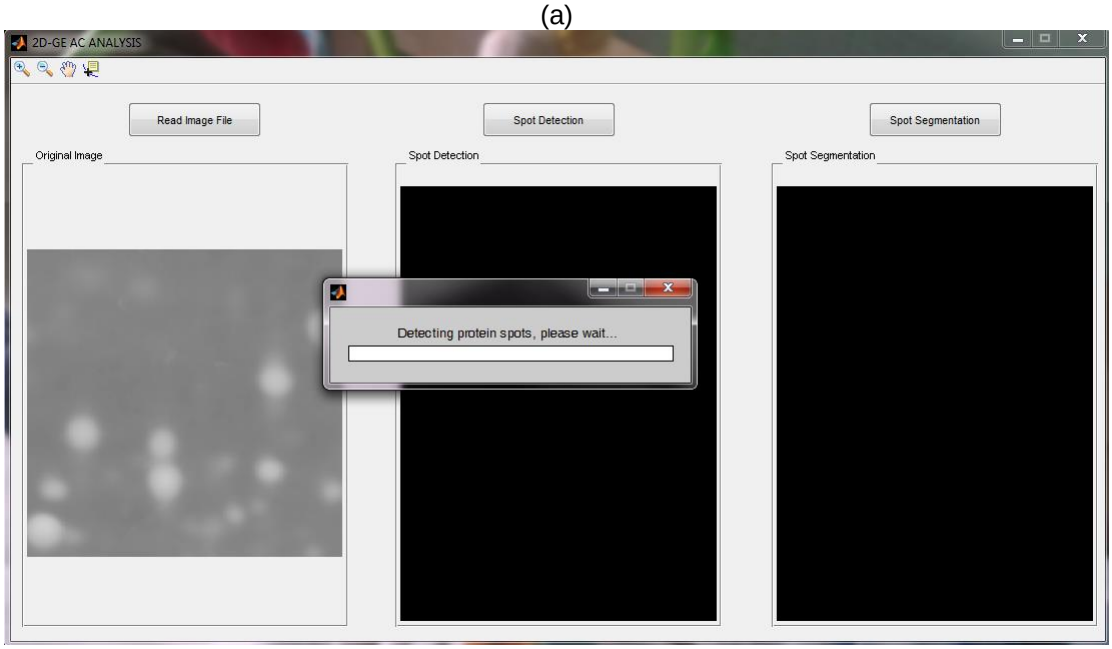

(b)

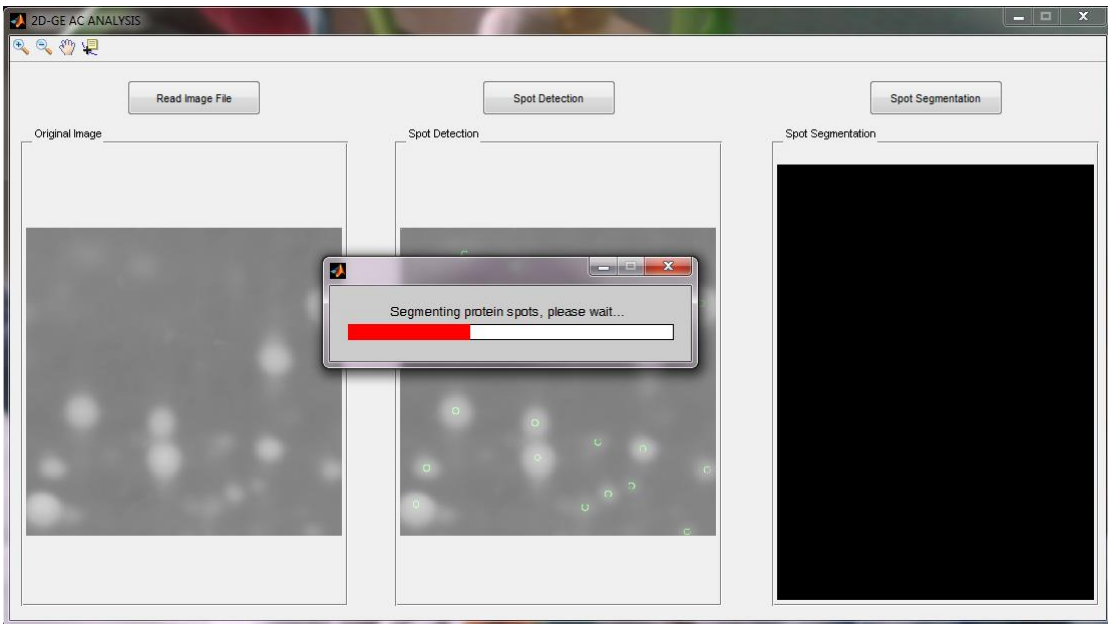

(c)

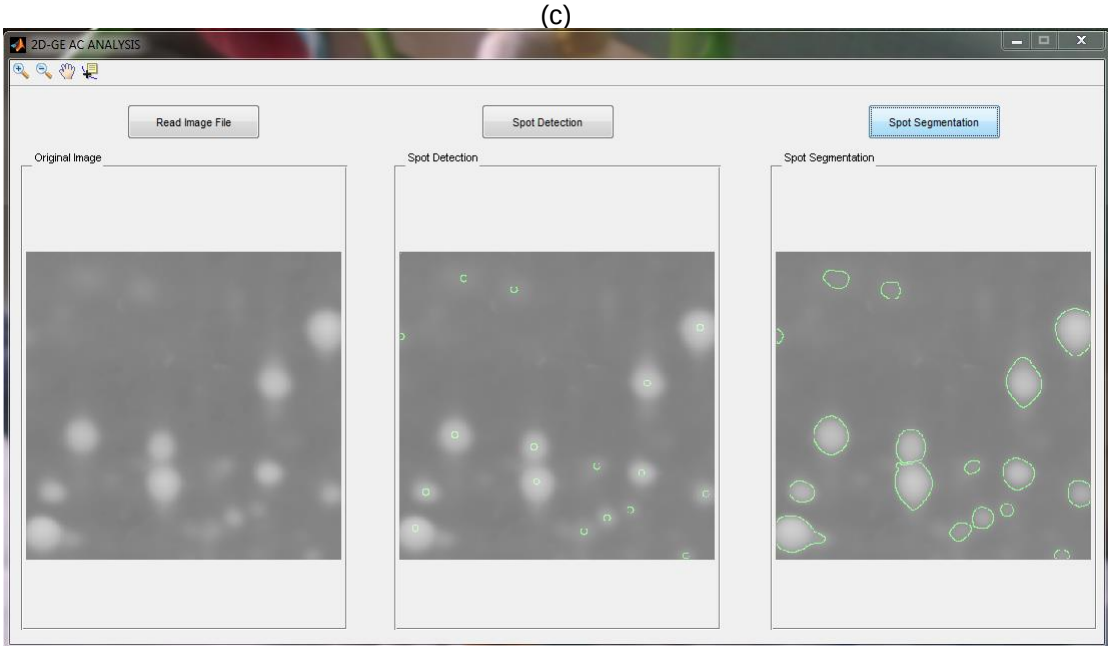

(d)

Figure 6.20: a) The *GUI* setup, b) a snapshot of *GUI* during spot detection, c) a snapshot of *GUI* during spot segmentation, d) detection and segmentation results.

6.3.7 Comparison Between Empirical and Automated *AC* Parameterization

The performance of the presented segmentation scheme has also been compared with the automated version implemented by embedding the framework presented in Chapter 3. Both automated and empirical versions are evaluated on real *2D-GE* images, obtained by the Biomedical Research Foundation of the Academy of Athens. For the empirical case, the optimal parameters are set according to the original paper [2]. For the presented framework, the

regularization and data fidelity parameters are automatically calculated according to Eq. (3.3.1).

Fig. 6.21 illustrates contours obtained on the second as well as on the final iteration for two *2D-GE* sub-images. Yellow color is used for the initial contour in both versions, whereas purple and green colors correspond to empirical and automated version, respectively. It is evident that, the segmentation results of the empirical and automated versions are comparable. Nonetheless, as already pointed out, empirical parameterization requires tedious, time-consuming experimentation. The presented framework is capable of obtaining *comparable results in an automated fashion*. Figure 6.22 depicts *DMI* for both versions, based on the contour evolution presented in Figure 6.21. Again in the case of the automated version, *DMI* is slightly higher in early iterations. In Figure 6.23, the comparison is performed in terms of *TC*, providing a quantification of the actual segmentation performance.

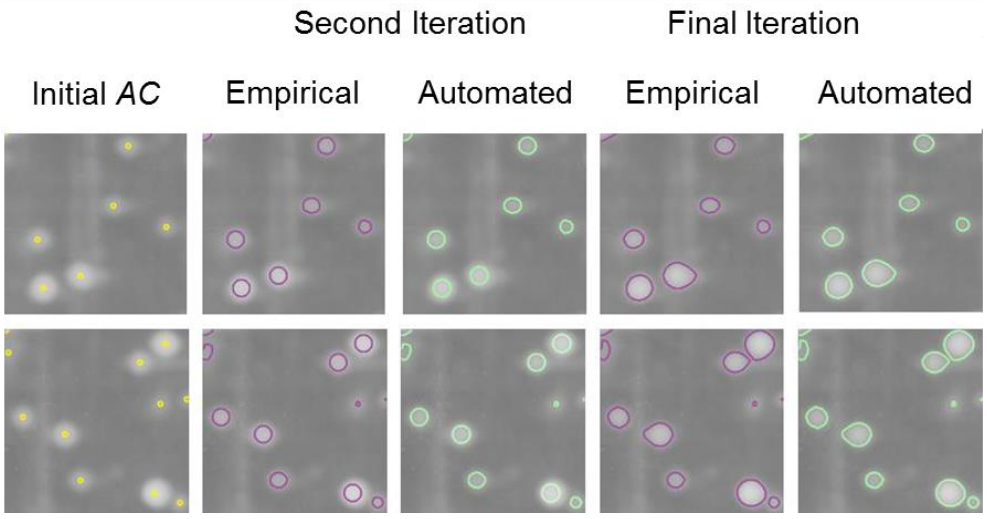

Figure 6.21: Segmentation results of the presented scheme on two sub-images. Yellow color is used for the initial contour in both versions, purple and green contours correspond to empirical and automated parameterization, respectively.

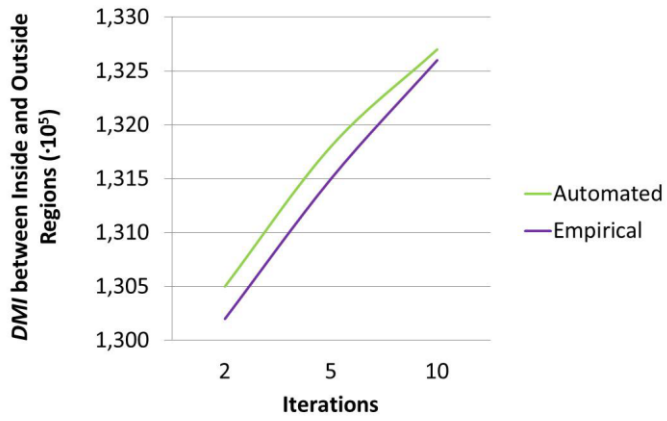

Figure 6.22: *DMI* between inside and outside regions for the early stages of evolution of automated versus empirical parameterization presented in Figure 6.21.

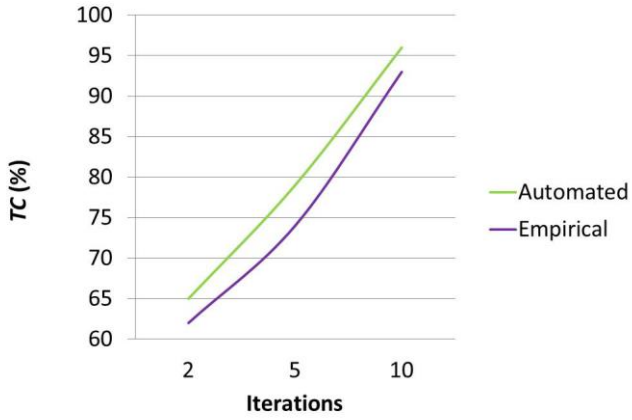

Figure 6.23: *TC* for the early stages of evolution of automated versus empirical approach presented in Figure 6.21.

6.4 Summary

In this chapter, a novel *AC*-based model is presented for the detection and segmentation of protein spots in *2D-GE* images. The presented detection technique utilizes the dilation operator for the location of regional intensity maxima associated with protein spots. The *SE* is selected as disk-shaped in accordance with the dominant roundish shape of most protein spots. The disk-shaped *SE* tends to ignore rectangular-shaped streaks. In addition, *SE* radius *R* is set considering that a certain radius value minimizes the detection of false negatives, whereas it allows the detection of local maxima associated with small spots even in cases where they overlap with larger spots in complex regions. The

presented detection technique imposes regional intensity constraints on the dilation-generated maxima so as to cope with the presence of noise and artifacts, such as cracks and dust particles.

Considering the experimental evaluation, the presented detection technique:

a) achieves a *PV* and a *DS* which exceed 90%,

b) outperforms Melanie 7 software package,

c) distinguishes multiple overlapping spots,

d) locates spots within streaks and,

e) ignores artifacts.

The presented segmentation scheme incorporates: (a) a detection process capable of identifying boundaries of spot overlap in regions occupied by multiplets, based on the observation that such boundaries are associated with local intensity minima, (b) histogram adaptation and morphological reconstruction so as to avoid unwanted amplifications of noise, streaks and facilitate the identification of faint spots, (c) a contour initialization process aiming to form a level-set surface initializing the subsequent contour evolution, based on the observation that protein spots are associated with regional intensity maxima and (d) a contour evolution process guided by region-based energy terms determined by image intensity as well as by information derived from the previous processes of the presented scheme.

The experimental evaluation of the presented segmentation scheme has been conducted on datasets of both real and synthetic *2D-GE* images, so as to facilitate quantitative comparisons with state-of-the-art *2D-GE* image analysis software packages, including PDQuest 8.0.1, Melanie 7 and Delta2D. As it can be derived by the experimental results, the presented scheme: (a) is capable of identifying spot boundaries within regions occupied by multiplets, (b) is capable of identifying boundaries of faint spots, (c) copes with the presence of noise, as a result of the region-based formulation of the energy terms in contour evolution

equation, (d) results in more plausible spot boundaries than PDQuest 8.0.1, Melanie 7 and Delta2D *2D-GE* image analysis software packages as it can be observed on the segmentation results on both real and synthetic *2D-GE* images, (e) outperforms all three 2D-GE image analysis software packages in terms of segmentation quantity measures, calculated from the segmentation results obtained on synthetic *2D-GE* images and (f) is unsupervised, providing an alternate to the laborious, error-prone and time-consuming process of manual editing, which is required in state-of-the-art *2D-GE* image analysis software packages.

CHAPTER 7

7. CONCLUSIONS

7.1 Contributions

In this thesis, unsupervised image analysis algorithms have been presented for the detection and segmentation of various types of images focusing on proteomics and medical images. After reviewing related state-of-the-art methods, novel algorithms, published in peer-reviewed international journals and international conferences, were introduced.

The major achievements of this thesis are listed below:

The presented framework for automated adjustment of region-based *AC* parameters described in Chapters 3 and 5 was compared to the empirical fine-tuned version and achieved to:

1) maintain a high segmentation quality comparable to the one stemmed from each empirically fine-tuned approach.
2) speed up contour convergence by selectively amplifying data fidelity forces.
3) identify and distinguish actual region boundaries from edge regions associated with noise and artifacts by utilizing multi-scale analysis and orientation coherence information.
4) enrich segmentation results with objectivity and reproducibility.
5) relieve domain users from the tedious and time-consuming process of empirical adjustment.
6) be equally successful when integrated into various region-based *AC* variations since it is implemented in a simple and flexible manner.
7) be successfully applied on several types of images such as natural, textured and biomedical images.

In the case of medical image segmentation, it achieved to remain insensitive on alterations in the settings of the acquisition devices and additional technical skills by the *MDs* are no longer a prerequisite.

The presented model for the detection and segmentation of proteomics images described in Chapter 6 achieved to:

1) separate multiplets in complex regions based on local intensity minima with respect to their directionalities.
2) identify boundaries of faint spots by utilizing *CLAHE* and *MM*.
3) tackle the presence of noise and the inhomogeneous background, as a result of the region-based formulation of the energy terms in contour evolution equation.
4) locate spots within streaks by appropriately selecting a disk-shaped *SE*, which tends to ignore the rectangular-shaped streaks.
5) ignore artifacts as a result of regional intensity constraints imposed on the detection of regional maxima.
6) obtain *PV* and *DS* values which exceed 90%.
7) endow detection and segmentation results with objectivity and reproducibility by automatically initializing the level set function based on regional intensity maxima associated with actual spots.
8) generate more plausible spot boundaries than commercial image analysis software packages such as: PDQuest 8.0.1, Melanie 7 and Delta2D.
9) outperform image analysis software packages in terms of *VO* and *VE* segmentation quality measures.
10) provide an alternate to the laborious, error-prone and time-consuming process of manual editing, which is required by gel analysis experts in state-of-the-art *2D-GE* software packages.

7.2 Future Perspectives

Recently, there has been an increasing interest to analyze and process images emerging from 3D scanners and 3D acquisition devices. Hence, one future direction of this work would be to investigate active surfaces, which are the three-dimensional representation of two-dimensional *ACs* [164]-[166]. In the case of volumetric medical imaging, active surfaces are very popular since they accurately delineate the required target region and aid *MDs* to better visualize complex and variable anatomical structures for diagnosis and treatment planning [167]. Figure 7.1 illustrates: (a) the initialization of an active contour surface, (b) the segmentation result of the trachea on a typical *CT* image [168].

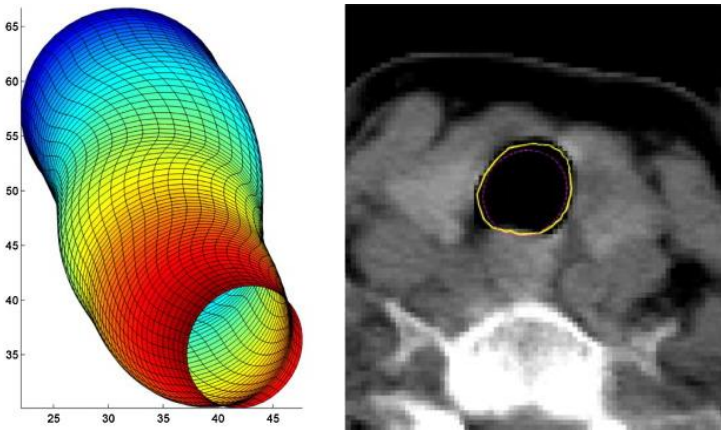

(a) (b)

Figure 7.1: (a) Initialization of an active contour surface, (b) segmentation result of the trachea on a typical *CT* image [168].

Moreover, in the case of the challenging issue of *AC* parameterization, machine learning algorithms have great potential for automation [169]. The key idea is to construct a 'level learning set' whose parameters will obtain values according to the orientation coherence in edge regions. More specific, the level learning set will be trained to learn to distinguish between structured and unstructured edge regions. After the learning process, it will be capable of amplifying and attenuating data fidelity forces in cases of unstructured and structured edge regions, respectively.

ABBREVIATIONS– ACRONYMS

2D-GE	Two-Dimensional Gel Electrophoresis
AC	Active Contour
AG	Attached Gingiva
ABR	Actual Background Region
ABV	Actual Background Volume
ASR	Actual Spot Region
ASV	Actual Spot Volume
ALOI	Amsterdam Library of Object Images (database)
ANOVA	Analysis of Variance
BCC	Basal Cell Carcinoma
^{14}C	Formaldehyde
CT	Computed Tomography
CTr	Contourlet Transform
COPD	Chronic Obstructive Pulmonary Disease
CLAHE	Contrast Limited Adaptive Histogram Equalization
DS	Detection Sensitivity
DFB	Directional Filter Bank
DMI	Difference of Mean Intensity
DNA	Deoxyribo-Nucleic Acid
FG	Free Gingiva
FN	False Negatives
FP	False Positives
FBR	False Background Region
FBV	False Background Volume
FSR	False Spot Region
FSV	False Spot Volume
GAC	Geodesic Active Contour
GUI	Graphical User Interface
HUPO	Human Proteome Organization
IPG	Immobilized pH Gradient
LP	Laplacian Pyramid

LoG_{σ}	Laplacian of Gaussian
LTG	Labial Teeth and Gingiva
LIDC - IDRI	Lung Image Dataset Consortium Image Collection (database)
MD	Medical Doctor
MM	Mathematical Morphology
MS	Mass Spectrometry
Mw	Molecular weight
MRI	Magnetic Resonance Imaging
MIAS	Mammographic Image Analysis Society (database)
mRNA	Messenger Ribo-Nucleic Acid
NSCLC	Non-Small Cell Lung Carcinoma
OE	Orientation Entropy
pI	Isoelectric Point
PV	Predictive Value
PDE	Partial Differential Equation
PTMs	Post-Translational Modifications
RNA	Ribo-Nucleic Acid
^{35}S	Methionine
SE	Structuring Element
SP	Specificity
SDS	Sodium Dodecyl Sulfate
SCC	Squamous Cell Carcinoma
SCLC	Small Cell Lung Carcinoma
T3	Triiodothyronine
T4	Thyroxine
TC	Tannimoto Coefficient
TN	True Negatives
TP	True Positives
tRNA	Transfer Ribo-Nucleic Acid
US	Ultrasound
VE	Volumetric Error
VO	Volumetric Overlap
WST	Watersheds Transform

APPENDIX I

I. Gradient Descent Algorithm

Let θ be an unknown parameter vector and $J(\theta)$ the corresponding cost function to be minimized, which is assumed to be differentiable.

The algorithm starts with an initial estimate $\theta(0)$ of the minimum point and the subsequent algorithmic iterations are defined as follows [158]:

$$\theta(new) = \theta(old) + \Delta\theta \tag{I.1}$$

$$\Delta\theta = -\mu \frac{\partial J(\theta)}{\partial \theta} \Big|_{\theta=\theta(old)} \tag{I.2}$$

where $\mu > 0$. Figure I.1 demonstrates the geometric interpretation of the algorithm. The new estimate $\theta(new)$ is selected in the direction that decreases $J(\theta)$. Parameter μ plays a key role in the convergence of the algorithm. Provided that μ is too small, corrections $\Delta(\theta)$ are also small and the convergence to the optimum point is slow. However, if μ is large, the algorithm may oscillate around the optimum point and convergence may not be achieved. Once μ is properly chosen, the algorithm converges to a stationary point of $J(\theta)$, which can be: a) a local minimum (θ_1^0), b) a global minimum (θ^0) and c) a saddle point (θ_2^0). In either case, the gradient of the stationary point is zero (Figure I.2). To which of the stationary points the algorithm will converge depends on the position of the initial point relative to the stationary points. Furthermore, the convergence speed depends on the form of $J(\theta)$. Figure I.3 shows the constant $J(\theta)$ = c curves, for two cases and for different values of c in 2D space where $\theta = [\theta_1, \theta_2]^T$. The optimum θ^0 is located at the center of the curves. The gradient $\frac{\partial J(\theta)}{\partial \theta}$ is always vertical to the tangent to the constant J curves. Indeed, if $J(\theta) = c$, then:

$$dc = 0 = \frac{\partial J(\theta)^{\mathrm{T}}}{\partial \theta} d\theta \Rightarrow \frac{J(\theta)}{\partial \theta} \perp d\theta \tag{I.3}$$

Moreover, at each point θ on a curve $J(\theta)$ = c, the gradient $\frac{\partial J(\theta)}{\partial \theta}$ points to the direction of the maximum increase of $J(\theta)$. This can be seen by the following:

$$dJ = \frac{\partial J(\theta)^{\mathrm{T}}}{\partial \theta} d\theta = \left| \frac{\partial J(\theta)}{\partial \theta} \right| \| d\theta | \cos\varphi \tag{I.4}$$

where $\cos\varphi$ is maximum for $\varphi = 0$, i.e. when two involved vectors are parallel. Hence, $\frac{\partial J(\theta)}{\partial \theta}$ always points to the direction of the maximum increase of $J(\theta)$. In the case of Figure I.3(a), the negative gradient points to the optimum point. In such cases convergence can be achieved in a single step. In the case of Figure I.3(b), $\Delta\theta$ points to the center at only very few places. Therefore, convergence in such cases is slow and $\Delta\theta$ can oscillate back and forth following a zigzag path until it rests at the optimum point [158].

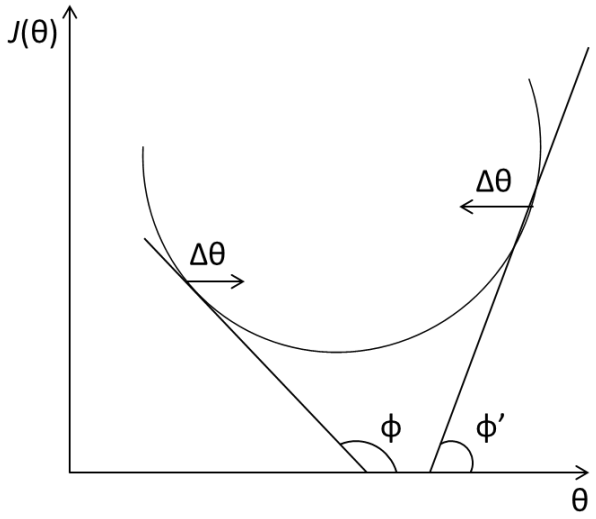

Figure I.1: In the gradient descent algorithm, the correction of the parameters takes place in the direction which decreases the value of the cost function.

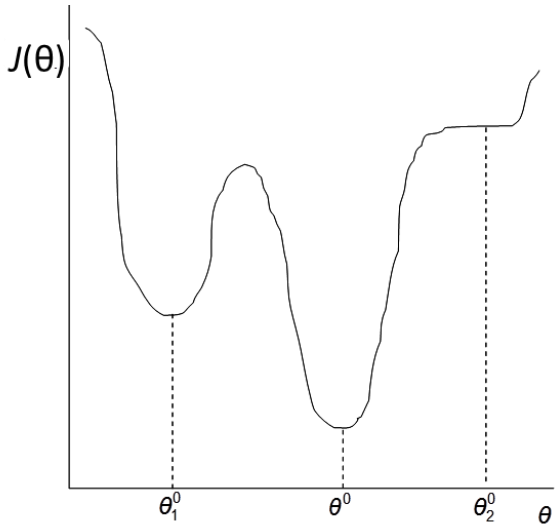

Figure I.2: A local minimum (θ_1^0), a global minimum (θ^0) and a saddle point (θ_2^0) of *J(θ)*.

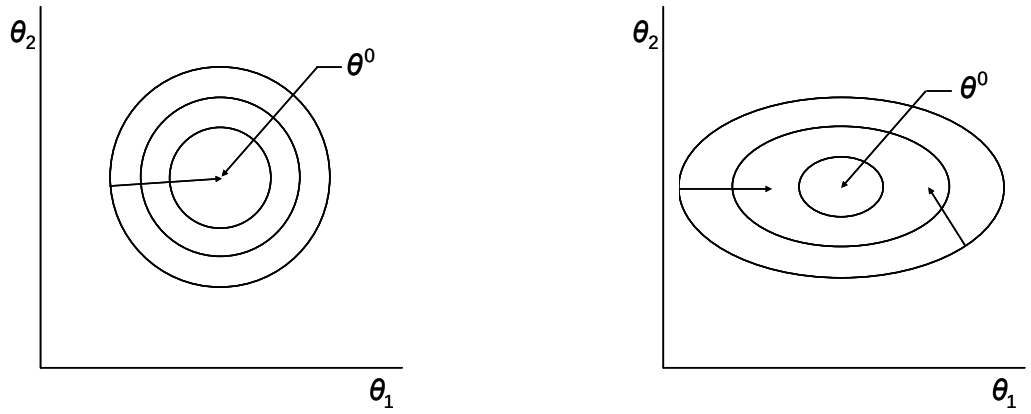

(a) (b)

Figure I.3: Curves of constant cost values, a) the negative gradient always points to the optimum, b) the negative gradient points to the optimum at a few places and convergence is slow.

BIBLIOGRAPHY

[1] P. Arbelaez, M. Maire, C. Fowlkes and J. Malik, “Contour Detection and Hierarchical Image Segmentation,” *IEEE Trans. Patt. Anal. Mach. Intell.,* vol. 33, no. 5, 2011, pp. 898-916.
http://www.eecs.berkeley.edu/Research/Projects/CS/vision/bsds.

[2] T.F. Chan and L.A. Vese, “Active Contours Without Edges,” *IEEE Trans. Im. Proc*., vol. 10, no. 2, 2001, pp. 266-277.

[3] Y. Saraf. *Algorithms for Image Segmentation*. Doctoral Dissertation, Birla Institute of Technology and Science, Pilani, Rajasthan, India, 2006.

[4] M. Kamel and A. Zhao, ‘‘Extraction of Binary Character/Graphics Images from Grayscale Document Images,’’ *Graph. Mod. Im. Proc.*, vol. 55, no. 3, 1993, pp. 203–217.

[5] B. Bhanu, ‘‘Automatic Target Recognition: State of the Art Survey,’’ *IEEE Trans. Aerosp. Electron. Syst.*, vol. 22, 1986, pp. 364–379.

[6] M. Sezgin, and R. Tasaltin, ‘‘A New Dichotomization Technique to Multilevel Thresholding Devoted to Inspection Applications,’’ *Patt. Rec. Lett.*, vol. 21, 2000, pp. 151–161.

[7] M.E. Sieracki, S.E. Reichenbach, and K.L. Webb, ‘‘Evaluation of Automated Threshold Selection Methods for Accurately Sizing Microscopic Fluorescent Cells by Image Analysis,’’ *Appl. Envir. Microbiol.*, vol. 55, 1989, pp. 2762–2772.

[8] L.U. Wu, M.A. Songde, and L.U. Hanqing, ‘‘An Effective Entropic Thresholding for Ultrasonic Imaging,’’ *Proc. Int. Conf. Patt. Rec. (ICPR)*, 1998, pp. 1522–1524.

[9] J.S. Chang, H.Y.M. Liao, M.K. Hor, J. W. Hsieh, and M. Y. Chern, ‘‘New Automatic Multi-Level Thresholding Technique for Segmentation of Thermal Images,’’ *Im. Vis. Comp.*, vol. 15, 1997, pp. 23–34.

[10] W. Oh, and B. Lindquist, ‘‘Image Thresholding by Indicator Kriging,’’ *IEEE Trans. Patt. Anal. Mach. Intell.*, vol. 21, 1999, pp. 590–602.

[11] T. Srikanthan, and K.V. Asari, ‘‘Automatic Segmentation Algorithm for the Extraction of Lumen Region and Boundary from Endoscopic Images,’’ *Med. Biol. Eng. Comp.*, vol. 39, no.1, 2001, pp. 8–14.

[12] M. Sezgin and B. Sankur, “Survey Over Image Thresholding Techniques and Quantitative Performance Evaluation,” *J. of Elect. Im*., vol. 13, no. 1, 2004, pp. 146-165.

[13] A. Rosenfeld, and P. De la Torre, ‘‘Histogram Concavity Analysis as an Aid in Threshold Selection,’’ *IEEE Trans. Syst. Man Cyber.*, vol. 13, 1983, pp. 231–235.

[14] J. Weszka, and A. Rosenfeld, ‘‘Histogram Modification for Threshold Selection,’’ *IEEE Trans. Syst. Man Cyber.*, vol. 9, 1979, pp. 38–52.

[15] L. Halada, and G.A. Osokov, ‘‘Histogram Concavity Analysis by Quasicurvature,’’ *Comp. Artif. Intell.*, vol. 6, 1987, pp. 523–533.

[16] S.C. Sahasrabudhe, and K.S.D. Gupta, ‘‘A Valley-Seeking Threshold Selection Technique,’’ *Comp. Vis. Im. Und.*, vol. 56, 1992, pp. 55–65.

[17] R.J. Whatmough, ‘‘Automatic Threshold Selection from a Histogram Using the Exponential Hull,’’ *Graph. Mod. Im. Proc.*, vol. 53, 1991, pp. 592–600.

[18] M.I. Sezan, ‘‘A Peak Detection Algorithm and its Application to Histogram-Based Image Data Reduction,’’ *Graph. Models Im. Proc.*, vol. 29, 1985, pp. 47–59.

[19] T.W. Ridler, and S. Calvard, ‘‘Picture Thresholding Using an Iterative Selection Method,’’ *IEEE Trans. Syst. Man Cyber.*, vol. 8, 1978, pp. 630–632.

[20] C.K. Leung, and F.K. Lam, ‘‘Performance Analysis of a Class of Iterative Image Thresholding Algorithms,’’ *Patt. Rec.*, vol. 29, no. 9, 1996, pp. 1523–1530.

[21] H.J. Trussel, ‘‘Comments on Picture Thresholding Using Iterative Selection Method,’’ *IEEE Trans. Syst. Man Cyber.*, vol. 9, 1979, pp. 311.

[22] M.K. Yanni and E. Horne, ‘‘A New Approach to Dynamic Thresholding,’’ *Proc. Eur. Conf. Sig. Proc. (EUSIPCO)*, vol. 1, 1994, pp. 34–44.

[23] N. Otsu, ‘‘A Threshold Selection Method from Gray Level Histograms,’’ *IEEE Trans. Syst. Man Cyber.*, vol. 9, 1979, pp. 62–66.

[24] J.N. Kapur, P.K. Sahoo, and A.K.C. Wong, ‘‘A New Method for Gray-Level Picture Thresholding Using the Entropy of the Histogram,’’ *Graph. Mod. Im. Proc.*, vol. 29, 1985, pp. 273–285.

[25] J.C. Yen, F.J. Chang, and S. Chang, ‘‘A New Criterion for Automatic Multilevel Thresholding,’’ *IEEE Trans. Im. Proc.*, vol. 4, 1995, pp. 370–378.

[26] P. Sahoo, C. Wilkins, and J. Yeager, ‘‘Threshold Selection Using Renyi’s Entropy,’’ *Patt. Rec.*, vol. 30, 1997, pp. 71–84.

[27] N.R. Pal, and S.K. Pal, ‘‘Entropic Thresholding,’’ *Sig. Proc.*, vol. 16, 1989, pp. 97–108.

[28] C. Chang, K. Chen, J. Wang, and M.L.G. Althouse, ‘‘A Relative Entropy Based Approach in Image Thresholding,’’ *Patt. Rec.*, vol. 27, 1994, pp. 1275–1289.

[29] W. Niblack, *An Introduction to Image Processing*, Prentice-Hall, 1986.

[30] O.D. Trier, and A.K. Jain, ‘‘Goal-Directed Evaluation of Binarization Methods,’’ *IEEE Trans. Patt. Anal. Mach. Intell.*, vol. 17, 1995, pp. 1191–1201.

[31] J.M. White, and G.D. Rohrer, ‘‘Image Thresholding for Optical Character Recognition and Other Applications Requiring Character Image Extraction,’’ *IBM J. Res. Dev.*, vol. 27, no. 4, 1983, pp. 400–411.

[32] J.M.S. Prewitt. *Object Enhancement and Extraction*. Picture Processing and Psychopictorics, B.S. Lipkin, and A. Rosenfeld (eds.), Academic Press, 1970.

[33] I.E. Sobel, *Camera Models and Machine Perception*, PhD Thesis, Stanford University, Palo Alto, CA, USA, 1970.

[34] L.S. Davis, “A Survey of Edge Detection Techniques,” *Comp. Graph. Im. Proc.*, vol. 4, no. 3, 1975, pp. 248-260.

[35] R. Kumar and A.M. Arthanariee, “A Comparative Study of Image Segmentation Using Edge-Based Approach,” *Int. J. Math. Sci.*, vol. 7, no. 3, 2013, pp. 784-788.

[36] L. Vincent and P. Soille, "Watersheds in Digital Spaces: an Efficient Algorithm Based on Immersion Simulations," *IEEE Trans. Patt. Anal. Mach. Intell.*, vol. 13, 1991, pp. 583-598.

[37] Y. Hu and T. Nagao, “A Template Matching Method Based on Marker-Controlled Watershed Segmentation,” *IEICE Trans. Inf. Sys*., vol. E87-D, no. 10, 2004, pp. 2389-2398.

[38] A. Bleau and L.J. Leon, “Watershed-Based Segmentation and Region Merging,” *Comp. Vis. Im. Und.,* vol. 77, no. 3, 2000, pp. 317-370.

[39] M. Kass, A. Witkin and D. Terzopoulos, “Snakes: Active Contour Models,” *Int. J. Comp. Vis*., vol. 1, no. 4, 1988, pp. 321-331.

[40] S. Osher and J. Sethian, “Fronts Propagating with Curvature-Dependent Speed: Algorithms Based on the Hamilton-Jacobi Formulation,” *J. Comp. Phys.*, vol. 79, no. 1, 1988, pp. 12-49.

[41] V. Caselles, F. Catté, T. Coll and F. Dibos, “A Geometric Model for Active Contours in Image Processing,” *Num. Math*., vol. 66, no. 1, 1994, pp. 1-31.

[42] V. Caselles, R. Kimmel and G. Sapiro, “Geodesic Active Contours,” *Proc. IEEE Int. Conf. Comp. Vis. (ICCV)*, 1995, pp. 694-699.

[43] C. Li, C. Xu, C. Gui and M.D. Fox, “Distance Regularized Level Set Evolution and Its Application to Image Segmentation,” *IEEE Trans. Im. Proc*., vol. 19, no. 12, 2010, pp. 3243-3254.

[44] S. Kichenassamy, A. Kumar, P. Olver, A. Tannenbaum and A. Yezzi, “Gradient Flows and Geometric Active Contour Models,” *Proc. IEEE Int. Conf. Comp. Vis. (ICCV),* 1995, pp. 810-815.

[45] R. Malladi, J.A. Sethian and B.C. Vemuri, “Shape Modeling with Front Propagation: A Level Set Approach,” *IEEE Trans. Patt. Anal. Mach. Intel.*, vol. 17, no. 2, 1995, pp. 158-175.

[46] N. Paragios and R. Deriche, “Geodesic Active Contours and Level Sets for the Detection and Tracking of Moving Objects,” *IEEE Trans. Patt. Anal. Mach. Intel.,*, vol. 22, no. 3, 2000, pp. 266-280.

[47] M. Leventon, W. Grimson and O. Faugeras, “Statistical Shape Influence in Geodesic Active Contours,” *Proc. IEEE Comp. Vis. Patt. Rec. (CVPR),* vol. 1, 2000, pp. 316-323.

[48] A. Vasilevskiy and Siddiqi, “Flux Maximizing Geometric Flows,” *IEEE Trans. Patt. Anal. Mach. Intel.*, vol. 24, no. 12, 2001, pp. 1565-1578.

[49] N. Paragios, O. Mellina-Gottardo and V. Ramesh, “Gradient Vector Flow Fast Geometric Active Contours,” *IEEE Trans. Patt. Anal. Mach. Intel*., vol. 26, no. 3, 2004, pp. 402-407.

[50] C. Li, C. Xu, C. Gui and M.D. Fox, “Level Set Evolution Without Reinitialization: A New Variational Formulation,” *Proc. IEEE Comp. Vis. Patt. Rec. (CVPR),* vol. 1, 2005, pp. 430-436.

[51] X. Xie and M. Mirmehdi, “MAC: Magnetostatic Active Contour Model,” *IEEE Trans. Patt. Anal. Mach. Intel.,* vol. 30, no. 4, 2008, pp. 632-646.

[52] D. Mumford and J. Shah, “Optimal Approximation by Piece-wise Smooth Functions and Associated Variational Problems,” *Comm. Pure Appl. Math*., vol. 42, 1989, pp. 577-685.

[53] X. Bresson, S. Esedoglu, P. Vandergheynst, J. Thiran and S. Osher, “Fast Global Minimization of the Active Contour/Snake Model,” *J. Math. Im. Vis*., vol. 28, no. 2, 2007, pp. 151-167.

[54] A. Tsai, A. Yezzi and A.S. Willsky, “Curve Evolution Implementation of the Mumford-Shah Functional for Image Segmentation, Denoising, Interpolation and Magnification,” *IEEE Trans. Im. Proc*., vol. 10, no. 8, 2001, pp. 1169-1186.

[55] L.A. Vese and T.F. Chan, “A Multiphase Level Set Framework for Image Segmentation Using the Mumford and Shah Model,” *Int. J. Comp. Vis*., vol. 50, no. 3, 2002, pp. 271-293.

[56] T. Brox and D. Cremers, “On Local Region Models and a Statistical Interpretation of the Piecewise Smooth Mumford-Shah Functional,” *Int. J. Comp. Vis*., vol. 84, no. 2, 2009, pp. 184-193.

[57] E. Strekalovskiy, A. Chambolle, D. Cremers, “A Convex Representation for the Vectorial Mumford-Shah Functional,” *Proc. IEEE Comp. Vis. Pat. Rec. (CVPR),* 2012.

[58] H. Xiao, Y. Li, J. Du and A. Mosig, “Ct3d: Tracking Microglia Motility in 3D Using a Novel Cosegmentation Approach,” *Bioinformatics*, vol. 28, no. 4, 2011, pp. 564-571.

[59] C. Pluempitiwiriyawej, J.M.F. Moura, Y.J.L. Wu and C. Ho, “STACS: New Active Contour Scheme for Cardiac MR Image Segmentation,” *IEEE Trans. Med. Imag.,* vol. 24, no. 5, pp. 593-603, 2005.

[60] A. Tsai, A. Yezzi, W. Wells, C. Tempany, D. Tucker, A. Fan, W.E. Grimson and A. Willsky, “A Shape-Based Approach to the Segmentation of Medical Imagery Using Level Sets*,” IEEE Trans. Med. Imag*., vol. 22, no. 2, 2003, pp. 137-154.

[61] I. Kokkinos, G. Evangelopoulos and P. Maragos, “Texture Analysis and Segmentation Using Modulation Features, Generative Models and Weighted Curve Evolution,” *IEEE Trans. Patt. Anal. Mach. Intel.,* vol. 31, no. 1, 2009, pp. 142-157.

[62] M. Keuper, T. Schmidt, J. Padeken, P. Heun, K. Palme, H. Burkhardt and O. Ronneberger, “3D Deformable Surfaces with Locally Self-Adjusting Parameters – A Robust Method to Determine Cell Nucleus Shapes,” *Proc. IEEE Int. Conf. Patt. Rec. (ICPR),* 2010, pp. 2254-2257.

[63] X. Liu, Y.M. Cheung, M. Li and H. Liu, “A Lip Extraction Method Using Localized Active Contour Model with Automatic Parameter Selection,” *Proc. IEEE Int. Conf. Patt. Rec. (ICPR),* 2010, pp. 4332-4335.

[64] D. Iakovidis, M. Savelonas, S. Karkanis and D. Maroulis, “A Genetically Optimized Level Set Approach to Segmentation of Thyroid Ultrasound Images,” *Appl. Intel.,* Springer – Verlag, vol. 27, no. 3, 2007, pp. 193-203.

[65] C.Y. Hsu, C.Y. Liu and C.M. Chen, “Automatic Segmentation of Liver PET Images,” *Comp. Med. Im. and Graph.,* vol. 32, 2008, pp. 601-610.

[66] M. Allili and D. Ziou, “An Approach for Dynamic Combination of Region and Boundary Information in Segmentation,” *Proc. IEEE Int. Conf. Patt. Rec. (ICPR),* 2008, pp. 1-4.

[67] P.A. Yushkevich, J. Piven, H. Cody, S. Ho, J.C. Gee and G. Gerig, “User-Guided Level Set Segmentation of Anatomical Structures with ITK – SNAP,” *ISC/NA-MIC/MICCAI Workshop on Open-Source Software*, 2005.

[68] D. Tschumperlé and R. Deriche, “Vector-Valued Image Regularization with PDEs: A Common Framework for Different Applications*,” IEEE Trans. Patt. Anal. Mach. Intel.,* vol. 27, no. 4, 2005, pp. 506-517.

[69] J. Weickert and H. Scharr, “A Scheme for Coherence-Enhancing Diffusion Filtering with Optimized Rotation Invariance,” *J. Vis. Comm. Im. Repres.,* vol. 13, no. (1-2), 2002, pp. 103-118.

[70] M.N. Do and M. Vetterli, “The Contourlet Transform: an Efficient Directional Multiresolution Image Representation,” *IEEE Trans. Im. Proc.,* vol. 14, no. 12, 2005, pp. 2091-2106.

[71] S. Katsigiannis, E. Keramidas and D. Maroulis, “A Contourlet Transform Feature Extraction Scheme for Ultrasound Thyroid Texture Classification,” *Eng. Intel. Sys. Artif. Intel. Appl. Inn.,* vol. 18, Issue ¾.2010

[72] M. Vetterli, “Multidimensional Subband Coding: Some Theory and Algorithms,” *IEEE Trans. Sign. Proc.*, vol. 6, no. 2, 1984, pp. 97-112.

[73] S. Theodoridis, A. Pikrakis, K. Koutroumbas and D. Cavouras. *Introduction to Pattern Recognition: A Matlab Approach*. Academic Press, 2010.

[74] C. Li, University of Connecticut, 2011,

http://www.engr.uconn.edu/~cmli/.

[75] X. Bresson, City University of Hong Kong, 2010,

http://www.cs.cityu.edu.hk/~xbresson/.

[76] D.D.-Y. Po and M.N. Do, "Directional Multiscale Modeling of Images Using the Contourlet Transform," *IEEE Trans. Im. Proc*., vol. 15, no. 6, 2006, pp. 1610-1620.

[77] A.K. Mishra, P.W. Fieguth and D.A. Clausi, "Decoupled Active Contour (*DAC*) for Boundary Detection," *IEEE Trans. Patt. Anal. Mach. Intel.*, vol. 33, no. 2, 2011, pp. 310-324.

[78] L. Bertelli, B. Sumengen, B.S. Manjunath and F. Gibou, "A Variational Framework for Multiregion Pairwise-Similarity-Based Image Segmentation," *IEEE Trans. Patt. Anal. Mach. Intel.,* vol. 30, no. 8, 2008, pp. 1400-1414.

[79] J.M. Geusebroek, G.J. Burghouts and A.W.M. Smeulders, "The Amsterdam Library of Object Images," *Int. J. Comp. Vis*., vol. 61, no. 1, 2005, pp. 103-112.

[80] W.R. Crum, O. Camara and D.L.G. Hill, "Generalized Overlap Measures for Evaluation and Validation in Medical Image Analysis," *IEEE Trans. Med. Im*., vol. 25, no. 11, 2006, pp. 1451-1461.

[81] http://world-2dpage.expasy.org/swiss-2dpage/

[82] http://prosite.expasy.org/

[83] B. Ren, F. Robert, J.J. Wyrick, O. Aparicio, E.G. Jennings, I. Simon, J. Zeitlinger, J. Schreiber, N. Hannett, E. Kanin, T.L. Volkert, C.J. Wilson, S.P. Bell and R.A. Young, "Genome-Wide Location and Function of DNA Binding Proteins," *Science*, vol. 290, no. 5500, 2000, pp. 2306-2309.

[84] J. Wisniak, "Jöns Jacob Berzelius A Guide to the Perplexed Chemist," *The Chemical Educator*, vol. 5, no. 6, 2000, pp. 343-350.

[85] P. Sudbery. *Human Molecular Genetics*. Prentice Hall, 2nd Ed., 2002.

[86] M.R. Wilkins, J.C. Sanchez, A.A. Gooley, R.D. Appel, I. Humphery-Smith, D.F. Hochstrasser and K.L. Williams, "Progress with Proteome Projects: Why All Proteins

Expressed by a Genome Should be Identified and How to Do It," *Biotechnol. Genet. Eng. Rev.,* vol. 13, 1996, pp. 19-50.

[87] W. Blackstock and M. Mann. *A Trends Guide to Proteomics*. Elsevier Science, 2001.

[88] S. Fields, "Proteomics. Proteomics in Genomeland," *Science*, vol. 291, 2001, pp. 1221-1224.

[89] J.H. Wang and R.M. Hewick, "Proteomics in Drug Discovery," *Drug Discovery Today*, vol. 4, no. 3, 1999, pp. 129-133.

[90] M.W. Duncan and S.W. Hunsucker, "Proteomics as a Tool for Clinically Relevant Biomarker Discovery and Validation," *Exp. Biol. Med*., vol. 230, 2005, pp. 808-17.

[91] P.H. O'Farrell, "High Resolution Two-Dimensional Electrophoresis of Proteins," *J. Biol. Chem.,* vol. 250, 1975, pp. 4007-21.

[92] A.W. Dowsey, M.J. Dunn and G.Z. Yang, "The Role of Bioinformatics in Two-Dimensional Gel Electrophoresis," *Proteomics*, vol. 3, no. 8, 2003, pp. 1567-1596.

[93] M. Berth, F.M. Moser, M. Kolbe and J. Bernhardt, "The State of the Art in the Analysis of Two-Dimensional Gel Electrophoresis Images," *Appl. Microb. Biotechnol.*,vol. 76, no. 6, 2007, pp. 1223-1243.

[94] R. Tonge, J. Shaw, B. Middleton, R. Rowlinson, S. Rayner, J. Young, F. Pognan, E. Hawkins, I. Currie and M. Davison, "Validation and Development of Fluorescence Two-Dimensional Differential Gel Electrophoresis Proteomics Technology," *Proteomics*, vol. 1, no. 3, 2001, pp. 377-396.

[95] B. Herbert, M. Molloy, A. Gooley, B. Walsh W. Bryson and K. Williams, "Improved Protein Solubility in Two-Dimensional Electrophoresis Using Tributyl Phosphine as Reducing Agent," *Electrophoresis,* vol. 19, no. 5, pp. 845–851.

[96] K.S Lilley, A. Razzaq and P. Dupree, "Two-Dimensional Gel Electrophoresis: Recent Advances in Sample Preparation, Detection and Quantitation," *Current Opinion in Chemical Biology*, vol. 6, no. 1, 2002, pp. 46-50.

[97] A. Gorg, O. Drews C. Luck, F. Weiland, and W. Weiss, "2-DE with *IPGs*," *Electrophoresis*, vol. 1, 2009, pp. 122–132.

[98] R. Duncan and J.W.B. Hershey, "Evaluation of Isoelectric Focusing Running Conditions During Two-Dimensional Isoelectric Focusing/Sodium Dodecyl Sulfate-

Polyacrylamide Gel Electrophoresis: Variation of Gel Patterns with Changing Conditions and Optimized Isoelectric Focusing Conditions," *Analytical Biochemistry*, vol. 138, no. 1, 1984, pp. 144-155.

[99] M. Kim and C. Kim, "Human Blood Plasma Preparation for Two-Dimensional Gel Electrophoresis," *J. Chromatogr. Analyt. Technol. Biomed. Life Sci.*, vol. 849, no. 1-2, 2007, pp. 203–210.

[100] J. Blonder, A. Terunuma, T.P. Conrads, K.C. Chan, C. Yee, D.A. Lucas, C.F. Schaefer, L.R. Yu, H.J. Issaq, T.D. Veenstra and J.C. Vogel, "A Proteomic Characterization of the Plasma Membrane of Human Epidermis by High-Throughput Mass Spectrometry," *J. Invest. Dermatol.,* vol. 123, 2004, pp. 691-699.

[101] R. Marouga, S. David and E. Hawkins, "The Development of the DIGE System:2D Fluorescence Difference Gel Analysis Technology," *Analytical and Bioanalytical Chemistry*, vol. 382, 2005, pp. 669-678.

[102] H.J Issaq and T.D. Veenstra, "Two-Dimensional Polyacrylamide Gel Electrophoresis (2D-PAGE): Advances and Perspectives," *Biotechniques,* vol. 44, 2008, pp. 697-700.

[103] J.P. Antoine, P. Carrette, R. Murenzi and B. Piette, "Image Analysis with Two-Dimensional Continuous Wavelet Transform," *Signal Processing*, vol. 31, 1993, pp. 241-272.

[104] http://www.hupo.org/

[105] J.J. Tyson and R.H. Haralick, "Computer Analysis of Two-Dimensional Gels by a General Image Processing System," *Electrophoresis*, vol. 7, 1986, pp. 107-113.

[106] P.F. Lemkin and L.E. Lipkin, "2-D Electrophoresis Gel Database Analysis - Aspects of Data Structures and Search Strategies in Gellab," *Electrophoresis*, vol. 4, no. 1, 1983, pp. 71-81.

[107] K.P. Pleissner, F. Hoffman, K. Kriegel, C. Wenk, S. Wegner, A. Sahlstrom, H. Oswald, H. Alt and E. Fleck, "New Algorithmic Approaches to Protein Spot Detection and Pattern Matching in Two-Dimensional Electrophoresis Databases," *Electrophoresis*, vol. 20, no. 4-5, 1999, pp. 755-765.

[108] P. Cutler, G. Heald, I.R. White and J. Ruan, "A Novel Approach to Spot Detection for Two-Dimensional Gel Electrophoresis Images Using Pixel Value Collection," *Proteomics*, vol. 3, no. 4, 2003, pp. 392-401.

[109] K. Takahashi, Y. Watanabe, M. Nakazawa and A. Konagaya, “Fully Automated Spot Recognition and Matching Algorithms for 2-D Gel Electrophoretogram of Genomic *DNA*,” *Genome Inf. Ser. Workshop*, vol. 9, 1998, pp. 161-172.

[110] L. Vincent and P. Soille, “Watersheds in Digital Spaces: an Efficient Algorithm Based on Immersion Simulations,” *IEEE Trans. Patt. Anal. Mach. Intel*., vol. 13, no. 6, 1991, pp. 583-598.

[111] Y. Kim, J. Kim, Y. Won and Y. In, “Segmentation of Protein Spots in 2-D Gel Electrophoresis Images with Watershed Using Hierarchical Threshold,” *Lect. Notes Comp. Sci.*, vol. 2869, 2003, pp. 389-396.

[112] R.D. Appel, J.R. Vargas, P.M. Palagi and D. Walther, "Melanie II – a Third-Generation Software Package for Analysis of Two-Dimensional Electrophoresis Images: II. Algorithms", *Electrophoresis*, vol.18, 1997, pp. 2735-2748.

[113] J.I. Garrels, "The QUEST System for Quantitative Analysis of Two-Dimensional Gels", *J. Biol. Chem.,* vol. 264, 1989 pp. 5269-5282.

[114] L. Tabar and P. Dean, *Teaching Atlas of Mammography*, 3rd Edition, New York: Thime, 2001.

[115] L. Garfinkel, M. Catherind, C. Boring, and C. Heath, “Changing Trends: An Overview of Breast Cancer Incidence and Mortality," *Cancer,* vol. 74, no. 1, 1994, pp. 222-227.

[116] R. Highnam and M. Brady, *Mammographic Image Analysis*, Dordrecht: Kluwer Academic Publishers, 1999.

[117] J. Suckling, J. Parker, D. Dance, S. Astley, I. Hutt, C. Boggis, I. Ricketts, E. Stamatakis, N. Cerneaz, S. Kok, P. Taylor, D. Betal and J. Savage, “The Mammographic Images Analysis Society Digital Mammogram Database,” *Exp. Med. Int. Cong. Ser.*, vol. 1069, 1994, pp. 375-8.

[118] A. Brander, P. Viikinkoski, J. Nickels, and L. Kivisaari, “Thyroid Gland: US Screening in a Random Adult Population,” *Radiology*, vol. 181, 1991, pp. 683-687.

[119] D. Koutras, “Subclinical Hyperthyroidism,” *Thyroid*, vol. 9, 1999, pp. 311-315.

[120] M.L. Rallison, B.M. Dobyns, A.W. Meikle, M. Bishop, J.L. Lyon, and W. Stevens, “Natural History of Thyroid Abnormalities: Prevalence, Incidence, and Regression of

Thyroid Diseases in Adolescents and Young Adults," *Am. J. Med*., vol. 92, no. 5, 1992, pp. 582.

[121] J.A. Jensen, "Field: A Program for Simulating Ultrasound Images," *Med. Biol. Eng. Comp.,* vol. 34, sup. 1, part 1, 1996, pp. 351-353.

[122] H. Miki et al, "Incidence of Ultrasonographically-Detected Thyroid Nodules in Healhty Adults," *Tokushima J. Exp. Med.*, vol. 40, 1993, pp. 43-46.

[123] M.H Irving and B. Catchpole, "ABC of Colorectal Diseases. Anatomy and Physiology of the Colon, Rectum and Anus," *Brit. Med. J.,* vol. 304, no. 6834, 1992, pp. 1106-1108.

[124] F.W. Ackroyd and S.E. Hedberg, "Colonic Polyps," *Ann. Rev. Med.*, vol. 36, 1985, pp. 619-625.

[125] G. Karamanolis, P. Psatha and K. Triantafyllou, "Endoscopic Treatments for Chronic Radiation Proctitis," *World J. Gastrointest. Endosc*., vol. 5, no. 7, 2013, pp. 308-312.

[126] D.J. Gawkrodger, *Dermatology: an Illustrated Colour Text*, Elsevier Health Sciences, 2002.

[127] G. Argenziano, S. Puig, I. Zalaudek, F. Sera, R. Corona, M. Alsina, and F. Barbato, "Dermoscopy Improves Accuracy of Primary Care Physicians to Triage Lesions Suggestive of Skin Cancer," *J. Clin. Onc.,* vol. 24, no. 12, 2006, pp. 1877-1882.

[128] R.H. Johr, "Dermoscopy: Alternative Melanocytic Algorithms – the ABCD rule of Dermatoscopy, Menzies Scoring Method and 7-Point Checklist," *Clin. Derm*., vol. 20, no. 3, 2002, pp. 240-247.

[129] The International Atlas of Dermoscopy and Dermatoscopy, http://www.dermoscopyatlas.com

[130] G. Argenziano and H.P. Soyer, "Dermoscopy of Pigmented Skin Lesions: a Valuable Tool for Earle Diagnosis of Melanoma," *Lanc. Oncology*, vol. 2, no. 7, 2001, pp. 443-449.

[131] F.H. Netter, *Atlas of Human Anatomy*, 3rd Edition, Rittenhouse Book Distributors, 2003.

[132] W.D Travis., L.B. Travis and S.S. Devesa "Lung Cancer," *Cancer*, vol. 75, 1995, pp. 191–202.

[133] S.J. Swensen, J.R. Jett, T.E. Hartman, D.E. Midthun, S.J. Mandrekar, S.L. Hillman, A.M. Sykes, G.L. Aughenbaugh, A.O. Bungum and K.L. Allen "*CT* Screening for Lung Cancer: Five Year Prospective Experience," *Radiology*, vol. 235, no. 1, 2005, pp. 259–265.

[134] S.G. Armato, G. McLennan, L. Bidaut, M.F. McNitt-Gray, C.R. Meyer, A.P. Reeves, B. Zhao, D.R. Aberle, C.I. Henschke, E.A. Hoffman, E.A. Kazerooni, H. MacMahon, E.J.R. van Beek, D. Yankelevitz et al. "The Lung Image Database Consortium (LIDC) and Image Database Resource Initiative (IDRI): A completed reference database of lung nodules on CT scans," *Medical Physics*, vol. 38, 2011, pp. 915-931.

[135] A. Palumbo, *The Anatomy and Physiology of the Healthy Periodontium*, Intech, 2011.

[136] R.R. Ranney, B.F. Debski and J.G. Tew, "Pathogenesis of Gingivitis and Periodontal Disease in Children and Young Adults," *Pediatr. Dent*., vol. 3, 1981, pp. 89-100.

[137] T. Eckhard, E.M. Valero and J.L. Nieves, "Labial Teeth and Gingiva Color Image Segmentation for Gingival Health-State Assessment," *Proc. Eur. Conf. Col. Graph. Im. Vis. (CGIV)*, 2012, pp. 102-7.

[138] T. McInerney and D. Terzopoulos, "Deformable Models in Medical Image Analysis: a Survey," *Medical Image Analysis*, vol. 1, 1996, pp. 91-108.

[139] F. Derraz, M. Beladgham and M. Khelif, "Application of Active Contour Models in Medical Image Segmentation," *Proc. IEEE Int. Conf. on Inform. Tech.: Cod. And Comp. (ITCC)*, 2004, pp. 675-681.

[140] P.A. Yushkevich, J. Piven, H.C. Hazlett, R.G. Smith, S. Ho, J.C. Gee and G. Gerig, "User-Guided 3D Active Contour Segmentation of Anatomical Structures: Significantly Improved Efficiency and Reliability," *NeuroImage*, vol. 31, 2006, pp. 1116-1128.

[141] S. Petroudi, C. Loizou, M. Patziaris, M. Pattichis and C. Pattichis, "A Fully Automated Method Using Active Contours for the Evaluation of the Intima-Media Thickness in Carotid US Images," *Proc. IEEE Int. Conf. Eng. Med. Biol. Soc. (EMBS)*, 2010, pp. 8053-7.

[142] J. Xu, J.P. Monaco and A. Madabhushi, “Markov Random Field Driven Region-Based Active Contour Model (MaRACel): Application to Medical Image Segmentation,” *Proc. Int. Conf. Med. Im. Comp. Comp.-Ass. Inter. (MICCAI)*, 2010, pp. 197-204.

[143] Y. Shang, X. Yang, L. Zhu, R. Deklerck and E. Nyssen, “Region Competition Based Active Contour for Medical Object Extraction,” *Comp. Med. Im. Graph.*, vol. 32, no. 2, 2008, pp. 109-17.

[144] L. Wang, C. Li, Q. Sun, D. Xia and C. Kao, “Active Contours Driven by Local and Global Intensity Fitting Energy with Application to Brain MR Image Segmentation,” *Comp. Med. Imag. Graph.*, vol. 33, 2009, pp. 520-31.

[145] D. Huttenlocher, G. Klanderman and W. Rucklidge, “Comparing Images Using the Hausdorff Distance,” *IEEE Trans. Patt. Anal. Mach. Intell*., vol. 15, 1993, pp. 850-63.

[146] P. Soille. *Morphological Image Analysis-Principles and Applications*. Springer, Berlin, 1999.

[147] F.Y. Shih and Y.T. Wu, “Decomposition of Arbitrary Gray-Scale Morphological Structuring Elements,” *Pattern Recognition*, vol. 38. pp. 2323-2332, 2005.

[148] P. Dokládal, I. Bloch, M. Couprie, D. Ruijters, R. Urtasun and L. Garnero, “Topologically Controlled Segmentation of 3D Magnetic Resonance Images of the Head by Using Morphological Operators,” *Pattern Recognition*, vol. 36, 2003, pp. 2463-2478.

[149] B. Bödvarsson, S. Klim, M. Mørkebjerg, S. Mortensen, C. H. Yoon, J. Chen, J. R. Maclaren, P. K. Luther, J. M. Squire, P. J. Bones and R. P. Millane, “A Morphological Image Processing Method for Locating Myosin Filaments in Muscle Electron Micrographs,” *Im. Vis. Comp*., vol. 26, 2008, pp. 1073-1080.

[150] T. Li, S. Wang and N. Zhao, “Gray-Scale Edge Detection for Gastric Tumor Pathologic Cell Images by Morphological Analysis,” *Comp. Biol. Med.*, vol. 39, 2009, pp. 947-952.

[151] D. Welfer, J. Scharcanski, C. M. Kitamura, M. M. Dal Pizzol, L. W. B. Ludwig, D. and R. Marinho, “Segmentation of the Optic Disk in Color Eye Fundus Images Using an Adaptive Morphological Approach,” *Comp. Biol. Med*., vol. 40, 2010, pp. 124-137.

[152] M.M. Skolnick, “Application of Morphological Transformations to the Analysis of Two-Dimensional Electrophoresis Gels of Biological Materials,” *Comp. Vis. Graph Im. Proc.*, vol. 35, 1986, pp. 306-322.

[153] P. Peer and L.G. Corzo, “Local Pixel Value Collection Algorithm for Spot Segmentation in Two-Dimensional Gel Electrophoresis Research,” *Comp. Func. Genom.*, vol. 2007, 2007, Article ID 89596.

[154] F.G. Huang and G. Yang, “The Application of Soft Morphology in Image Edge Detection,” *J. Image Graph. China*, vol. 5, 2000, pp. 284-288.

[155] E.R. Urbach and M.H.F. Wilkinson, “Efficient 2-D Grayscale Morphological Transformations with Arbitrary Flat Structuring Elements,” *IEEE Trans. Im. Proc*., vol. 17, 2008, pp. 1-8.

[156] D.T. Lin, “Autonomous Sub-Image Matching for Two–Dimensional Electrophoresis Gels using MaxRST Algorithm,” *Im. Vis. Comp*., In Press, Corrected Proof, 2010.

[157] C. Guda, E. Fahy and S. Subramaniam, “MITOPRED: a Genome-Scale Method for Prediction of Nucleus-Encoded Mitochondrial Proteins,” *Bioinformatics*, vol. 20, 2004, pp. 1785-1794.

[158] S. Theodoridis and K. Koutroumbas, *Pattern Recognition*, 4th Edition, Academic Press, 2008.

[159] S.M. Pizer, E.P Amburn and J.D. Austin, “Adaptive Histogram Equalization and its Variations,” *Comp. Vis. Graph. Im. Proc*., vol. 39, 1987, pp. 355-368.

[160] A.P. Stefanoyannis, L. Costaridou, S. Skiadopoulos and G. Panayotakis, “A Digital Equalization Technique Improving Visualization of Dense Mammary Gland and Breast Periphery in Mammography,” *Eur. J. Radiol*., vol. 45, 2003, pp. 139-149.

[161] L.M. Fayad, Y. Jin, A.F. Laine, Y.M. Berkmen, G.D. Pearson, B. Freedman and R.V. Heertum, “Chest CT Window Settings with Multiscale Adaptive Histogram Equalization: Pilot Study,” *Radiology*, vol. 223, 2002, pp. 845-852.

[162] E.D. Pisano, S. Zong, B.M. Hemminger, M. DeLuca, R.E. Johnston, K. Muller, M.P. Braeuning and S.M. Pizer, “Contrast Limited Adaptive Histogram Equalization Image Processing to Improve the Detection of Simulated Speculations in Dense Mammograms,” *J. Digit. Im*., vol. 11, 1998, pp. 193-200.

[163] S.H. Lee and J.K. Seo, “Level Set-Based Bimodal Segmentation with Stationary Global Minimum,” *IEEE Trans. Im. Proc.*, vol. 15, no. 9, 2006, pp. 2843-2852.

[164] M. Krueger, P. Delmas and G. Gimel’Farb, “Active Contour Based Segmentation of 3D Surfaces,” *Eur. Conf. Comp. Vis*., Springer-Verlag, 2008, pp. 350–363.

[165] H. Jin, A. Yezzi, and S. Soatto, “Mumford-Shah on the Move: Region-based Segmentation on Deforming Manifolds with Application to 3D Reconstruction of Shape and Appearance from Multi-View Images,” *J. Math. Imag. Vis*., vol. 29, 2007, pp. 219–234.

[166] K.I. Chang, K.W. Bowyer and P.J. Flynn, “An Evaluation of Multimodal 2D+3D Face Biometrics,” *IEEE Trans. Patt. Anal. Mach. Intell*., vol. 27, 2005, pp. 619–624.

[167] T. Shen, H. Li and X. Huang, “Active Volume Models for Medical Image Segmentation,” *IEEE Trans. Med. Imag.*, vol. 30, 2011, pp. 774-91.

[168] K. K. Delibasis, A. Kechriniotis and I. Maglogiannis, “A Novel Tool for Segmenting 3D Medical Images Based on Generalized Cylinders and Active Surfaces,” *Comp. Meth. Prog. Biomed.*, vol. 111, 2013, pp. 148-165.

[169] X. Cai and A. Sowmya, “Level Learning Set: A Novel Classifier Based on Active Contour Models,” *LNCS*, vol. 4701, 2007, pp. 79-90.